5-2018

Assessment of the Structural and Thermal Behavior of Concrete Masonry Construction via Experimentally Informed Numerical Models

Marcos Javier Martínez Andino
Clemson University, marcosm@clemson.edu

ASSESSMENT OF THE STRUCTURAL AND THERMAL BEHAVIOR OF CONCRETE MASONRY CONSTRUCTION VIA EXPERIMENTALLY INFORMED NUMERICAL MODELS

A Dissertation
Presented to
the Graduate School of
Clemson University

In Partial Fulfillment
of the Requirements for the Degree
Doctor of Philosophy
Civil Engineering

---

by
Marcos Javier Martínez Andino
May 2018

Accepted by:
Dr. Sez Atamturktur, Committee Chair
Dr. Brandon Ross
Dr. John Sanders
Dr. Qiushi Chen

ABSTRACT

This dissertation aims at describing and examining the compressive and out-of-plane behavior and failure patterns of mortarless masonry prisms and walls through experimental tests and numerical models. In addition, the thermal performance of various masonry units is investigated through detailed thermo-fluid dynamic models to contribute to the masonry construction knowledge base.

Studies on the behavior of masonry systems are fundamental to understanding their structural and thermal performance. One of the variations of this type of construction is dry-stack masonry, i.e., units laid without mortar between the joints. Despite reducing the time and cost of construction, mortarless construction has not gained widespread acceptance as a viable alternative to mortared masonry because the mechanical behavior of the mortarless system is not yet fully understood. To address this knowledge gap, this research developed numerical models to compare their response under compressive and out-of-plane loads with experimental tests.

The validated structural numerical models of mortarless masonry prisms and reinforced mortarless walls are then used to predict and thoroughly examine the effects of design parameters. The mortarless prisms in these models included variations in the surface roughness between the units. These models revealed that both the stress distribution and failure pattern depended on the unit strength, the condition of the surface in contact between the units, and the grout strength for grouted prisms. The mortarless walls studied here included grout and steel reinforcement within the cells. In these walls, the load-carrying capacity, the displacement ductility, and the failure patterns were examined based

on variations in the unit and grout compressive strength, yield strength, and reinforcement and grouting ratios.

The thermal response of masonry units also merits further study to better understand the behavior of standard units as well as thermally efficient unit configurations. In this research, validated numerical models were used to evaluate the heat flow path, the distribution of temperatures, and the air velocities within the units. The results revealed the importance of including the three heat transfer mechanisms and the air flow within the cells of masonry units to better approximate the experimental thermal performance.

DEDICATION

I would like to dedicate this dissertation to my parents, María Andino and Marcos Martínez, for their endless love and support.

ACKNOWLEDGMENTS

First and foremost, I want to thank God Almighty for giving me the strength, courage, perseverance, and hope to complete this dissertation when I had doubts. Without His blessing, this achievement would not have been possible.

I would like to thank and acknowledge my advisor, Dr. Sez Atamturktur, who taught me what a relentless work ethic means. Dr. Atam gave me the opportunity to turn my dream into reality and for that I will be eternally grateful. Her wisdom, unconditional support and guidance saw me through until the end. I have great gratitude for all my committee members: Dr. Brandon Ross, Dr. John Sanders, and Dr. Qiushi Chen. Their guidance and expertise were insightful in times of struggle to successfully achieve high-quality research.

I am thankful to the National Concrete Masonry Association Education and Research Foundation, especially to Jason Thompson for the funding and support to make this research possible. Also, I would like to thank Seth Adams, Ahmad Tarawneh, Nate Huygen, and Jonathan Broyles, whose support, encouragement and incredible ideas helped tremendously with the completion of this dissertation. To Dr. Austin Gorman and Barbara Ramirez for their editorial assistance at the end stage of this dissertation. Dr. Saurabh Prabhu, Dr. Xiaoyu Hu, and Robert Locke also deserve recognition for their feedback and selfless willingness to help. I would like to thank Kristi Baker and Dr. Abdul Khan for all the assistance and advice provided during these years. Finally, I also would like to extend my eternal gratitude to Adrienne Fama, who provided invaluable editorial help and supported me at all times to achieve my goal, propelling me with motivation and love.

TABLE OF CONTENTS

TABLE OF CONTENTS (CONTINUED)

Chapter Page

TABLE OF CONTENTS (CONTINUED)

Chapter Page

TABLE OF CONTENTS (CONTINUED)

Chapter Page

LIST OF FIGURES

Figure Page

LIST OF FIGURES (CONTINUED)

Figure Page

LIST OF FIGURES (CONTINUED)

Figure Page

LIST OF FIGURES (CONTINUED)

Figure Page

LIST OF FIGURES (CONTINUED)

Figure Page

LIST OF FIGURES (CONTINUED)

Figure Page

LIST OF FIGURES (CONTINUED)

Figure Page

LIST OF FIGURES (CONTINUED)

Figure Page

LIST OF TABLES

Table Page

LIST OF TABLES (CONTINUED)

Table Page

CHAPTER ONE

INTRODUCTION

1.1 Motivation for this Research

Over the past 70 years, a renewed research interest in the behavior of masonry systems has led to improvements in their structural and thermal performance (Edwards et al. 2010; De Berardinis 2014). With the incorporation of steel reinforcements and new insulation materials in masonry walls specified in the earliest building codes in the 1950s, the strength and energy efficiency of masonry systems have increased significantly (BIA 1996). These advances, coupled with the increased accessibility of quality-controlled masonry units, have enabled the construction of stronger, more efficient structures that have reduced wall thickness and weight while at the same time increasing performance (Klingner 1994; Hendry 2001; Hendry et al. 2003; Heath et al. 2012).

Despite these advancements in structural and thermal efficiency, masonry construction is a slow, labor-intensive process that is limited by both the number of units a masonry crew can lay and the time that mortar needs to cure (Hines 1992). Researchers have investigated many strategies for reducing the construction time of masonry systems (Hines 1993; Garrity 1994; Pave and Uzoegbo 2010). One such strategy involves omitting bedding mortar, thus creating building structures without mortar to bind the units (Hines 1992; Ramamurthy et al. 2004; Ramamurthy and Nambiar 2004). These mortarless systems can be classified based on the interface between units as non-interlocking or interlocking, both of which can also incorporate surface bonding agents and pre-stressed reinforcement

elements to enhance their capacities (Ramamurthy and Nambiar 2004). Masonry structures with non-interlocking units rely on the friction between units to provide compressive and shear capacity, while the structure develops limited flexural capacity. For structures with interlocking units, the protrusions and grooves of individual units hold the system together as a monolithic structure, providing compressive, shear, and flexural strength (Anand et al. 2000). Both systems can enhance their structural and thermal performance by internally adding grouting, steel reinforcing bars, and insulated materials.

Mortarless masonry systems have many advantages over mortared systems, including faster construction. As no mortar is involved between units, masonry structural elements can be built in a short amount of time and loaded immediately after constructions; no curing of mortar joints is needed (Hines 1993). This system also has a decreased need for skilled labor as there is no need to lay mortar in the joints. Because skilled labor is not required and the construction process is faster, the construction of mortarless systems can become highly cost-effective (Pave 2008; Zahra 2017). Despite these advantages, mortarless construction is not supported by current masonry design codes and, as a result, has not been as widely implemented (Biggs and Forsberg 2008; Pave and Uzoegbo 2010). The under-utilization of mortarless systems is partly due to the limited knowledge about stress and deformation behavior and the lack of calculation methods for design (Marzahn 1999; Biggs 2002). Although it has been demonstrated that mortared and mortarless construction have similar in-plane and out-of-plane capacities (Ferozkhan 2005), the failure modes of these two construction types are fundamentally different, with the failure modes of the latter being less understood.

The thermal characteristics of a structure play a critical role in energy efficiency. In concrete masonry construction, walls built with concrete masonry units (CMUs) serve as the major surface areas through which heating and cooling are lost (Eumorfopoulou and Kontoleon 2009; Pacheco-Torgal et al. 2015). In thermal analysis of masonry structures, it is critical to investigate the effect of the three heat transfer mechanisms (i.e., conduction, convection, and radiation) and air flow within the unit cells (Al-Homoud 2005; Kosny and Christian 1995; Wati et al. 2017). Studies on these effects in such systems are limited, providing opportunities to improve the design of the masonry unit. The thermal performance of the masonry, which is measured in terms of its thermal resistance or R-value, depends on the physical properties of their units (i.e., dimensions, density) and their thermal properties (i.e., thermal conductivity) (Ozel 2011; Abdullah et al. 2015).

Globally, an increased fundamental understanding of structural behavior in mortarless systems and the thermal behavior of masonry concrete units is required to improve their performance. To meet this need, this dissertation has the potential to lead to construction and environmental benefits including expanded knowledge of mortarless masonry, increased building affordability, minimization of waste, reduction in cost and time of construction, improved health and safety of laborers, and reduction in overall energy consumption.

1.2 Contributions of the dissertation

After reviewing the past contributions and findings and discussing the potential future directions of mortarless masonry construction, the research reported here developed a modeling strategy to improve the understanding of the compressive behavior of

mortarless concrete masonry prisms by taking into account the surface roughness at the prisms' bed joints. At the same time, out-of-plane behavior of reinforced mortarless masonry walls was thoroughly investigated. In the study of prisms and walls, the mechanisms of failure have been examined through both laboratory experiments and high-fidelity finite element models that have the ability to yield accurate predictions under different changes in design variables. This dissertation also evaluated the thermal behavior of concrete masonry units, including the three heat transfer mechanisms (i.e., conduction, convection, and radiation) and the effect of air flow within the cells of the units. Realistic R-values were predicted through sophisticated numerical models for different unit geometries and insulation types to establish which types allow for the most effective compromise between energy efficiency and cost. In this dissertation, the experimental programs provide insight into the behavior of the masonry, while the numerical models provide a powerful means of approximating the underlying physics of the masonry's structural and thermal behavior.

1.3 Dissertation Organization

The remainder of this dissertation is organized into five chapters. Chapter Two offers a review of the literature published on mortarless masonry construction. This review provides descriptions of the methodologies employed, testing frameworks, and numerical models developed by other scholars. This chapter is divided into sections corresponding to the use of non-interlocking and interlocking masonry units, the application of surface bonding on masonry walls, the pre-stressing of reinforced masonry elements, and the use of alternative masonry materials. By identifying gaps in the literature, Chapter Two also

indicates directions for future research for improving the understanding of the behavior of mortarless masonry systems. This chapter is currently in preparation for submission to a peer-reviewed journal.

Chapter Three explains the research conducted as part of this dissertation. It begins by analyzing the development of experimentally informed numerical models used to assess the behavior of mortarless masonry prisms under axial compressive loads. These predictive models take into account the bed surface roughness of two types of mortarless masonry prisms, units with a ground surface and units with an unground surface. Based on these predictive models, a parametric analysis is next conducted to find relationships between unit design variables (e.g., material properties, surface roughness, unit size, and grout strength) and to evaluate the performance of mortarless prisms. Chapter Three is a peer-reviewed journal manuscript that will be published in a forthcoming issue of the American Society of Civil Engineers' *Journal of Structural Engineering*.

Chapter Four assesses the behavior of reinforced dry-stack concrete masonry walls subjected to out-of-plane bending. Validated numerical models are developed to predict and investigate the influence of various design parameters (e.g., unit and grout compressive strength, yield strength of reinforcing bars, and reinforcement and grouting ratio) on the flexural behavior of mortarless masonry walls. This chapter is currently under review for publication in Elsevier's *Building Materials Journal*.

Chapter Five focuses on the thermal performance of concrete masonry units. To investigate thermal and fluid interactions of the units, an experimental program is conducted, and three-dimensional numerical models are developed to enhance predictive

capabilities. These numerical models enhance knowledge related to the thermal performance of CMUs with different configuration types as they consider both the three heat transfer mechanisms and air flow within the units. At the end of the chapter, the results obtained from the experimental program and numerical models are combined with a cost-effectiveness analysis to provide insights into the feasibility of implementing different configuration types in the construction industry. Chapter Five has been accepted for publication in Elsevier's *Building Materials Journal.*

The final chapter of this dissertation summarizes key points of the research, discusses its impact, and considers its assumptions and limitations. Chapter Six also includes a discussion of future work that may stem from the research presented here.

References

Abdullah, C.S., Bahaudin, A.Y., Nawi, M.N., Baluch, N.H., Kamarudden, A.M., Mohtar, S., Mohamed Udin, Z., Zulhumadi, F., and Abu Bakar, Z. (2015). "Implications of Technology Transfer in the Design and Constructiton of Load-Bearing Masonry Buildings," *Jurnal Teknologi*, 77(5), 127-134.

Al-Homoud, M. S. (2005). "Performance Characteristics and Practical Applications of Common Building Thermal Insulation Materials," *Building and Environment*, 40(3), 353-366.

Anand, K., and Ramamurthy, K. (2000). "Development and Performance Evaluation of Interlocking-Block Masonry," *Journal of Architectural Engineering*, 6(2), 45-51.

BIA. (1996). "Reinforced Brick Masonry – Introduction," *The Brick Industry Association*, Technical Notes 17, 1-7.

Biggs, D. T. (2002). “Development of a Mortarless Post-Tensioned Masonry Wall System,” *In Proceedings of the 6th international masonry conference,* 28-32.

Biggs D.T., and Forsberg, T.E. (2008). “A Mortarless Prestressed Masonry House: Case Study.” *Proceedings of the 14th International Brick and Block Masonry Conference,* Sydney, Australia, 1-11.

Edwards, J., Gayed, M., Pyra, M., and Rodriguez, T. (2010). “Design and Construction of Interlocking Mortarless Block Masonry,” *In Proceedings of the 2nd Masonry Mini Symposium*, Edmonton, Alberta, 4-43.

Eumorfopoulou, E. A., and Kontoleon, K. J. (2009). “Experimental Approach to the Contribution of Plant-Covered Walls to the Thermal Behavior of Building Envelopes.” *Building and Environment*, 44(5), 1024-1038.

Ferozkhan, M. (2005). "Development of a Dry Stack Masonry System for Effective Resistence to Out-of-Plane Bending," *M.S. thesis*, Central Queensland University, Brisbane, Australia.

Garrity, S. (1994). The Shellstone System – A New Form of Dry-Stacked Masonry Construction,” *Proc. of the 10th International Brick and Block Masonry Conference,* Masonry Council of Canada, Calgary, Alberta, Canada.

Hendry, A. W., Sinha, B. P., and Davies, S. R. (2003). *Design of Masonry Structures*. CRC Press.

Hines, T. (1992). “Using Dry-Stacked Concrete Masonry for Affordable Construction,” *In 4th International Seminar on Structural Masonry for Third World Countries*, Madras, India.

Hines, T. (1993). "Benefits of Drys-Stack Interlocking Concrete Masonry as a Component of Cost Effective Construction," *The Sixth North American Masonry Conference*, Philadelphia, Pennsylvania.

Kosny, J., and Christian, J. E. (1995). "Thermal Evaluation of Several Configurations of Insulation and Structural Materials for Some Metal Stud Walls," *Energy and Buildings*, 22(2), 157-163.

Marzahn, G. (1999). "Investigation on the Initial Settlement of Dry-Stacked Masonry under Compression," *LACER*, *4*, 253-270.

National Concrete Masonry Association. (2013). "R-Values and U-Factors of Single Wythe Concrete Masonry Walls." *NCMA TEK 6-2C*.

Ozel, M. (2011). "Thermal Performance and Optimum Insulation Thickness of Building Walls with Different Structure Materials," *Applied Thermal Engineering*, 31(17-18), 3854-3863.

Pacheco-Torgal, F., Lourenco, P.B., Labrincha, J.A., Kumar, S., and Chindaprasirt, P. (2015). *Eco-efficient Masonry Bricks and Blocks: Design, Properties and Durability*, Woodhead Publishing Series in Civil and Structural Engineering.

Pave, R. F. (2008). *Strength Evaluation of Dry-Stack Masonry*, Ph.D. Dissertation, University of the Witwatersrand, South Africa.

Pave, R. F., and Uzoegbo, H. (2010). "Structural Behavior of Dry-Stack Masonry Construction," *Proc. SB10 Portugal: Sustainable Building Affordable to All: Low Cost Sustainable Solutions*, Algarve, Portugal.

Ramamurthy, K., and Nambiar, E.K. (2004). "Accelerated Masonry Construction: Review and Future Prospects," *Progress in Structural Engineering and Materials*, 6(1), 1-9.

Sadineni, S. B., Madala, S., and Boehm, R. F. (2011). "Passive Building Energy Savings: A Review of Building Envelope Components." *Renewable and Sustainable Energy Reviews*, 15(8), 3617-3631.

Wati, E., Meukam, P., and Damfeu, J. C. (2017). "Modeling Thermal Performance of Exterior Walls Retrofitted from Insulation and Modified Laterite Based Bricks Materials," *Heat and Mass Transfer*, 53(12), 3487-3499.

CHAPTER TWO

LITERATURE REVIEW

2.1 Introduction

Masonry systems, in their earliest forms in Egyptian pyramids and the monuments of Stonehenge, involved walls constructed by dry-stacking stone units without a bonding agent (Hussein and El-Shishiny 2009; Sasaki et al. 2011; Cuadra 2012). This construction technique relied on friction and interlocking action between the units to achieve structural stability. To achieve increased structural performance and reduced cost, more modern civilizations began to build walls by utilizing a workable paste made of mud, clay with sand, gypsum, or lime to bind masonry units composed of stone, sun-dried clay brick, calcium silicate, or concrete block. This composite arrangement allowed to reduce the wall thickness in the masonry. In the 1800s, the development of Portland cement and the fabrication of steel brought new technologies to the building industry (Venkatarama 2009). In the 1950s, the masonry construction industry was revitalized with the emergence of the concrete masonry unit (CMU) (BIA 1996). Subsequently, masonry construction with mortar was codified in design specifications, leading to the widespread use of mortared masonry construction in the U.S. (Tobriner 1984). It was not until the 1990s that the use of dry-stack masonry began to reemerge. Compared to mortared masonry, mortarless construction has been reported to be faster, more cost-effective, less labor intensive, and less dependent on skilled labor (Oh 1994; Beall 2000; Murray 2007). The introduction of new masonry unit designs further supported the revival of mortarless construction through the use of both non-interlocking and interlocking units (Hines 1993).

Like any other structural system, dry-stacked masonry assemblies are subjected to various types of external loads. In systems with non-interlocking units (Fig. 2-1-a), lateral loads are resisted through friction between the units. Using friction alone tends to be insufficient for walls with depths common in practical, modern-day applications (Langer 1992; Schubert 1995; Velez et al. 2014; Martínez et al. 2017). In systems using interlocking units (Fig. 2-1-b), lateral loads can be resisted by protrusions and grooves. These can also help with self-alignment and leveling in the masonry structure (Glitza 1991; Anand and Ramamurthy 2005; Ali et al. 2012; Dyskin et al. 2012; Liu et al. 2016; Palios et al. 2017). To ensure sufficient structural integrity, these dry-stack masonry systems can include widely-known enhancements such as grouting and steel reinforcement. They can also use less widely-studied approaches such as surface bonding and pre-stressing to increase the load-bearing capacity of the masonry assembly (Anand and Ramamurthy 2000). These mortarless structures with non-interlocking or interlocking units can also vary depending on the surface bonding material and whether they use pre-stressed reinforcement elements, as it affects the capacity of the structure.

Surface bonding material, such as fiberglass or reinforced cement-polymer mix, are sometimes used in dry-stack masonry systems to cover the faces of the masonry wall as shown in Fig. 2-1-c (Lohr 1992; Ferozkhan 2005). The tensile strength of the surface bonding material provides enhancements to both the shear capacity of the wall under in-plane loading and its flexural capacity under out-of-plane loading (Arifuzzaman and Saatcioglu 2012). Dry-stacked masonry systems can also be pre-stressed (Fig. 2-1-d), leading to a compressive state in the masonry units prior to the application of external

loads. This compressive state is achieved through the use of steel bars that are anchored at two ends of the masonry element. When the bars are tensioned (i.e., pre-tensioned or post-tensioned), the tensile forces in the bars are transferred into compression in masonry by external bearing plates and anchorage devices. Pre-stressing improves both the flexural capacity, by counteracting the tensile stresses that result from bending (Lohr 1992; Graham and Page 1995), and the shear capacity, through the increased friction between the units and dowel action of the vertical tensioned steel bars (Al-Manaseer and Neis 1987; Dawe and Aridru 1992).

The construction options shown in Fig. 2-1 can be implemented alone or in combination and can be used with an essentially infinite variety of interlocking unit designs. This variety leads to a remarkably large number of possible design configurations, making it challenging to evaluate them all and develop generally applicable design codes, a situation that has been identified to prevent its standardized widespread use of mortarless construction technique (Hines 1993; Biggs 2002; Pave and Uzoegbo 2010).

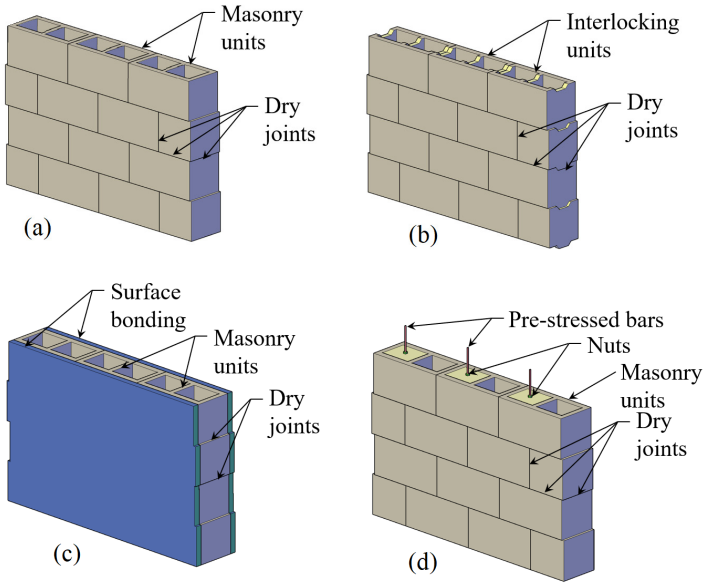

Fig. 2-1. Dry-stacked masonry systems: (a) non-interlocking units, (b) interlocking units, (c) surface bonding on faces, and (d) pre-stressed elements.

What is more, the dry-stacked masonry systems shown in Fig. 2-1 under compressive and lateral loads are affected by the type of unit (i.e., non-interlocking, interlocking), the contact surface roughness between units, the slenderness of the wall, the duration of the applied load, and the variability of unit dimensions (Oh 1994; Marzahn and Konig 2002; Anand and Ramamurthy 2005; Ferozkhan 2005; Jaafar et al. 2006b; Thanoon et al. 2007; Andreev et al. 2012; Atamturktur et al. 2016; Martínez et al. 2017). However, the effect of these parameters on the behavior of mortarless masonry structures is not yet fully understood further complicating the development of design codes.

This paper aims to present a comprehensive review of past contributions to allow for the identification and discussion of research gaps, thus revealing the need for future studies to better understand the behavior of dry-stacked masonry systems through

numerical and experimental investigations. This paper is organized as follows: Section 2 presents modeling techniques to take the surface roughness of the units at the bed joints into account in numerical models. Section 3 reviews studies on mortarless prisms and wall structures with non-interlocking units, discussing relevant experimental and numerical investigations. Section 4 also reviews studies on mortarless prisms and wall structures while examining interlocking units. Section 5 presents studies on various dry-stack masonry construction types, including those that use pre-stressed elements and surface bonded agents. Section 6 offers marks and identifies the need for future studies to support the development of mortarless masonry design codes. Section 7 contains the conclusions to the research conducted throughout the paper.

2.2 Approaches for Modeling and Simulation of Mortarless Masonry Systems

Unlike mortared masonry system, the surface roughness at the bed joint in mortarless masonry systems plays a critical role. The contact behavior of a dry masonry joint is a complex phenomenon due to the high stress concentrations in the asperities, which cause local crushing at the bed surface. For example, as the vertical load applied on the dry-stacked units increases, the asperities are crushed and the gaps between the units gradually close, leading to the softening behavior or what is referred to as the “seating effect.” Computational modeling can be used to describe further this contact behavior between the units on mortarless structures under different load scenarios.

Finite element modeling has been widely used at various levels of sophistication to simulate the complex contact behavior in mortarless construction (Pei et al. 2005; Zhang et al. 2014). One modeling approach, to account for surface roughness at the bed joint, has

involved modeling the asperities by considering their approximate geometric properties in a three-dimensional solid model (see Fig. 2-2). In Martinez at el. (2017), this approach was used to compare the compressive response of prisms using a ground (smooth) surface to prisms using an unground (rough) surface at the bed joint. In this study, contact elements were used at the bed joint to control for the sliding behavior in both surface treatments.

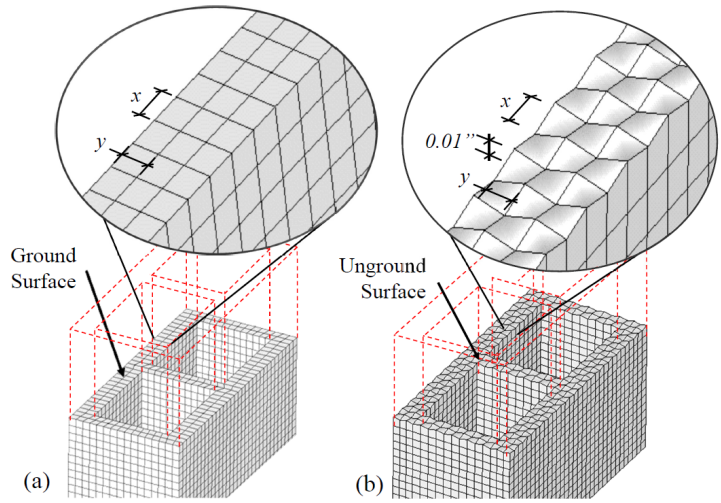

Fig. 2-2. Representative FE models for prisms with (a) ground and (b) unground units [Source: Martínez et al. 2017, with permission].

Additionally, three-dimensional numerical simulations have also been used to model the effect of contact between the units on mortarless structures. To model this contact, another technique relies on the use of nonlinear spring elements that link nodes of the units' bed surface mesh under vertical loads (as shown in Fig. 2-3). These spring elements are unidirectional elements in which a generalized force-displacement curve is needed to describe the nonlinear contact stiffness of the joint. Using such nonlinear link elements with eight-node solid elements to represent the masonry units, Oh (1994) described the response of mortarless prisms in terms of stresses and displacements under

vertical loads. The response of this modeling technique has been evaluated, resulting within the 20% of the experimental data.

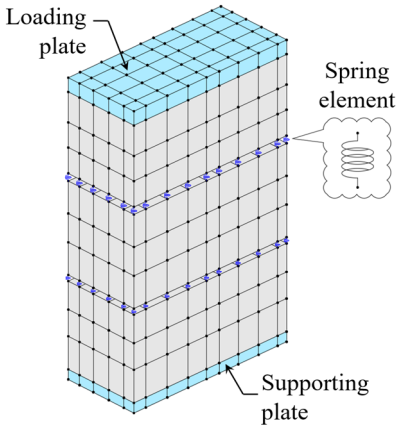

Fig. 2-3. Numerical model for three-unit mortarless prism using spring elements at the dry joint.

Simplified models using three-node interface elements to simulate the dry joint have been employed to study the effect of the surface roughness on the mechanical behavior of masonry structures. One of these models uses two-dimensional eight-node isoparametric plane elements for the masonry units combined with interface elements for the dry joint. For example, Al-Wathaf (2006) developed a model to assess the effect of the surface roughness on the response of dry-stack structures subjected to vertical (see Fig. 2-4-a), in-plane (see Fig. 2-4-b), and out-of-plane loads (see Fig. 2-4-c). These models require a normal tangent and a shear stiffness of the joint to describe the nonlinear behavior of the closing deformation at the bed joint under vertical loads. Al-Wathaf modeled the joint he used in his research using a three-node interface element, but in furthering this research study using the joint with plate elements and six nodes, Hejazi was able to describe the mortarless behavior.

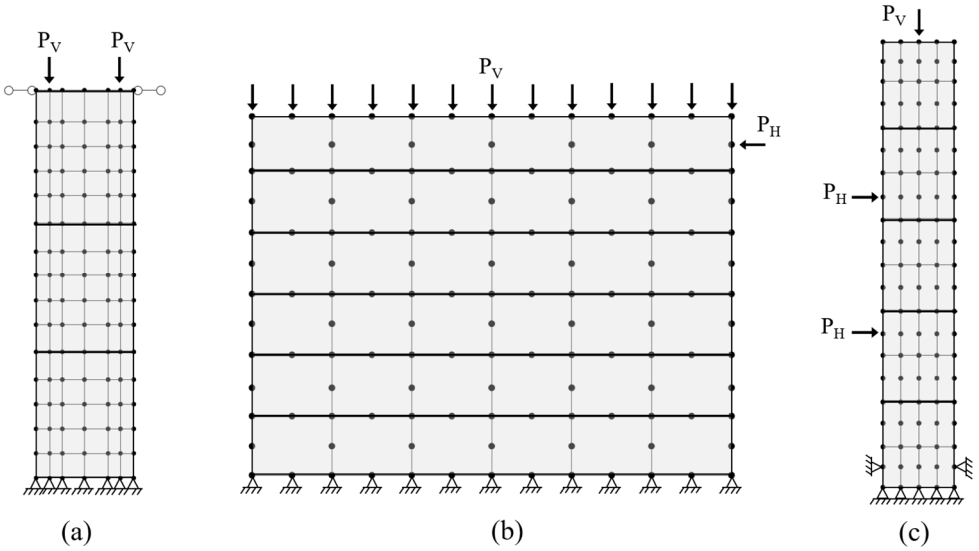

Fig. 2-4. Numerical models of mortarless masonry (a) three-unit prism under vertical load; (b) wall under vertical and lateral in-plane load; and (c) wall under vertical and lateral out-of-plane loads using zero-thickness elements at the dry joint.

Instead of Al-Wathaf's three-node interface elements, the research conducted by Hejazi et al. (2016) used six-node isoparametric interface plane elements which were used to model the horizontal and vertical dry joints between the units as seen in Fig. 2-5. Hejazi et al. developed a two-dimensional wall model to simulate the behavior of dry-stack masonry walls under lateral in-plane seismic activity using eight-node isoparametric plane elements to model the masonry units. The behavior of the bed joints is described by properties in the interface elements such as the normal and tangent stiffness to account for the compressive and shear behavior. This technique has not widely been implemented, and thus requires rigorous validation with experimental data.

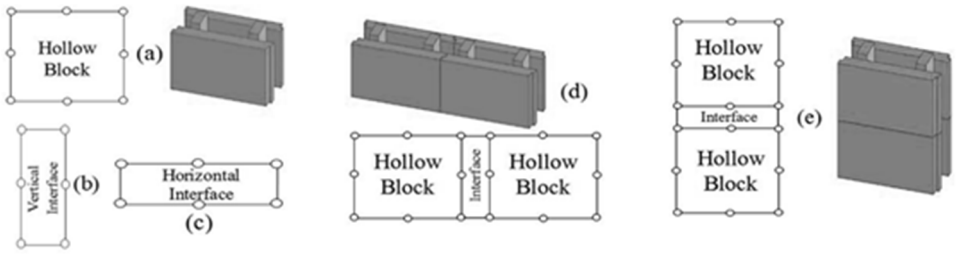

Fig. 2-5. (a) Eight-node elements used for modeling of hollow units, (b) six-node elements used for modeling the vertical interface, (c) six-node elements used for modeling the horizontal interface, (d) connection of two horizontal hollow units with vertical interface, and (e) connection of two vertical hollow units with horizontal interface [Source: Hejazi et al. 2015, with permission].

Some of the aforementioned modeling techniques showed acceptable correlation to experimental data. Three-dimensional models are powerful to account with different unit geometries and design configurations in which the surface roughness is the key in these mortarless systems. These models allow for a precise prediction of the evolution of the stress distribution and failure modes along the masonry structure. On the other hand, simplified techniques can assess the effect of the surface roughness with limitations and assumptions in the behavior of mortarless masonry. In any case, experimental tests are necessary for the purpose of validating the simulations through rigorous test-analysis comparisons. Research on mortarless prisms and walls has been conducted using non-interlocking and interlocking units combined with alternatives to enhance the behavior through experimental tests, numerical models, or a combination of these.

2.3 Knowledge-Base on Mortarless Masonry Systems with Non-Interlocking Units

2.3.1 Mortarless Prisms with Non-Interlocking Units

Research on mortarless prisms using non-interlocking units has been primarily experimental, exploring the prisms' short-term (i.e., near instantaneous) response under vertical loads. A key aspect of these experiments was the evaluation of the effect of surface roughness at the bed joint between the units on the compressive strength and the modulus of elasticity of mortarless prisms (Marzahn and Konig 2002; Andreev et al. 2012; Zahra 2016). The experiments conducted by Lin et al. (2015), for instance, have shown a 15% decrease in the mortarless prisms' compressive strength and a 62% decrease in the mortarless prisms' modulus of elasticity compared to their mortared counterparts. Similar results were obtained by Atamturktur et al. (2016). This can be seen in Fig. 2-6 where the representative stress-strain plots of prisms using ground (smooth) and unground (rough) surfaces at the bed joint of the units are compared. Also evident in Fig. 2-6 is that for prisms with unground units, the seating effect occurs due to the crushing of local asperities on the unground bed surface as the load levels increase. Based on Atamturktur's results, this causes the vertical force to spread to a larger contact area at the bed surface. This results in the expectation that the efficiency factors (i.e., the ratio of prism compressive strength to unit compressive strength) depends on bed joint surface roughness. In studying the prisms with standard 8" × 8" × 16" CMUs, Martinez et al. (2017) have shown that the efficiency factors are approximately 0.62 for prisms with ground and 0.58 for prisms with unground units. Furthermore, under long-term (i.e., sustained) vertical loads, the compressive strength of mortarless prisms further decrease by approximately 15% when the load was

applied over seven days compared to short-term load applications (Marzahn 2000; Marzahn and Konig 2002). The short- and long-term load applications on mortarless prisms showed different compressive behavior in similar test conditions.

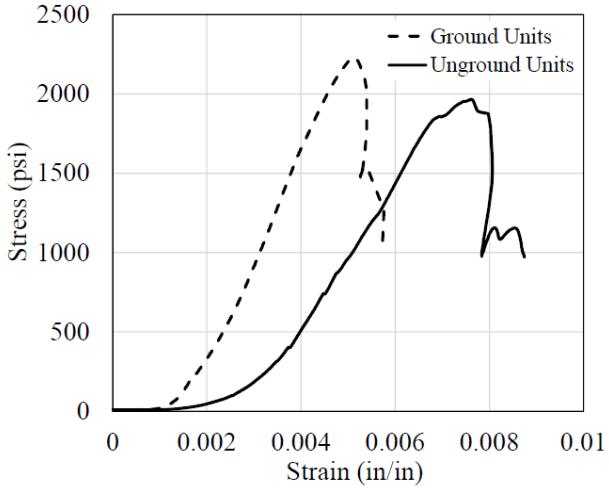

Fig. 2-6. Representative stress-strain curve of a prism with ground and unground units [Source: Atamturktur et al. 2016, with permission].

The surface roughness, in addition to being influential on the compressive capacity, also has significant influence on the shear capacity of mortarless systems. Shear failure of dry-stacked masonry prisms depends on the coefficient of friction at the bed joints, which varies according to the magnitude of compressive forces applied to the prisms. For instance, Lin et al. (2015) conducted shear tests on mortarless prisms and found that at low load levels, a 400% increase compressive force leads to an approximately 29% increase in the coefficient of friction. This increase in the compressive force is caused by a correlation between the crushing of the asperities, leading to a uniform stress distribution at the interface between the units. However, further increase in the compressive force evens the bed surface of the unis, resulting in near constant coefficient of friction based on the

research provided (Lin et al. 2015). The surface roughness is a characteristic of the bed unit surface that can change according to the load level that is subjected. This characteristic can vary in other applications of mortarless masonry, needing to extend the research towards these new areas.

In some situations, the coefficient of friction in the dry joint is not influenced by the compressive force upon the masonry structure but thermal loads. Mortarless construction with non-interlocking units is adapted as refractory ceramic lining, which is a material that retains its strength at high temperatures, in industries that utilize high temperature (such as in the fabrication of steel, furnaces, kilns, incinerators, reactors and boilers). Prisms using these ceramic units under vertical loads have been tested in a wide temperature range to investigate the effect of material stiffness and unit geometry on the dry joint closure. Results showed that the temperature increase creates thermal expansion that constraints the closure of the dry joint and the coefficient of friction by changing the stiffness of the material and by reducing the initial gap at the joint (Andreev et al. 2012, Rekik et al. 2014). It is important to look at mortarless prisms with non-interlocking units because they are one of two types of structures that this level of research has been tested on within mortarless systems; the other structural type is mortarless walls with non-interlocking units, which will be discussed in the next section.

2.3.2 Mortarless Walls with Non-Interlocking Units

Similar to the observations from prisms, studies on dry-stacked masonry walls revealed that the surface roughness of the units can reduce both compressive strength and the modulus of elasticity of these types of walls. For example, Senthivel et al. (2006)

conducted a combined experimental and numerical study on mortarless masonry walls with non-interlocking units considering incremental vertical and lateral in-plane loading. The numerical model was developed to simulate the mortarless wall as shown in Fig. 2-4-b. The study showed that when the vertical load increased by approximately 150% and a lateral in-plane load was applied, the shear capacity of the wall due to friction between the units also increased by approximately 130%. Under a monotonic lateral in-plane load application was observed two failure modes: rocking (overturning) and toe-crushing failures. Walls exhibited rocking failure at low levels of vertical load, while high levels of vertical load led to a combined rocking and toe-crushing failure. In contrast to the monotonic load, the application of a cyclic load on walls has been difficult to analyze because the opening of the units' bed joints fails to close (Vasconcelos 2005; Senthivel et al. 2005).

The experimental and numerical modeling (Fig. 2-4-b) results showed a linear behavior in the load-displacement plots of the walls at up to 30% of the peak load; however, past the 30% mark, the walls gradually lost stiffness due to relative movements at the dry-joint between the masonry units (Roca et al. 2001; Lourenco et al. 2005). Furthermore, the out-of-plane behavior on reinforced masonry walls has been experimentally and numerically studied (Fig. 2-2-a). Under proper configurations, these types of walls show ductile behavior when subjected to out-of-plane loads. A parametric analysis was used to demonstrate that the flexural capacity of the wall increased by approximately 35% and 22% as the unit and grout strength increased by 100% and 75%, respectively. In both cases, the ductility of the wall increased by approximately 150% because of the increase of

compressive strength of the material. When the yield strength of the reinforcing bars, or the reinforcement ratio, increased, the capacity of the wall increased by approximately 10%. However, in both cases the ductility of the wall decreased approximately 10% which shows the influence of the steel reinforcement in the response of the mortarless walls. Lastly, when the percentage of grouting increased, the flexural capacity increased by 53% and the displacement ductility increased by 110% (Martínez and Atamturkur 2017). These configurations show that increasing the unit and grout strength and the percentage of grouting have a ductile response as well as limiting the percentage and strength of the steel reinforcement in mortarless walls with non-interlocking units.

The term load applications, which can be either short or long term, show that there are differences between mortared and mortarless masonry walls. Tests have been conducted on full-scale masonry walls under both short- and long-term load applications (Marzahn 2000). Under short-term vertical loads, mortarless masonry walls showed higher initial deformation within approximately 30% of the failure load compared to mortared masonry walls (Langer 1992; Schubert 1995). As in the prism compressive tests, this initial deformation depended on the surface roughness at the bed joint of the units: the more uneven the bed surface, the lower the strength (Marzahn 1997). There are also calculation methods when evaluating the collapse mechanisms in mortarless masonry walls using the limit-state analysis approach.

Both the limit-state analysis approach and its extension in including the Mohr-Coulomb frictional law, are integral to understanding the draws and fallbacks to the design features on the behavior of mortarless masonry systems under a variety of load

configurations. The limit-state approach is the analysis where a structure should properly identify the mechanism by which static equilibrium is maintained. The limit-state analysis approach has been used to evaluate the strength associated with collapse mechanisms in mortarless masonry walls (Kooharian 1952; Heymn 1966; Giuffre 1989; Augusti et al. 2001; Felice and Giannini 2001). This approach assumed only rocking mechanisms of failure (i.e., flexural failure), and the masonry units were treated as rigid bodies between crack lines. A second approach proposed by D'Ayala and Speranza (2003) and Casapulla (2008) extended past the earlier research by accounting for Mohr-Coulomb frictional law, which stipulates that there is a linear relationship between the shear stress and the normal stress by the coefficient of friction of the bed surface. More recent studies on mortarless masonry walls have obtained acceptable results by applying the virtual work methodology to the in-plane and out-of-plane collapse load of the walls (Zuccarello et al. 2009; Vaculik et al. 2014). These are both important techniques and methods because they go beyond the previous research by including the Mohr-Coulomb frictional law and by looking at the collapse load of walls, which had yet to be done on the topic until their research was conducted. This research was even furthered when Ceradinit (1992) and Baggio and Trovalusci (1995) looked at the mechanical behavior of dry-stack masonry walls using solid units under lateral in-plane load.

The mechanical behavior of dry-stack masonry walls using solid units under lateral in-plane loads did further the research on the design features and behavior of mortarless masonry systems and their variable load configurations. Ceradini (1992) and Baggio and Trovalusci (1995) both conducted experimental tests and numerical analysis to study the

impact of the units' bed surface roughness on the shear strength of dry-stack masonry walls to test the imperfections of the units in the actual shear test. When imperfections of the units in the shear test were included in the numerical models, more accurate results were obtained than the previous research before it. The limit-state analysis accurately described only the walls' collapse mechanisms, however, which is a limit of the research and something that Velez et al. (2014) grappled with in their extensive research.

Mortarless masonry walls have also been studied in small-scale experiments to investigate mechanisms of collapse under seismic loads, which furthered the research for future analytical and computational developments in mortarless masonry walls. Velez et al. (2014) extensively studied forty-two different wall configurations of 1:5-scale experiment dry stone masonry, assessing the shear and flexural behavior. In many of these configurations, more than one type of failure mechanism occurred, causing sliding and rotation of different sections of the wall. The Velez et al. (2014) study provides an experimental reference for future analytical and computational developments in mortarless masonry walls under in-plane and out-of-plane loads for mortarless masonry. What may be ignored by the research is how mortarless masonry can be utilized in other industries.

In industries that utilize high temperatures, such as the steel industry, there are many applications for mortarless masonry because of its ability to accommodate high temperature. In steel ladles, the inside of the vessel consists of a large number of masonry units laid in direct contact with each other to accommodate thermal expansion in linings (Nguyen et al. 2009). Homogenization techniques can be used to describe the mechanical behavior of this kind of large, mortarless masonry structure. Researchers proposed an

equivalent material in mathematical terms which behaves similar to mortarless masonry to quickly predict the stress and strain in a temperature field. These techniques minimize the need to tediously model each masonry unit through experimentally validated numerical models because of its adaptive and accommodating features (Andreev et al. 2012; Rekik et al. 2015). This is important to the future of the topic because it shows how advantageous option could be—yet it is being under-used by professionals who could most benefit from its implementation in their fields.

2.4 Knowledge-Base on Mortarless Masonry Systems with Interlocking Structures

2.4.1 Mortarless Prisms with Interlocking Units

Studies of the surface roughness at the bed joint on prisms have focused on various types of masonry units with special interlocking characteristics such as protrusions and grooves to provide compressive, shear, and flexural capacity. Putra Block units (see Fig. 2-7) were used in compressive and shear tests on ungrouted and grouted mortarless masonry prisms (Thanoon et al. 2004; Jaafar et al. 2006a). In ungrouted mortarless prisms, the stress-strain curves results showed that the surface roughness at the bed joint was significantly affecting the compressive performance. However, in mortarless grouted prisms, structural performance improved because of the reduced effect in the initial deformations. Thanoon et al. (2008) accurately predicted not only the cracking patterns, but also the level of load and deformation in both ungrouted and grouted masonry through numerical models (recall Fig. 2-4-a). The initial softening behavior (seating effect) in ungrouted prisms was observed in stress-strain plots at up to 45% of the failure load. In addition, similar to mortared prisms, web splitting occurred in mortarless prisms at higher

stress levels in ungrouted prisms versus grouted prisms (Jaafar et al. 2006a). The compressive behavior on mortarless prisms showed that the grout within the cells of the prisms mitigated the initial deformations of the dry joint. An important aspect in the surface roughness is the determination of the shear response of masonry joints.

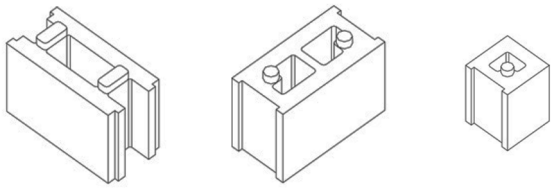

(a) (b) (c)

Fig. 2-7. Different types of Putra Block interlocking units (a) stretcher; (b) corner; and half units [Source: Thanoon et al. 2008, with permission].

Extending the research on the impact of the shear response on surface roughness in mortarless prisms, shear tests were conducted using Putra Block units under different compressive loads to investigate the shear behavior at the bed joint (Al-Wathaf et al. 2005). The results indicated that the frictional behavior of interlocking mortarless joints under compression can be represented by the Mohr-Coulomb friction law. The surface roughness impacted the shear performance at low levels of compressive loads, reducing the shear strength due to the bed joint area for friction resistance was not fully utilized. When the compressive load increased by approximately 64%, the shear strength increased by approximately 60% (Al-Wathaf et al. 2005). Other metrics (e.g., efficiency factors) have been used on mortarless prisms to quantify the response under under vertical loads.

The impact of the surface roughness was investigated on modified H and Whelan-Hatzinikolas-Drexel (WHD) and units on prisms under vertical loads (see Fig. 2-8). Oh (1994) conducted experimental and numerical studies on prisms (recall Fig. 2-3) using

these interlocking units. The compressive test revealed that the efficiency factors found for prisms using modified-H units were 0.35 and WHD units were 0.50, compared to 0.61 for mortared prisms. Oh (1994) also found that the surface roughness influenced the location of failure in prisms, which differed from its location in mortared prisms. The lack of filler material in the interlocking masonry and the nature of the surface roughness between units' dry joints altered the failure mechanism.

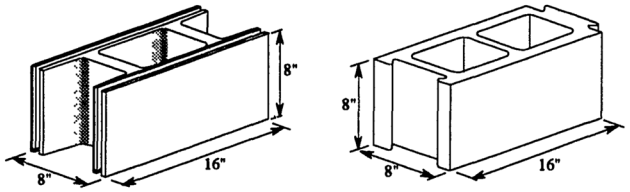

(a) (b)

Fig. 2-8. Masonry system: (a) Modified H-Block unit; (b) WHD Block unit [Sources: Oh 1994, with permission].

Investigations on mortarless prisms using interlocking Hydraform units (see Fig. 2-9) under vertical loads have shown similar compressive behavior to mortared prisms in which the compressive strength of the prisms increased by approximately 130% with an increase in unit strength by approximately 360% (Uzoegbo and Pave 2005; Ngowi 2005; Pave 2007). Compressive tests on prisms with Hydraform units showed that efficiency factors were between approximately 0.20 and 0.40 for mortarless prisms, and between 0.75 and 0.98 for mortared prisms. The failure pattern formed two parallel vertical cracks along the end shells of the prisms with Hydraform units, compared to an X-shaped crack in mortared units (Ngowi 2005). Results also revealed that the mortarless prisms composed of four-stacked units had a compressive strength that was approximately 30% higher than the compressive strength of similarly constructed mortared prisms. However, in terms of

ultimate compressive load, mortared prisms were deemed superior by approximately 65% to mortarless prisms due to differences in the contact area between the two prisms (Pave 2007). However, this study did not look at the prisms after compressive tests to determine their efficiency through eccentric and concentric loads.

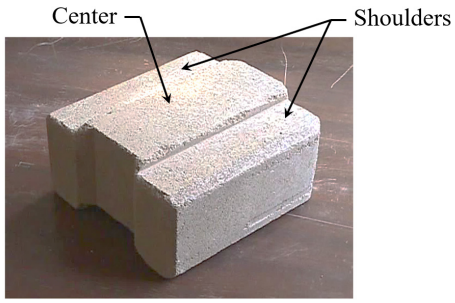

Fig. 2-9. Hydraform unit [Source: Ngowi 2005, with permission].

Compressive tests were conducted on prisms with SILBLOCK-1 and SILBLOCK-2 units (see Fig. 2-10) under concentric but also eccentric vertical loads, to determine the prisms' response (Anand and Ramamurthy 2000; Anand and Ramamurthy 2005; Ferozkhan 2005; Thanoon et al. 2007). The concentric compressive tests found that efficiency factors in the mortarless prisms were between 0.60 and 0.80, while the efficiency factors in the mortared prisms were between 0.30 and 0.40. Early vertical splitting of the units in mortared prisms by biaxial tensile stresses led to the low efficiency factors; however, this effect was different in mortarless prisms, in which the first crack occurred at approximately 71-74% of the failure load. As in prisms under concentric vertical loads, results on eccentric loads on prisms with SILBLOCK-1 and SILBLOCK-2 units exhibited a relatively lower reduction in the capacity of approximately 10% of the concentric capacity, while mortared prisms conducted by Drysdale and Hamid (1983) reduced 29%

its capacity. These prisms with interlocking units advantaged mortared prisms under concentric and eccentric loads.

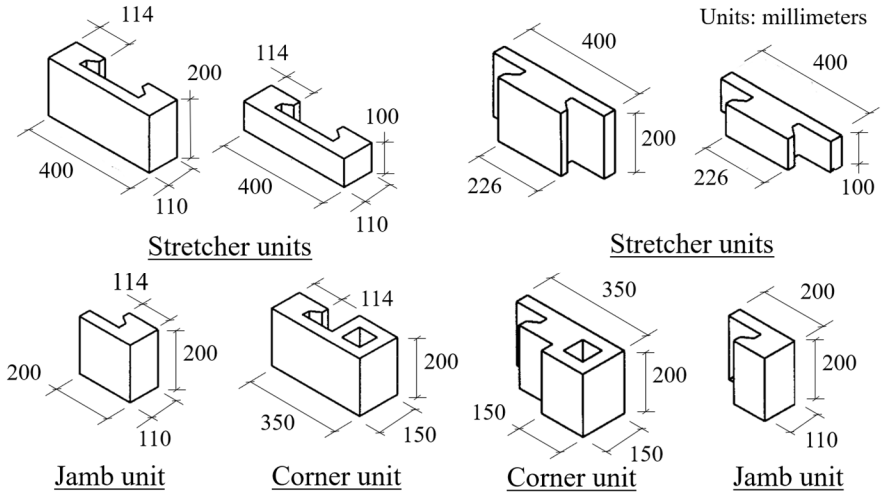

Fig. 2-10. Details of (a) SILBLOCK-1 and (b) SILBLOCK-2 system [Source: Anand and Ramamurthy 2000, recreated with permission].

Mortarless prisms with QuickBlock units (see Fig. 2-11) were also tested under concentric and eccentric vertical loading and showed a more varied response than the SILBLOCK reactions above (Ferozkhan 2005). These tests found efficiency factors between 0.79 and 0.92 under concentric vertical loads, with the primary failure being caused by the splitting of web shells along the height of the prisms. However, under eccentric vertical loads, the primary failure occurred in the face shell, followed by the splitting of the web. More specifically, at low relatively eccentricities, failure in the prisms occurred at approximately 72% of the concentric failure load. Under relatively high eccentricities, this failure occurred at approximately 44% of the concentric failure load (Ferozkhan 2005). In short, these results follow a different approximate percentage of the concentric and eccentric failure load between SILBLOCKS and QuickBlocks—but the

information does not have the much-needed dialogue on how grouting within the cells would affect mortarless masonry prisms.

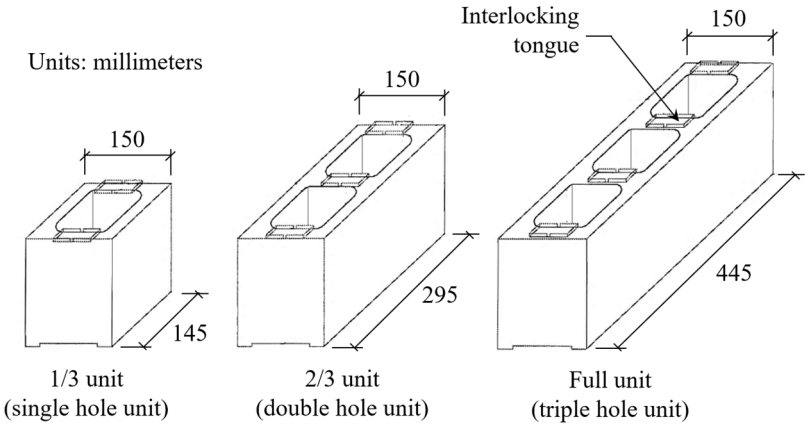

Fig. 2-11. Geometry of interlocking QuickBlock units [Source: Ferozkhan 2005, recreated with permission].

Extending the investigation of concentric and eccentric vertical loading on interlocking units, mortarless masonry prisms with HILBLOCK units (see Fig. 2-12) were studied both with grouting and without grouting within the cells (Anand and Ramamurthy 2005). Concentric compressive tests on mortarless prisms resulted in efficiency factors of 0.62 and 0.68 for ungrouted and grouted prisms, respectively, while efficiency factors for mortared prisms were 0.83 and 0.85 for ungrouted and grouted prisms. As these results indicated, compared to ungrouted mortarless prisms, the compressive strength of grouted mortarless prisms increased by approximately 9%. In addition, these eccentric tests on ungrouted mortarless prisms showed similar behavior to grouted mortarless prisms. Under low eccentricities, the failure in the mortarless prisms occurred at approximately 75% of the concentric failure load. Under high eccentricities, this failure occurred at approximately

50% (Anand and Ramamurthy 2005). This information was furthered in the 2016 research by Tang et al. in their study on the shear behavior under various dynamic loads of mortarless prisms with coconut-fiber reinforced concrete (CRFC).

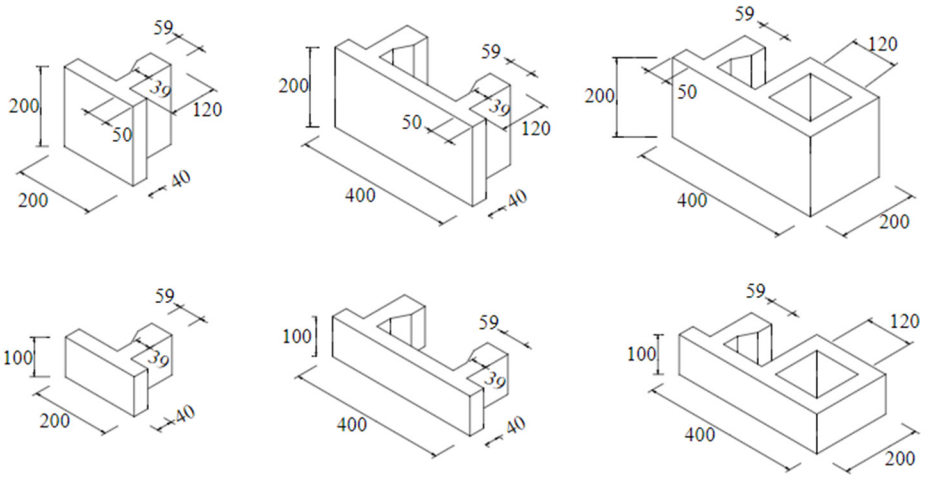

Fig. 2-12. Dimensional details of HILBLOCK [Source: Anand and Ramamurthy 2005, with permission].

The shear behavior under various dynamic loads has been studied in mortarless prisms containing coconut-fiber reinforced concrete (CFRC) units to determine their residual capacity after dynamic loadings (Tang et al. 2016). Prisms with CFRC units have been found to have an adequate residual capacity after being subjected to a number of dynamic loads. Further studies on the shear behavior of prisms with interlocking mortarless units with different shapes were conducted under cyclic loading (see Fig. 2-13). The circular interlock was the most efficient system since it was able to absorb more in-plane energy dissipation (Liu et al. 2016). Similar tests also showed that joints between units exhibited Mohr-Coulomb frictional behavior and that the coefficients of friction were significantly affected by compression load levels (Lourenco and Ramos 2004). This

research provided insights of the behavior of alternative materials to the masonry unit and the geometry of the interlock for a better response that can be extended to a wall.

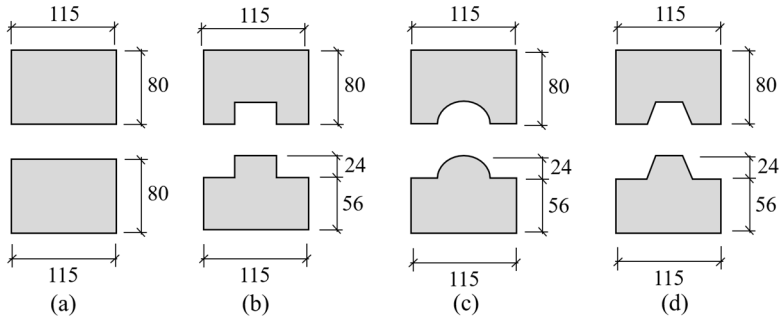

Fig. 2-13. Dimensions and profiles of the cross-section of units with various interlocking shapes: (a) non-interlocking; (b) rectangular interlocking; (c) circular interlocking; (d) trapezoidal interlocking (Units: mm) [Source: Liu et al. 2016, recreated with permission].

2.4.2 Mortarless Walls with Interlocking Units

To further the current knowledge about the behavior of masonry structures, similar types of experiments and numerical models have been conducted on walls using interlocking units. Beall (2000) indicated that the physical interlocking feature improves the accuracy of mortarless masonry systems; it facilitates the straight vertical alignment of the wall and, therefore, expedites construction. However, the effect of the surface roughness at the dry joints in mortarless walls requires further research. Furthering the research of Beall (2000), Kintingu (2009) investigated these effects by using interlocking units during the construction process. The effects of unit surface roughness on wall alignment were found to be the primary issue in mortarless walls since the load path can lead to a non-uniform distribution of stresses. However, the self-aligning properties of interlocking units within the allowance limits can decrease the need for skilled labor and increase both productivity and cost savings by approximately 50% (Whelan 1985; Hines

1993; Anand and Ramamurthy 2003). Some potentials of interlocking units can be seen in mortarless walls using Putra Block units under flexural and seismic loads.

Flexural behavior can be investigated by examining the response of mortarless masonry walls under eccentric vertical loads. Analysis of these walls conducted using Putra Block units (see Fig. 2-7) revealed that wall stiffness increased after 30% of the ultimate load was applied (Najm 2001). As with research on other types of units, this increase was attributed to a gradual closing of the interlocking joints (Thanoon et al. 2004). In addition, when the eccentricities increased by approximately 55%, the flexural strength of the walls decreased by approximately 25% (Thanoon et al. 2007). Further parametric analysis using numerical models (Fig. 2-4-c) investigated variations in the amount of vertical force and the slenderness ratio of the walls. The results showed that increasing vertical loads enhanced the bending capacity of the wall, and when the slenderness ratio of the walls increased, the bending capacity of the walls decreased (Safiee et al. 2011b). Hejazi et al. (2015) studied the lateral in-plane behavior through numerical models (Fig. 2-5) and conducted a time-history analysis of the walls using earthquake data from the Indonesian (PGA=0.39g) and Malaysian (PGA=0.15g) earthquakes. The results showed that the mortarless masonry wall using Putra Block units could have withstood the Malaysian earthquake because it experienced reasonably low deformation and stress. It also concluded that Putra Block units could be used in dry-stack masonry walls located in low seismic areas. Flexural strength is an important indicator for the structural integrity of mortarless masonry walls in which the lateral out-of-plane loading orientation can affect the response of the wall.

A similar study focused on the flexural behavior was conducted on Hydraform units (Fig. 2-9) under vertical and lateral out-of-plane loading (Uzoegbo 2003; Uzoegbo and Ngowi 2003; Elvin and Uzoegbo 2011). Test results have shown that compared to mortared masonry walls, the compressive capacity of mortarless masonry walls decreased by approximately 35% (Uzoegbo et al. 2007). This failure was characterized by the formation of a vertical crack parallel to the centerline of the wall. In addition, mortarless masonry walls under out-of-plane loading parallel (i.e., vertical bending) or perpendicular (i.e., horizontal bending) to the bed joints exhibited characteristics similar to mortared masonry walls in their flexural strength. Compared to those under loading parallel to the bed joints, both mortared and mortarless walls under loading perpendicular to the bed joints showed a 700% higher flexural strength (Ngowi 2005; Elvin and Uzoegbo 2011). To better improve the flexural behavior in mortarless walls, researchers have been searching for a way to use new integrations in the units.

A novel technique integrating natural fiber with cement composites in the masonry unit has been proposed to improve the flexural behavior in mortarless walls (Aziz et al. 1981; Baruah and Talukdar 2007). For example, Ali et al. (2012) took this technique and developed interlocking keys on units made of coconut-fiber reinforced concrete (CFRC) to resist in-plane and out-of-plane loads (see Fig. 2-14). These units also had the distinction of restricting uplift, which was ensured by a rope that vertically ran through the two holes in the units. Based on experimental compressive tests, these mortarless masonry walls with CFRC units were found to have a compressive strength of approximately 96% of the compressive strength of an individual unit. When compared to walls without ropes, those

with ropes indicated decreased relative upper displacement and base shearing. Nevertheless, one significant limitation of the ropes was that they lost tension over time. For this reason, future studies of these structures are warranted (Ali et al. 2013). However, there were other researchers who looked at how the bed joints affected the flexural capacity of the ungrouted and grouted mortarless masonry units.

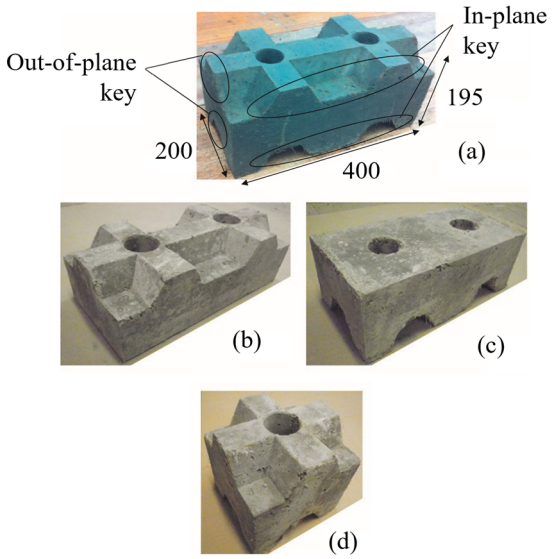

Fig. 2-14. CFRC interlocking units: (a) standard; (b) bottom; (c) top; and (d) half unit [Source: Ali et al. 2011, with permission].

Similar research was conducted using HILBLOCK (Fig. 2-12) and AZAR Block (Fig. 2-15) units on mortarless masonry walls in both parallel bed joint loading tests and perpendicular loading tests. When parallel, as opposed to perpendicular, loads were applied to the bed joints, the flexural capacity of both ungrouted and grouted HILBLOCK units increased by approximately 75% and 60%, respectively (Anand and Ramamurthy 2005). In contrast to HILBLOCK units, mortarless masonry walls using AZAR Block units increased their flexural capacity by approximately 5% when perpendicular, rather than

parallel, loading was applied to the bed joints (Drysdale 2000). Mortarless walls using HILBLOCK and AZAR Block units has not been tested when grout is added as design parameters. However, grouted mortarless walls using G.R. units have been tested with the purpose of better understand the role of grouting in the behavior of the walls.

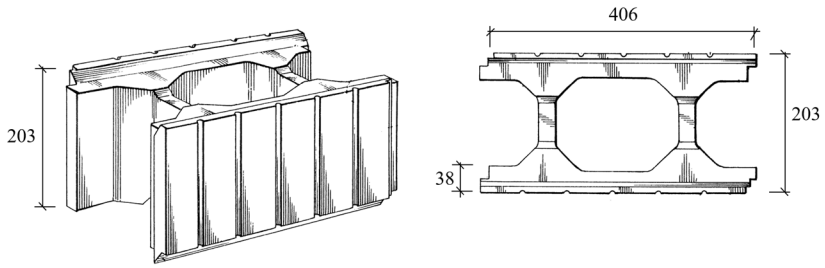

Fig. 2-15. AZAR Block, isometric and plan view (units: mm) [Source: Drysdale 2000, recreated with permission].

Partially and fully grouted mortarless walls were experimentally tested and numerically simulated to study their behavior under vertical loads as well as loading perpendicular or parallel to the bed joint using G.R. units (see Fig. 2-16) (Hatzinikolas et al. 1986). The experimental results showed that compared to ungrouted walls, the compressive strength of partially and fully grouted walls increased by approximately 16% and 38%, respectively. When the ultimate compressive load was reached, cracking at the face shell occurred sooner in the partially and fully grouted walls than the ungrouted walls. In addition, compared to loading parallel to the bed joints, loading perpendicular increased their flexural capacity by approximately 120%.

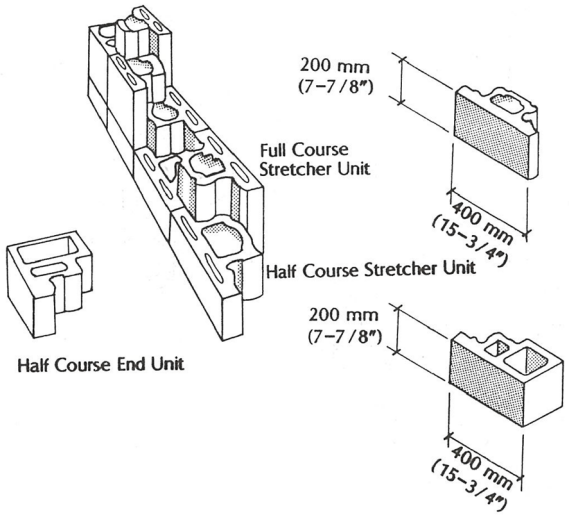

Fig. 2-16. General views of the G.R. unit [Source: Hatzinikolas et al. 1986, with permission].

2.5 Knowledge-Base on Mortarless Masonry Systems with Alternative Methods

Research exploring methods of mortarless construction has led to improvements in the structural performance of the system, as a whole. For example, experimental tests of pre-stressed reinforcement elements and surface bonding have been conducted to investigate the effect of these methods on structural strength; however, numerical modeling has not been widely applied in the current literature to enhance the understanding of these systems. This section discusses the previous work conducted using these alternative methods.

2.5.1 Mortarless Pre-Stressed Masonry Systems

One method to improve the structural performance of mortarless masonry is pre-stressed reinforcement elements within the walls. Pre-stressing can be applied with non-interlocking and interlocking units. Biggs' (2002) early research conducted shear tests on the walls using FlexLock units (see Fig. 2-17). The results of the tests indicated a lower

shear capacity than mortared systems due to the low levels of pre-stressing and the reduction of the coefficient of friction in the contact between units. Biggs and Forsberg (2006) conducted further research on walls using the FlexLock system, focusing on its constructability as applied to a full-scale house. In their assessment, these researchers concluded that using the FlexLock system instead of a mortared system would reduce the cost of construction by approximately 25%, in addition to increasing worker productivity by almost 120%. This research did not yet include Bolt-A-Blok systems to compare the flexural capacity of the walls.

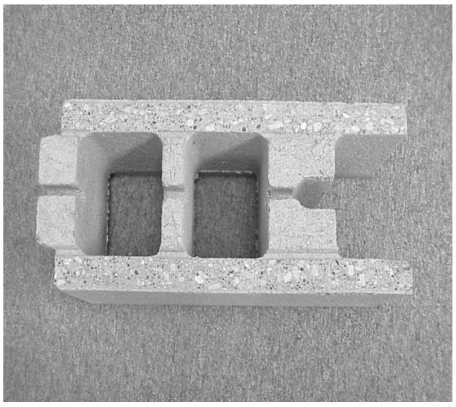

Fig. 2-17. Stretcher FlexLock unit [Source: Biggs 2002, with permission].

Research on pre-stressed mortarless masonry studies was extended to include Bolt-A-Blok systems to determine the displacement ductility (Ota 2011). These walls were used under in-plane and out-of-plane loads to mathematically analyze the behavior of the system and determine the adjustments needing to be made to existing design equations in the MSJC 2008. Based on these results, the flexural capacity of these walls was found to be comparable to reinforced mortared masonry walls. In addition, these mortarless walls exhibited significantly higher displacement ductility. This research was nuanced by the

2007 Yamaguchi et al. research that focused more strictly on the reinforced unbonded elements in masonry walls.

Yamaguchi et al. (2007) focused on the friction-resistant stress-transfer mechanism, a system containing reinforced unbonded elements in masonry walls, thus allowing for easy reuse of the materials (see Fig. 2-18). This system was used in full-scale houses that were subsequently subjected to a magnitude seven earthquake approximately one hundred days after construction. They showed no signs of structural damage. Furthermore, approximately 1200 days later, these structures still showed only a limited pre-stress loss of 20%. The research conducted by Yamaguchi et al. (2007) did not, however, focus on the importance of variations in grout level.

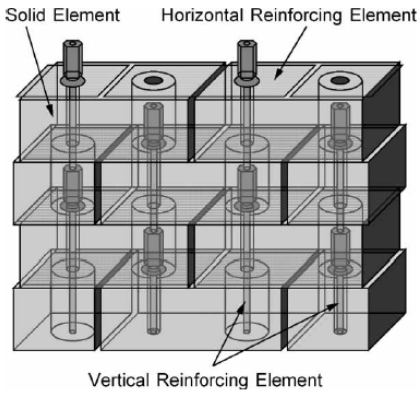

Fig. 2-18. Pre-stressed system for dry-stack masonry walls [Source: Yamaguchi et al. 2007, with permission].

Pre-stressed mortarless masonry has also been studied in grouted and ungrouted walls using both AZAR Block and Spar-lock units to assess their behavior under out-of-plane loads (Sokairge et al. 2017). Based on the results of both units, grouted pre-stressed walls resisted twice the failure load of ungrouted pre-stressed walls. Additionally, these grouted walls had a cracking load three times greater than that of reinforced masonry walls

with grout. Walls tested using either the AZAR or Spar-lock units were found to resist lateral out-of-plane loading both with and without grouting. However, their results indicated that the ungrouted pre-stressed masonry wall exhibited shear failure under out-of-plane loads, implying that the equation's design in the current MSJC code requires revision for pre-stressed dry-stack masonry walls. The current research on pre-stressed mortarless walls lacks numerical models to predict their response. In addition, it is important to note that all studies on these walls recommended further experiments to validate the results. Pre-stressed dry-stack systems are a relatively new construction method, requiring further investigation to be incorporated fully into the MSJC code.

2.5.2 Mortarless Masonry Using Surface Bonding

A method for enhancing the structural performance of dry-stack masonry is by using surface bonding. For example, Ferozkhan (2005) conducted compressive tests on walls using QuickBlock units that included fiber-reinforced cement composite (FRCC) on the faces of the wall. Ferozkhan found that this surface bonding increased the compressive strength of mortarless masonry walls compared to mortared walls. Based on these tests, Ferozkhan reported that walls with FRCC surface bonding exhibited less damage, including a significant reduction in cracking. In addition, these walls exhibited approximately 20% greater compressive strength than walls without surface bonding. This can be furthered by research on the compressive and shear capacities of dry-stack masonry walls.

The compressive and shear capacities of dry-stack masonry walls with surface bonding have been studied with a specific focus on ENDURA units (see Fig. 2-19). For

example, Murray (2007) conducted compressive tests on mortarless walls. When the walls reached the failure load, the researchers removed the surface bonding from the walls to document the damage to the structure. Some units displayed significant concentrations of cracking and crushing along the top and bottom units of the walls. However, Murray found inconsistencies between the compressive capacities of these walls with and without a thin layer of mortar along their bed joints. Further tests related to the compressive behavior of the walls are recommended. Beyond this, Eixenberger and Fonseca's (2016) research furthered this because it looked at how grouting, reinforcement, and shear capacity seem to be affected by each other.

More recently, Eixenberger and Fonseca (2016) conducted shear tests that showed that as the percentage of grouting and reinforcement increased, the shear capacity increased as well. Subsequently, comparing their results with equations from the MSJC and the International Code Council (ICC) equations, the researchers concluded that the MSJC equations overestimated and the ICC underestimated the shear capacity of the walls. In a later study, Eixenberger (2017) concluded that ENDURA units provided limited shear resistance; however, grout within the cells and surface bonding played important roles in determining the shear strength of the walls.

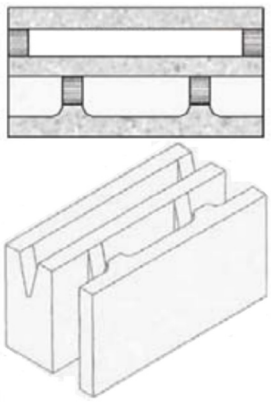

Fig. 2-19. Concrete units used in dry-stack system [Source: Murray 2007, recreated with permission].

These new masonry technologies and construction methods focus on pre-stressed and surface bonding mortarless masonry to reduce the need for highly skilled masons, allowing for faster construction and increasing structural performance.

2.6 Future Directions

A combination of experimental tests and numerical models of mortarless structures is needed because numerical models that are validated against experimental data can be used to explore further a wide range of untested scenarios. This combination is essential to assess, optimize, and better understand mortarless masonry systems—as has been discussed, at length throughout this literature review. Relevant studies from past years have combined the experimental tests and numerical modeling (brought up above) to make extraordinary progress in the availability of information on mortared and mortarless masonry; however, there is significant room for advancements in the coming years, such as:

(1) Dry-stack masonry has several advantages over mortared masonry, including a reduction in construction time, costs, and the amount of wet materials needed. The common methods to compensate for the lack of mortar in masonry systems include: using non-interlocking and interlocking units that can be grouted and reinforced. Other alternatives that enhance structural performance can include adding surface bonding agents and using pre-stressed reinforcement elements. The dry-stack construction system presents a myriad of design opportunities with essentially infinite variations in the interlocking units, surface treatment and reinforcement abilities. This new design configuration requires further investigation and improved methods to predict the structural behavior of these masonry systems. Previous research shows that such design variations can cause significant changes in the behavior of the system. Hence, a more thorough understanding of the effect and sensitivity of various design decisions on mortarless masonry systems is needed. Several variables should be explored, including: (i) the change in the coefficient of friction in the presence of simultaneous vertical and lateral loads; (ii) the aspect ratios of walls; (iii) the effects of various percentages of reinforcement and grouting; (iv) the effects of different thicknesses of surface bonding; and (iv) the effects of various types of interlocking units.

(2) Only a limited number of studies have considered the effect of the variability of the unit material. Several material properties that exhibit natural variability should be explored with probabilistic models. This study can include a detail study of the surface roughness and the microscopic distribution of the asperities in the bed surfaces area of the units.

(3) Future studies are needed to develop mitigation strategies for reducing contact surface irregularities between units. For instance, dry-stack masonry prisms tend to have relatively higher initial deformations when subjected to vertical loads of up to approximately 30% of the failure load of prisms. This can result in stiffness in the response at low levels of applied loads. Dry-stack masonry prisms exhibit stable compressive behavior after the units are settled because, when loading is increased, the contact area at the interface is greater. This increases the stiffness of the prism. One potential solution to this is to ground the bed surfaces to reduce roughness and eliminate the large deformations that result from the crushing of the rough surface. Future studies are needed to investigate this concept and its potentially negative effect on the shear capacity of the system due to the reduced coefficient of friction between the units.

(4) Dry-stack systems have been tested with a thin layer of mortar between units, which tends to have a minor impact on masonry performance. Instead of a thin layer of mortar, an alternative strategy is the application of low-cost, easy-to-lay (e.g., sprayable, spreadable with a foam gun) bonding material between units. Studies on such materials must include tests to determine the mechanical properties of these bonding materials.

(5) Multiple studies show that the efficiency factor of dry-stack masonry systems can be represented by the ratio of the compressive strength of a masonry prism to the compressive strength of a single unit. For mortared masonry systems, the maximum efficiency factor has been found to be approximately 0.98. This review found that the average efficiency factor was approximately 0.65 for non-interlocking systems and ranged from 0.20 to 0.92 for interlocking systems depending on the type of unit.

However, for surface bonding and pre-stressed reinforcement elements, the information is unavailable in the available literature.

(6) Dry-stacked masonry systems need to be studied under different geometric configurations to include one- and two-way behavior of walls. It also needs to be studied when looking at the "one- and two-way behavior of windows and door openings from within the wall. Moreover, research on the shear capacity of dry-stack masonry remains inconclusive because of the complex behavior of the friction contact between units during the loading process. Dynamic loads on mortarless masonry walls need to be studied to assess their behavior in high-seismic zones.

(7) Recent studies have shown that pre-stressed dry-stack masonry systems can withstand vertical, in-plane, and out-of-plane loads. However, the capacity of the systems relies on the kind of surface contact between units. Uneven contact between units creates instabilities during the pre-stressing process, leading to a reduced load capacity. In addition, researchers have found that typical equations in building codes are not applicable to pre-stressed dry-stack masonry systems. Efforts towards the adjustments of those equations are needed for design purposes.

(8) Additional research is needed in a wide range of design configurations to determine the compressive, shear, and flexural capacities of dry-stack masonry systems so that researchers can establish design guidelines for the practical use of such systems.

2.7 Conclusions

Based on this general overview of the research on mortarless prisms and walls through experimental tests and numerical modeling, it is evident that important advances

in the numerical modeling have occurred in the last three decades. However, the numerical simulations of mortarless masonry has encountered challenges in the description of the behavior of dry joints due to high local non-uniform distribution of stresses developed in the bed joint between the units. This complex behavior generates a nonlinear response with initial deformations and different failure patterns to mortared systems. A limited set of numerical models has been developed to describe the mortarless behavior with different levels of accuracy in their predictions. The validation process of numerical models, based on a comparison with experimental data is necessary to ensure the reliability of the numerical models and their capacity to predict the structural response. The extent of research effort in masonry structures is presented herein with a strong emphasis on mortarless structures. The importance of this review comes from the need to have a clear understanding of the behavior of different design configurations on mortarless structures. This research accomplishes to contribute to the masonry field by identifying barriers preventing the codification of these systems and proposing future investigation with the purpose to enrich the knowledge about mortarless masonry.

References

Ahmad, S., Hussain, S., Awais, M., Asif, M., Muzamil, H., Ahmad, R., and Ahmad, S. (2014). "To Study the Behavior of Interlocking of Masonry Units/Blocks." *Journal of Engineering*, 4(3), 39-47.

Ahmed, Z., Othman, S. Z., Yunus, M., and Mohamed, A. (2011). "Behavior of Masonry Wall Constructed using Interlocking Soil Cement Bricks." *International Journal of*

Civil, Environmental, Structural, Construction, and Architectural Engineering, 5(12), 804-810.

Ali, M., Gultom, R., and Chouw, N. (2012). "Capacity of Innovative Interlocking Block under Monotonic Loading." *Construction and Building Materials*, 37(1), 812-820.

Ali, M., Briet, R., and Chouw, N. (2013). "Dynamic Response of Mortar-Free Interlocking Structures." *Construction and Building Materials*, 47(1), 168-198.

Al-Manaseer, A. A., and Neis, W. V. (1987). "Load Tests on Post-Tensioned Masonry Wall Panels." *Structural Journal*, 84(6), 467-472.

Al-Wathaf, A. (2006). "Development of Finite Element Code for Non-Linear Analysis of Interlocking Mortarless Masonry System." *Ph.D. dissertation*, Universiti Putra Malaysia.

Al-Wathaf, A. (2009). "3D Finite Element Analysis of Hollow Concrete Block Masonry." *Journal of Science and Technology*, 14(2), 1-10.

Al-Wathaf, A., Thanoon, W., Jaafar, M., Noorzaei, J., and Kadir, M. (2005). "Shear Characteristic of Interlocking Mortarless Block Masonry Joints." *Masonry International*, 18(1), 39-44.

Anand, K., and Ramamurthy, K. (2000). "Development and Performance Evaluation of Interlocking - Block Masonry." *J. Archit. Eng.,* 6(2), 45-51.

Anand K.B. and Ramamurthy K. (2003). "Laboratory-Based Productivity Study on Alternative Masonry Systems." *ASCE Journal of Construction Engineering and Management*, 129(3), 237-242.

Anand, K., and Ramamurthy, K. (2005). "Development and Evaluation of Hollow Concrete Interlocking Block Masonry System." *The Masonry Society Journal*, 23(1), 11-20.

Andreev, K., Sinnema, S., Rekkik, A., Allaoui, S., Blond, E., and Gasser, A. (2012). "Compressive Behavior of Dry Joints in Refractory Ceramic Masonry." *Construction and Building Materials*, 34(1), 402-408.

Arifuzzaman, S., and Saatcioglu, M. (2012). "Seismic Retrofit of Load Bearing Masonry Walls by FRP Sheets and Anchors Sheets and Anchors." In *Proceedings of the 15th World Conference on Earthquake Engineering*, Lisboa, Portugal.

Atamturktur, S., Ross, B., Thompson, J., and Biggs, D. (2016). "Compressive Strength of Dry-Stacked Concrete Masonry Unit Assemblies." *Journal of Materials in Civil Engineering*, 29(2), 1-4.

Augusti, G., Ciampoli, M., and Giovenale P. (2001). "Seismic Vulnerability of Monumental Buildings." *Structural Safety,* **23(1)**, 253-274.

Aziz, M.A, Paramasivam P., and Lee S.L. (1981). "Prospects for Natural Fibre Reinforced Concretes in Construction." *Int. Journal of Cement Composite Lightweight Concrete*, 3(2), 123-132.

Baggio, C., and Trovaluski, P. (1993). "Discrete Models for Joined Block Masonry Walls." *Proc. 6th North American Masonry Conf.*, 939-949.

Baggio, C., and Trovaluski, P. (1995). "Stone Assemblies under In-plane Actions, Comparison between Nonlinear Discrete Approaches." *Computer Methods in Structural Masonry*, 3(1), 184-193.

Baruah P., and Talukdar S.A. (2007). "Comparative Study of Compressive, Flexural, Tensile and Shear Strength of Concrete with Fibres of Different Origins." *Ind. Concrete Journal*, 81(7), 17-24.

Beall C. (2000). "New Masonry Products, Materials." *Progress in Structural Engineering and Materials*, 2(1). 296-303.

BIA. (1996). "Reinforced Brick Masonry – Introduction," *The Brick Industry Association*, Technical Notes 17, 1-7.

Biggs, D.T. (2002). "Development of a Mortarless Post-Tensioned Masonry Wall System." *Proceedings of the Sixth International Masonry Conference*, 28-32.

Biggs D.T., and Forsberg, T.E. (2008). "A Mortarless Prestressed Masonry House: Case Study." *Proceedings of the 14th International Brick and Block Masonry Conference,* Sydney, Australia, 1-11.

Bosiljkov, V., Page, A., Bokan-bosiljkov, V., and Žarnic, R. (2003). "Performance Based Studies of In-Plane Loaded Unreinforced Masonry Walls." *Masonry International*, 16 (2), 39-50.

Carol, I. and López, C. (1999). *Failure Analysis of Quasi Brittle Materials using Interface Elements*, Mechanics of Quasi-Brittle Materials and Structures. Hermes Science Publications. Paris, France.

Carreira, D.J. and Chu, K. H. (1985). "Stress-Strain Relationship for Plain Concrete in Compression." *Journal Proceedings*, 82(6), 797-804.

Casapulla, C. (2008). "Lower and Upper Bounds in Closed Form for Out-of-Plane Strength of Masonry Structures with Frictional Resistances." *In Proceedings of the* 6th

International Conference on Structural Analysis of Historical Constructions, Bath, UK, London, England: CRC Press, Chapter 137, 1191-1206.

Ceradini V. (1992). "Modeling and Experimentation for the Study of Historic Structures." *PhD. Dissertation*, Università degli Studi di Roma. Roma, Italy.

Cuadra, C. H. (2012). "Seismic Vulnerability of Santo Domingo Church, Cusco, Peru." *In Proceedings of the 15th World Conference on Earthquake Engineering*, Lisbon, Portugal.

Dawe, J. L., and Aridru, G. G. (1992). "Posttensioned Concrete Masonry Walls Subjected to Uniform Lateral Loadings." *In Proceedings of the 6th Canadian Masonry Symposium,* 201-212.

D'Ayala, D. and Speranza, E. (2003). "Definition of Collapse Mechanisms and Seismic Vulnerability of Historic Masonry Buildings." *Earthquake Spectra*, 19(3), 479-509.

Drysdale, R. G., and Hamid, A. A. (1983). "Capacity of Concrete Block Masonry Prisms under Eccentric Compressive Loading." *ACI Journal*, 80(11), 102-108.

Drysdale, R. (2000). "Properties of Surface-Bonded AZAR Dry-Stack Block Construction." *AZAR Group of Companies*. Windsor, Ontario.

Dyskin, A. V., Pasternak, E., and Estrin, Y. (2012). "Mortarless Structures Based on Topological Interlocking." *Frontiers of Structural and Civil Engineering*, 6(2), 188-197.

Eixenberger, J.G. (2017). "Seismic Analysis of and Provisions for Dry-Stack Concrete Masonry Wall Systems with Surface Bond in Low-Rise Buildings." *PhD. Dissertation*, Brigham Young University, UT.

Eixenberger, J.G. and Fonseca, F.S. (2016). "Shear Strength of Dry-Stack Masonry Walls." *Brick and Block Masonry-Trends, Innovations and Challenges*. Taylor and Francis Group, 1539-1544

Elvin, A. and Uzoegbo, H. C. (2011). "Response of a Full-Scale Dry-Stack Masonry Structure Subject to Experimentally Applied Earthquake Loading." *Journal of the South African Institution of Civil Engineering*, 53(1), 22-32.

Felice, G. D., and Giannini, R. (2001). "Out-of-Plane Seismic Resistance of Masonry Walls." *Journal of Earthquake Engineering*, *5*(2), 253-271.

Ferozkhan, M. (2005). "Development of a Dry Stack Masonry System for Effective Resistance to Out-of-Plane Bending." *M.S. Thesis*. Central Queensland University, Australia.

Ferozkhan, M., Dhanasekar, R., Holt, W., and Dhanasekar, M. (2004). "Behavior of Drystack Masonry Wallettes under Axial Compression." *In Proc. 13th International Brick and Block Masonry Conference*. Amsterdam, Netherlands.

Giuffrè, A. (1989). *Letture Sulla Meccanica delle Murature Storiche* [In Italian]. Rome, Italy. Edizioni Kappa, 85-94.

Glitza, H. (1991). "State of Art and Tendency of Development of Masonry without Mortar." *Brick and Block Masonry*, 2, 1028-1033.

Hamid, A. (2004). "Development of a New Loadbearing Masonry Wall System for Building Construction in Hot Climate." *13th International Brick and Block Masonry Conference.* Amsterdam, Netherlands.

Hamid, A., Abboud, B., and Harris, H. (1985). "Direct Modeling of Concrete Block Masonry under Axial Compression." *Masonry: Research, Application, and Problems*, 1(1), 151-166.

Haynes, B. C. and Simons, J. W. (1976). "Construction with Surface Bonding." *Agriculture Information Bulletin, No. 374*, U.S. Department of Agriculture.

Hatzinikolas, M., Elwi, A., and Lee, R. (1986). "Structural Behavior of an Interlocking Masonry Block." *In Proc. 4th Canadian Masonry Symposium.* University of Alberta, 225-239.

Hejazi, F. (2015). "Seismic Analysis of Interlocking Block in Wall-Foundation-Soil System." *Challenges, Opportunities and Solutions in Structural Engineering and Construction*. Taylor and Francis Group, 351-356.

Heyman J. (1966). "The Stone Skeleton." *Int. J. Solids Struct*, 2(1), 249-279.

Hines, T. (1993). "Benefits of Dry-Stack Interlocking Concrete Masonry as a Component of Cost Effective Construction." *In Proc. 6th North American Masonry Conference*, 849-861.

Hussein, A. S., and El-Shishiny, H. (2009). "Influences of Wind Flow over Heritage Sites: A Case Study of the Wind Environment over the Giza Plateau in Egypt." *Environmental Modelling & Software*, 24(3), 389-410.

Jaafar, M., Al-Wathaf, A., Thanoon, W., Noozaei, J., and Abdulkadir, M. (2006a). "Behavior of Interlocking Mortarless Block Masonry." *Construction Materials*, 159(3), 111-117.

Jaafar, M., Thanoon, W., Najm, A., Abdulkadir, M., and Ali, A. (2006b). "Strength Correlation between Individual Block, Prism and Basic Wall Panel for Load Bearing Interlocking Mortarless Hollow Block Masonry." *Construction and Building Materials*, 20(7), 492-498.

JNE Consulting Ltd. (2006). "Design and Construction Guide for AZAR Dry – Stack Block Construction." *Azar Group of Companies*. Hamilton, Ontario.

Kintingu, S. H. (2009). "Design of Interlocking Bricks for Enhanced Wall Construction Flexibility, Alignment Accuracy and Load Bearing." *Ph.D. Dissertation*. The University of Warwick, England.

Kooharian A. (1952). "Limit Analysis of Voussoir (Segmental) and Concrete Arches." *J. Amer. Conc. Inst*, 24(4), 317-328.

Langer, P. (1992). Trockenmauerwerk [In German]. In. Bautechnik 69, Heft 6, Ernst & Sohn, Berlin.

Laursen, T. (2003). *Computational Contact and Impact Mechanics*, Springer, NY.

Lin, K., Totoev, Y., Liu, H., and Wei, C. (2015). "Experimental Characteristics of Dry-Stack Masonry under Compression and Shear Loading." *Materials*, 8(12), 8731-8744.

Liu, H., Liu, P., Lin, K. and Zhau, S. (2016). "Cyclic Behavior of Mortarless Brick Joints with Different Interlocking Shapes." *Materials*, 9(166), 1-12.

Lohr, J. (1992). "Evaluation of Formwall – A Post-Tensioned Dry-Stacked Masonry System." *M.S. thesis*. The Pennsylvania State University, PA.

Lourenco, P.B., and Ramos, L.F. (1994). “Characterization of Cyclic Behavior of Dry Masonry Joints.” *J. Struct. Eng.*, 130(1), 779-786.

Lourenço, P. B. (1996). *Computational Strategies for Masonry Structures. Ph.D. Dissertation*. Universidade do Porto, Portugal.

Lourenço, P. B. and Rots J. G. (1997). “A Multi-surface Interface Model for the Analysis of Masonry Structures.” *ASCE J. Engrg. Mech.*, 123(7), 660-668.

Lourenço, P. B., Oliveira, D. V., Roca, P., and Orduña, A. (2005). “Dry Joint Stone Masonry Walls Subjected to In-Plane Combined Loading.” *Journal of Structural Engineering*, 131(11), 1665-1673.

Lü, W., Wang, M., and Liu, X. (2011). "Numerical Analysis of Masonry under Compression via Micro-Model." *Advance Materials Research*, 243(1), 1360-1365.

Martínez, M., Atamturktur, S., Ross, B., and Thompson, J. (2017). “Assessing the Compressive Behavior of Dry-Stacked Concrete Masonry with Experimentally Informed Numerical Models.” *ASCE Journal of Structural Engineering*, DOI: 10.1061/(ASCE)ST.1943-541X.0002056

Martínez, M. and Atamturktur, S. (2017). “Experimental and Numerical Evaluation of Reinforced Dry-Stacked Concrete Masonry Walls.” *Elservier's Building Engineering,* (In Press)

Marzahn, G. (1997). “Dry-Stacked Masonry in Comparison with Mortar Jointed Masonry.” *LACER*, 2(1), 353-365.

Marzahn, G. (1999). "Investigation on the Initial Settlement of Dry-Stacked Masonry under Compression." *Liepzig Annual Civil Engineering Report* 3, 353-365.

Marzahn, G. (2000). “A Study on the Creep Behavior of Dry-Stacked Masonry Walls and Individual Masonry Units.” *LACER*, 5(1), 261-278.

Marzahn, G. and König, G. (2002). “Experimental Investigation of Long-Term Behavior of Dry-Stack Masonry.” *TMS Journal December*, 9-21.

Murray, E. (2007). “Dry-Stacked Surface Bonded Masonry: Structural Testing and Evaluation.” *M.S. Thesis*, Brigham Young University, UT.

Najm AMS. (2001). “Structural Behaviour of Load Bearing Interlocking Hollow Block Masonry.” *M.S. Thesis*, Universiti Putra Malaysia.

Ngowi, J. V. (2005). “Stability of Dry-Stack Masonry.” *Ph.D. Dissertation*. University of the Witwatersrand, South Africa.

Nguyen, T. M. H., Blond, E., Gasser, A., and Prietl, T. (2009). “Mechanical Homogenization of Masonry Wall without Mortar.” *European Journal of Mechanics A/Solids*, 28(3), 535-544.

Oh, K.H., Harris, H.G., and Hamid, A.A. (1993). “New Interlocking and Mortarless Block Masonry Units for Earthquake Resistant Structures.” *In Proceedings of the 6th North American Masonry Conference*, Philadelphia, PA. 821-836.

Oh, K. (1994). "Development and Investigation of Failure Mechanism of Interlocking Mortarless Block Masonry System." *Ph.D. Dissertation*. Drexel University, PA.

Okazaki, K., Pribadi, K., Kusumastuti, D., and Saito, T. (2012). “Comparison of Current Construction Practices of Non-Engineered Buildings in Developing Countries.” *In 15th World Conference on Earthquake Engineering*, Lisbon.

Oliveira, D. V. (2000) “Mechanical Characterization of Stone and Brick Masonry.” *Report 00-Dec/E-4*, Universidade do Minho, Portugal.

Ota, H. (2011). “Experimental Study of Mortarless Post-Tensioned Masonry Walls and Development of Design Guidelines.” *M.S. Thesis*. The Pennsylvania State University, PA.

Palios, X., Fardis, M. N., Strepelias, E., and Bousias, S. N. (2017). “Unbonded Brickwork for the Protection of Infills from Seismic Damage.” *Engineering Structures*, 131, 614-624.

Pave, R. (2007). "Strength Evaluation of Dry-Stack Masonry." *M.S. Thesis*, University of the Witwatersrand, Johannesburg, South Africa.

Pave, R. F., and Uzoegbo, H. (2010). “Structural Behavior of Dry Stack Masonry Construction.” *Proc., SB10 Portugal: Sustainable Building Affordable to All: Low Cost Sustainable Solutions*, Algarve, Portugal.

Prietl, T., Zach, O., and Studnicka, H. (2006). “The Evaluation of Refractory Linings Thermomechanical Properties.” *Erzmetall-World of Metallurgy,* 59(1), 127-132.

Pei, L., Hyun, S., Molinari, J. F., and Robbins, M. O. (2005). “Finite Element Modeling of Elasto-Plastic Contact between Rough Surfaces.” *Journal of the Mechanics and Physics of Solids*, 53(11), 2385-2409.

Ramamurthy, K., and Nambiar, K. (2004). "Accelerated Masonry Construction: Review and Future Prospects." *Progress in Structural Engineering and Materials*, 6(1), 1-9.

Rekik, A., Allaoui, S., Gasser, A. Blond, E., and Andreev, K. (2014). “Experiments and Nonlinear Homogenization Sustaining Mean-Field Theories for Refractory Mortarless Masonry: The Classical Secant Procedure and its Improved Variants.” *European Journal of Mechanics*, 49(1), 67-81.

Rekik, A., Nguyen, T. T. N., and Gasser, A. (2015). “Coupling between Homogenization Techniques and Brittle Mechanics for Modelling the Behavior of Micro-Cracked Refractory Linings.” *In 14th Biennial Worldwide Congress UNITECR*.

Roca, P., Oliveira, D., Lourenco, P., & Carol, I. (2001). “Mechanical Response of Dry Joint Masonry.” *In 2nd International Congress on Studies in Ancient Structures*. 571-579.

Safiee, N., Jaafar, M., and Noorzaie, J., and Kadir, M. (2009). "Finite Element Analysis of Mortarless Wall Panel." *Report and Opinion*, 1(2), 1-16.

Safiee, N., Jaafar, M., and Noorzaie, J. (2011a). “Behavior of Mortarless Wall Subjected to In-plane Combine Loading.” *Advanced Materials Research*, 264(1), 1746-1751.

Safiee, N., Jaafar, M., Jaafar, M., Al-Wathaf, A. H., Noorzaei, and Abdulkadir, M. (2011b). “Structural Behavior of Mortarless Interlocking Load Bearing Hollow Block Wall Panel under Out-of-Plane Loading.” *Advances in Structural Engineering*. 14(6), 1185-1195.

Sasaki, T., Hagiwara, I., Sasaki, K., Yoshinaka, R., Ohnishi, Y., Nishiyama, S., and Koyama, T. (2011). “Stability Analyses for Ancient Masonry Structures using Discontinuous Deformation Analysis and Numerical Manifold Method.” *International Journal of Computational Methods*, 8(02), 247-275.

Schubert, P. (1995). Mauerwerk mit Mittelbettmortel [In German]. Mauerwerk-Kalender Ernst & Sohn, Berlin.

Senthivel, R., Lourenco, P. G., and Vasconcelos, G. (2006). "Analytical Modeling of Dry Stone Masonry Wall under Monotonic and Reversed Cyclic Loading." *Structural Analysis of Historical Constructions*, 1005-1012.

Senthivel, R., Lourenço, P. B., and Vasconcelos, G. (2006). "Numerical Modelling of Deformation Behaviour of Dry-Stack Stone Masonry." Department of Civil Engineering, University of Minho.

Silva, A., Soares, E., Oliveira, D., Miranda, T., Cristelo, N., and Oliveira, J. (2015). "CEBs Stabilised with Geoploymeric Binders: Mechanical Performance of Dry-Stack Masonry." *In WASCON 2015, 9th International Conference on the Environmental and Technical Implications of Construction with Alternative Materials*, 1-6.

Sokairge, H., Rashad, A., and Elshafie, H. (2017). "Behavior of Post-Tensioned Dry-Stack Interlocking Masonry Walls under Out-of-Plane Loading." *Construction and Building Materials*, 133(1), 348-357.

Surm, T., Ramos, L. F., and Lourenço, P. B. (2015). "Characterization of Dry-Stack Interlocking Compressed Earth Blocks." *Materials and Structures*, 48(9), 3059-3074.

Tang, Z., Ali, M., and Chouw. N. (2014). "Residual Compressive and Shear Strengths of Novel Coconut-Fibre-Reinforced-Concrete Interlocking Blocks." *Construction and Building Materials*, 66(1), 533-540.

Thanoon, A., Jaafar, M.S., Abdul Kadir, M.R., Abang, A.A., Trikha, D.N. and Amad, S.N. (2004). “Development of an Innovative Interlocking Load Bearing Hollow Block System in Malaysia.” *Construction and Building Materials*, 18(1), 445–454.

Thanoon, A., Jaafar, M., Noorzaei, J., Razali, M., Kadir, A., and Fares, S. (2007). “Structural Behavior of Mortar-Less Interlocking Masonry System under Eccentric Compressive Loads." *Advances in Engineering*, 10(1), 11-24.

Thanoon, A., Al-Wathaf, A. H., Noorzaei, J., Jaafar, M., and Abdulkadir, M. (2008a). “Nonlinear Finite Element Analysis of Grouted and Ungrouted Hollow Interlocking Mortarless Block Masonry System.” *Engineering Structures*, 30(1), 1560-1572.

Thanoon, W.A.M., Alwathaf, A.H., Noorzaei, J., Jaafar M.S. and Abdulkadir, M.R. (2008b). “Finite Element Analysis of Interlocking Mortarless Hollow Block Masonry Prism.” *Computer and Structures*, 86(6), 520-528.

Tobriner, S. (1984). “A History of Reinforced Masonry Construction Designed to Resist Earthquakes: 1755-1907.” *Earthquake Spectra*, 1(1), 125-149.

Totoev, Y. (2015). “Design Procedure for Semi Interlocking Masonry.” *Journal of Civil Engineering and Architecture*, 9(1), 517-525.

Uzoegbo, H. C. (2003). “In-Plane and Out-Plane Behaviour of Dry-Stack Block Walling Systems.” *In Proc., The Ninth North American Masonry Conference,* Clemson, South Carolina.

Uzoegbo, H. C., and Ngowi, J. V. (2003). “Structural Behaviour of Dry-Stack Interlocking Block Walling Systems Subject to In-Plane Loading.” *Concrete Beton*, 1(103), 9-13

Uzoegbo, H. C. and Pave, R. F. (2005) “Compressive Strength Evaluation of Compressed-Soil Cement Interlocking Blocks.” *4th Congresso Luso-Moçambicano de Engenharia*, Maputo, Mozambique.

Uzoegbo, H. C., Senthivel, R., and Ngowi, J. V. (2007). “Load Capacity of Dry-Stack Masonry Walls.” *TMS Journal,* 41-52.

Vaculik, J., Griffith, M. C., and Magenes, G. (2014). “Dry Stone Masonry Walls in Bending - Part II: Analysis.” *International Journal of Architectural Heritage*, 8(1), 29-48.

VanderWerf, P. (1999). “Mortarless block systems.” *Masonry Construction*, *12*(2), 20-24.

Vasconcelos, G. (2005). “Experimental Investigations on the Mechanics of Stone Masonry.” *Ph.D. Dissertation*. Universidade do Minho, Portugal.

Vasconcelos, G., and Lourenço, P. (2009). "Experimental Characterization of Stone Masonry in Shear and Compression." *Construction and Building Materials*, 23(11), 3337-3345.

Vélez, L. F. and Magenes, G. (2009). “Static Tests on Dry Stone Masonry and Evaluation of Static Collapse Multipliers.” *Research Report ROSE 2009/02*. Pavia, Italy.

Velez, L., Magenes, G., and Griffith, M. (2014). “Dry Stone Masonry Walls in Bending – Part I: Static Tests.” *International Journal of Architectural Heritage*, 8(1), 1-28.

Venkatarama Reddy, B. V. (2009). "Sustainable Materials for Low Carbon Buildings." *International Journal of Low-Carbon Technologies*, 4(3), 175-181.

Waleed, A.T, Jaafar, M.S., Abdul Kadir, M.R., Abang, A.A.A., Trikha, D.N. and Amad, M.S. (2004). "Development of an Innovative Interlocking Load Bearing Hollow Block System in Malaysia", *Construction and Building Materials*, 18(1), 445-454.

Wheeler, G. (2005). "Interlocking Compressed Earth Blocks Volume II." *Manual of Construction. Center for Vocational Building Technology*, Thailand, 110-115.

Whelan M.L. (1985). "Hollow Concrete Masonry Unit Shape Modification to Improve Productivity of Placement: Results of the Preliminary Research Effort." *Proceedings of the 3rd North American Masonry Conference*, Arlington, TX.

Yamaguchi, K., Matsufuji, Y., and Koyama, T. (2007). "A New Structural System: Friction-Resistant Dry-Masonry." *Building Research and Information*, 35(6), 616-628.

Zahra, T., Yin, Z., and Dhanasekar, M. (2016). "Experimental Investigation of Dry Joint Surface and Closure Characteristics of Interlocking Blocks Under Compression." *Brick and Block Masonry – Trends, Innovations and Challenges.* Taylor & Francis Group, London.

Zhang, S., Wang, W., and Zhao, Z. (2014). "The Effect of Surface Roughness Characteristics on the Elastic–Plastic Contact Performance." *Tribology International*, 79(1), 59-73.

Zhuge, Y., Corderoy, J., and Thambiratnam, D. (1996). "Behavior of Unreinforced Brick Masonry under Lateral (Cyclic) Loading." *TMS Journal*, 14 (2), 55-62, 1996.

Zuccarello, F. A., Milani, G., Olivito, R. S., and Tralli, A. (2009). "A Numerical and Experimental Analysis of Unbonded Brickwork Panels Laterally Loaded." *Construction and Building Materials*, 23(5), 2093-2106.

CHAPTER THREE

ASSESSING THE COMPRESSIVE BEHAVIOR OF MORTARLESS CONCRETE MASONRY WITH EXPERIMENTALLY INFORMED NUMERICAL MODELS

3.1 Introduction

Laying concrete masonry units (CMU) dry without mortar, known as dry-stack construction, leads to significant reductions in construction time, the need for skilled labor, and construction cost (Oh 1994; Beall 2000; Ramamurthy and Nambiar 2004; Murray 2007). Such mortarless masonry systems have been shown to provide in-plane (Lourenço et al. 2005) and out-of-plane capacities (Ferozkhan 2005) provided by surface bonding and interlocking, capacities similar to conventional construction; however, they exhibit failure modes that are fundamentally different from those of bonded masonry. In conventional bonded masonry construction, the effects of irregular surface topography at the bed joints are mitigated by mortar. The absence of mortar in dry-stack construction, however, creates complex stress states with large gradients at the interface between the units. Local cracking and crushing resulting from these high stresses alter ultimate load capacity of the units (Jaafar et al. 2006) in a way that is not yet fully understood (Marzahn 1999; Anand and Ramamurthy 2000).

The contact behavior at the interface between the units depends on many micro-scale phenomena, including contact pressure, friction, and cohesion (Yastrebov et al. 2015). Previous studies on numerical modeling of mortarless masonry systems represented this interface with either zero-thickness contact (Baggio and Trovaluski 1993; Thanoon et

al. 2007; Safiee et al. 2009) or two-dimensional link elements (Oh 1994; Campbell 2012), significantly simplifying the representation of the surface roughness. Recent studies have demonstrated that the actual variation in the height of the units (Thamboo and Dhanasekar 2015) as well as the surface topography influence the deformation in the contact area (Peng and Bhushan 2001; Jackson and Streator 2006; Thamboo et al. 2013). Hence, modeling the surface topography is essential for investigating the effect of the bed joint surface roughness on the stiffness characteristics, stress distribution and the global behavior of the mortarless masonry system (Sellgren et al. 2003; Yastrebov et al. 2012). For instance, CMUs to be used in dry-stacked construction can have smoothed (ground) or rough (unground) bed surfaces (See Fig. 3-1 for microscale views of the bed surfaces of these two types of units), where the smooth bed surfaces are obtained using diamond-plated pads to grind the rough surfaces (following the same process used to create smooth face blocks), and the units with rough bed surfaces are those that are commonly provided by the manufacturers. The effect of such variation in bed surface roughness on the load carrying performance of dry-stacked systems is currently unknown, and studying this effect requires an explicit consideration of surface topography at the bed joint, which is precisely what is accomplished in this study.

In this paper, the authors present a modeling strategy for dry-stacked masonry systems that take into account not only the highly nonlinear behavior of the masonry material and the dry contact between the units but also the surface topography at the bed joint. A particular contribution of this paper is its focus on standard (8”×8”×16”) blocks (i.e., CMUs most commonly used in the United States), as past studies on this topic have

primarily focused on proprietary units, often with interlocking components (Beall 2000; Anand and Ramamurthy 2005; Murray 2007; Pave 2007). The numerical models developed in this study for standard CMUs are rigorously compared against experimental measurements to validate their ability to yield accurate predictions regarding the influence of surface roughness on the global behavior of the prisms. The validated numerical models are then used to explore the relationship between the properties of standard CMUs and dry-stacked assemblies to better understand the behavior of this unconventional masonry construction technique.

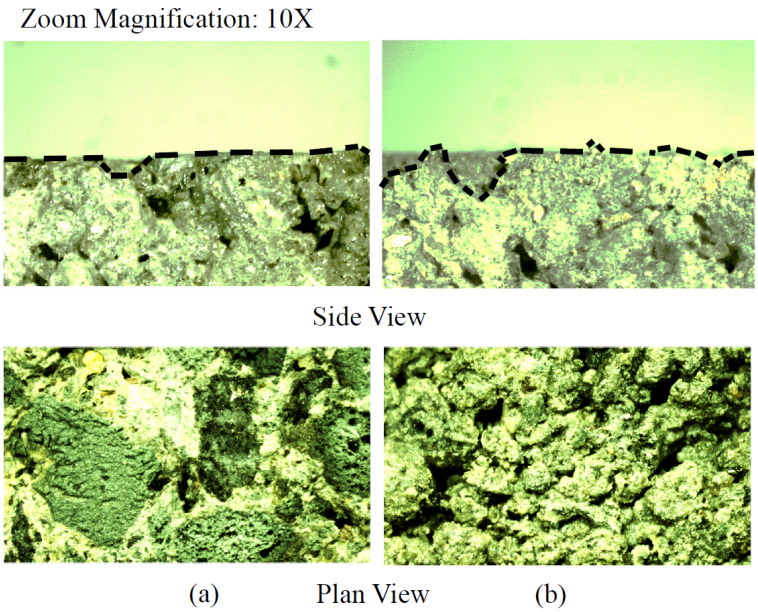

Fig. 3-1. The CMU bed (a) ground surface and (b) unground surface.

3.2 Numerical Models for Dry-Stack Masonry Prisms

Finite Element (FE) models for two-unit hollow and grouted prisms with two variations, representing smoothed (ground) or rough (unground) bed surfaces, are built in ANSYS v.15 (Fig. 3-2). These four models differ only in the contact surface between the

units and whether the unit is grouted or not. The models are built using the nominal dimensions of a two-core CMU, stretcher unit with an 8” width and height, a 16” length, a 1.25” thickness in face shells and a 1” thickness in end shells and web. Fillets at the edges in the cells and the tapering of the web are neglected to simplify the model geometry. Grouted prisms are built with the assumption of a perfect bond at the interface between the units and the grout as well as the assumption of continuity of grout along the prism height. The FE models are developed to include the top and bottom steel plates that are part of the universal testing machine. Boundary conditions at the base of the lower steel plate are fixed, restraining translation and rotation in all directions, while the top steel plate is restrained to prevent lateral movements (Fig. 3-3).

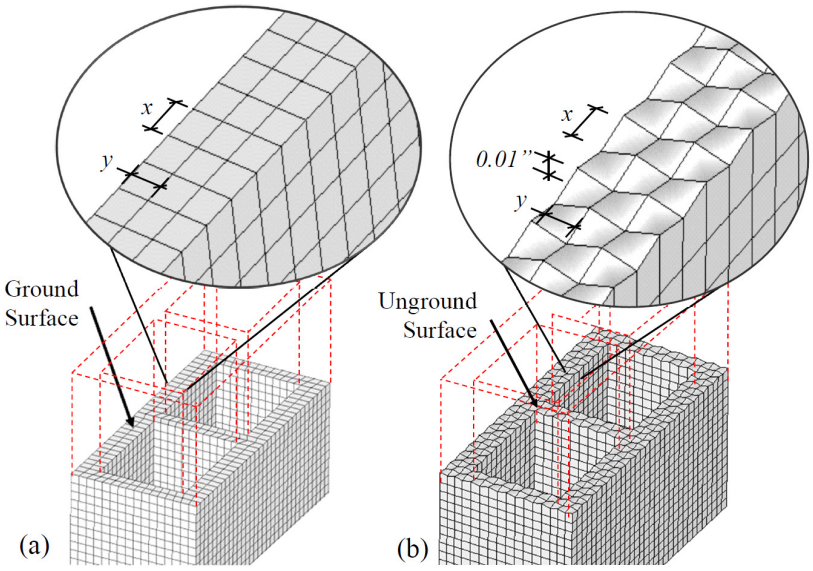

Fig. 3-2. FE models: (a) ground surface and (b) unground surface; the vertical scale has been increased for enhanced visualization.

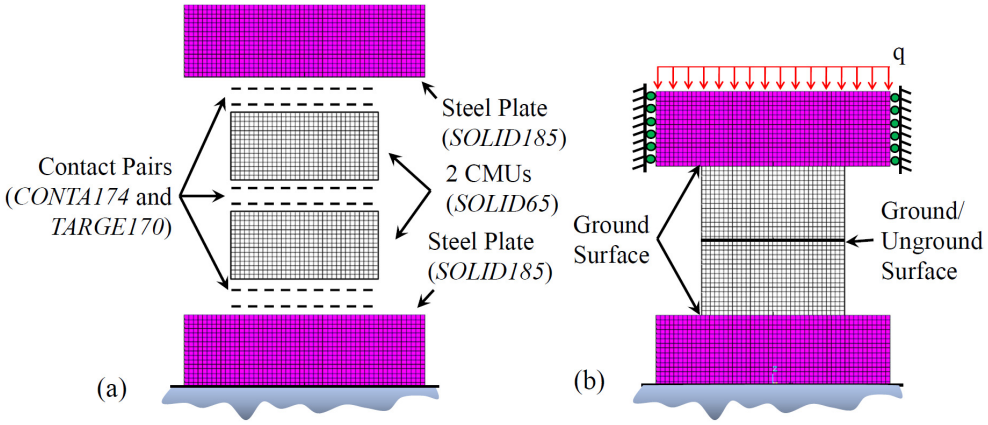

Fig. 3-3. FE model of the two-unit dry-stacked prisms: (a) element types, (b) configuration during testing.

3.2.1 Representation of Dry-Stack Contact Stiffness

For the prism with unground units, a rough surface is assumed at the contact between units. Rough surfaces are composed of a large number of asperities (or peaks and valleys). To model the roughness, the prisms include gaps between the two units but with contact occuring at the peaks (high points). Three parameters describe the asperities: length (x), width (y) and peak height or depth (Fig. 3-2). The asperities are created by moving a predefined set of nodes in the mesh hence by changing the aspect ratios of the individual finite elements. The mesh size in the model is set according to the x and y asperities. The asperity height is assumed to be uniform at the mean height of 0.01" and is determined using the sand patch test (see ASTM E965). The sand patch test measures the texture depth of a rough surface and involves spreading sand to fill gaps in the surface. The texture depth is equal to the volume of the sand required to fill the gaps divided by the area over which the sand is applied (Atamturktur et al. 2016). For the prism with ground units, the bed

surface is kept smooth (Fig. 3-2 (a)). Both variations of FE models include 31,340 nodes and 27,792 elements.

The interfaces between CMU and steel plate, as well as CMU and CMU are modeled with 8-node contact elements *CONTA174* and *TARGE170*. In the numerical model, the contact interface is modeled using the contact (*CONTA174*) and target (*TARGE170*) surfaces available in ANSYS. The contact and target surfaces constitute a contact pair that can identify when contact occurs and prevent (or limit) penetration between the solids (Recall Fig. 3-3). The contact pair supplies a scheme for ensuring a proper transfer of forces between two solids according to normal and tangential contact stiffnesses. In this study, the normal contact stiffness, which controls the penetration between the two bodies, is assumed to be identical to the stiffness of the body beneath the contact element. The tangential contact stiffness, used to represent the sliding behavior, is idealized via the coefficient of friction (Prabhu et al. 2014).

Sliding behavior of the contact pair is governed by the Mohr-Coulomb criterion given as $\tau_{lim} = \mu\sigma + c_c$, where τ_{lim} represents the limit for shear stress at which sliding begins, σ represents the normal contact pressure, μ represents the coefficient of friction, and cc represents contact cohesion. When the shear stress exceeds τ_{lim}, the elements *CONTA174* and *TARGE170* allow sliding. In contact surfaces, cohesion can provide sliding resistance; however, because contact cohesion is negligible at dry joints ($c_c = 0$), the shear stress is carried entirely by the friction (Vasconcelos and Lourenço 2009). In both variations of the FE models, the coefficient of friction is set to be 0.3 for the CMU-CMU contact surfaces, and 0.15 between CMU-steel plates (Gorst et al. 2003). In the prisms with

unground units, the friction due to the roughness of the bed joint is taken into account by modeling the asperities.

The contact between the surfaces generates a nonlinearity; a change in stiffness occurs in the contact between two solid bodies as a function of the nodal displacements. The contact nonlinearity arises when one body tries to penetrate another solid body. The penetration must be within tolerances to have a converged solution. Although many formulations exist for solving contact problems (Laursen 2003), the Augmented Lagrange method (Bertsekas 1996) is preferred for modeling the prism with ground units. This is because the method is capable of controlling penetration at the contact surface by introducing an opposing force at the nodes at which contact is detected. For the FE model for the prism with unground units, the Multi-Point Constraints method (Ainsworth 2001) is preferred as this method satisfies the impenetrability between the unground surfaces. Unlike the Augmented Lagrange method, Multi-point Constraints uses rigid constraint equations between the solid elements on the contact and target elements, eliminating degrees of freedom at the nodes on the contact and target elements (Cunningham 2014).

3.2.2 Element Type Selection and Material Model

ANSYS has the capability to represent the behavior of concrete masonry and grout with the specialized *SOLID65* element, a predefined 8-noded solid isoparametric hexahedron element that can simulate typical masonry failure, which is characterized by cracking in tension and crushing in compression (Truong-Hong and Laefer 2008; Lü et al. 2011). *SOLID65* can represent cracking and crushing as a smeared crack, where the crack/crush reduces the stiffness of the element while keeping the mesh topology as a

continuum (Rots and Blaauwendraad 1989). The material models used in this study are (i) the Drucker-Prager model, which introduces a plastic behavior after the elastic limit is exceeded and before the ultimate capacity of the material is reached either in compression or in tension; and (ii) the Willam-Warnke model, which defines the material behavior in each element after cracking and crushing conditions are met. Steel plates of the universal testing machine are represented with *SOLID185* elements, which have the capability to represent large deflection, large strain, and ductile materials (Salas and Sánchez 2012).

To account for the plasticity, the Drucker-Prager model (Drucker et al. 1952), yield criterion widely implemented for masonry structures is adopted (Sayed-Ahmed and Shrive 1996; Michel 2015; Stefanou et al. 2015). This criterion defines a surface created in the principal stress domain that takes into account the limited plastic-flow ability before crushing. This yield criterion introduces an elastic perfectly plastic model that is defined by two parameters: cohesion c and the internal friction angle ϕ. Values $\phi = 36.65^{\circ} - 1.1^{\circ}(f'_{unit}/1000)$ proposed by Dahl (1992) and Mahboubi and Ajorloo (2005) and $c = f'_{unit}/4$ proposed by Chen (1982) are adopted here, and the values $\phi = 0.01 f'_{grout}$, and $c = 0.129 f'_{grout} + 268.32$, proposed by Köksal et al. (2005), are used to represent the grout.

SOLID65 element accounts for cracking through a smeared crack analogy and crushing through a plasticity algorithm in three orthogonal directions according to the Willam–Warnke failure criterion (Willam and Warnke 1974; Fanning 2001). Failure occurs when multi-axial stresses in the element surpass the failure surface defined by the criterion. In particular, cracking and/or crushing occurs in the element at any integration point once one of the principal stresses lies outside the failure surface. After cracking

occurs, the modulus of elasticity of the element at the integration point is set to zero in the direction parallel to the principal stress; however, a stiffness multiplier (0.6 as a default value) is applied at the integration point in the direction of the principal stress to ensure the convergence of the calculations. Similarly, after crushing occurs, the modulus of elasticity of the element at the integration point is set to zero in all directions of principal stresses; however, a stiffness multiplier (1.0E-06 as a default value) is applied at the integration point in the direction of the principal stress to avoid numerical instabilities (Dahmani et al. 2010).

SOLID65 element allows for the transfer of tangential loads across cracks, simulating the aggregate interlocking effect through the shear transfer coefficient for open cracks, and the interlock between cracked faces through the shear transfer coefficient for closed cracks (Parvanova et al. 2005; Contamine et al. 2011). This shear transfer coefficient ranges from 0.0 to 1.0, where 0.0 represents a perfectly smooth crack (complete loss of shear transfer capability), and 1.0 represents a perfectly rough crack (no loss of shear transfer capability). The coefficients are often set for open and closed cracks independently. This study adopts shear transfer coefficients used in previous studies of 0.2 for open cracks and 0.6 for closed cracks (Kachlakev et al. 2001; Prabhu et al. 2014). The measured averaged properties of individual concrete masonry units (e.g., compressive strength and modulus of elasticity) are listed in Table 3-1 along with other properties recommended in the literature needed to define the material model in the numerical model.

Table 3-1. Material properties of the units and grout specimen entered into the FE model.

Material Properties	Ground Units			Unground Units			Grout
Measured in the laboratory	G1	G2	G3	U1	U2	U3	GG
Modulus of elasticity (ksi)	792	1,075	1,817	600	1,180	1,400	2,200
Compressive strength, f'_{unit} (psi)	2,875	3,140	3,263	2,188	2,511	3,675	4,400
Obtained from literature (see *Element Type Selection and Material Model* Section for details)							
Poisson's ratio	0.2	0.2	0.2	0.2	0.2	0.2	0.2
Cohesion, c (psi)	719	785	816	547	628	919	836
Friction angle, ϕ (°)	33.5	33.2	33.1	34.2	33.9	32.6	44
Tensile strength, f_t (psi)	288	314	326	219	251	368	440
Shear transfer coef. for open cracks, β_t	0.2	0.2	0.2	0.2	0.2	0.2	0.2
Shear transfer coef. for closed cracks, β_c	0.6	0.6	0.6	0.6	0.6	0.6	0.6

3.2.3 Laboratory Experiments to Determine Concrete Masonry Unit Properties

To determine the unit properties (i.e., compressive strength and modulus of elasticity) needed for the development of the FE models, individual units are tested according to ASTM C140 (ASTM 2014). Table 3-2 shows the results obtained from 18 units categorized according to different compressive unit strengths per manufacturer specifications (G1 to G3 and U1 to U3). This table also shows the range of the measured compressive strength (f'_{unit}) for all three replicates. Grout used to fill the cores (GG) is also tested in accordance with ASTM C476 (ASTM 2016a) and ASTM C1019 (2016b). In the absence of tensile test data, the tensile strength (f'_t) is approximated to be about 10% of the compressive strength (Klingner 2010). The modulus of elasticity is derived from these measurements according to ASTM E111 (ASTM 2010) as the chord modulus of the

predominantly linear region of the stress-strain curve. In our application, this coincides with the region between 50% and 80% of the ultimate strength.

Table 3-2. Unit properties measured by testing.

Unit Type	Cate-gory	# of Tests	Specified f'_{unit}	Measured Strength			Measured Elasticity		
				Min.	Mean	Max.	Min.	Mean	Max.
Ground Units	G1	3	2,000	2,689	2,875	2,970	668	792	926
	G2	3	2,500	2,962	3,140	3,234	953	1,075	1,228
	G3	3	3,000	3,107	3,263	3,432	1,710	1,817	1,945
Unground Units	U1	3	2,000	1,893	2,188	2,397	560	600	643
	U2	3	2,500	2,413	2,511	2,741	1,050	1,180	1,269
	U3	3	3,500	3,247	3,675	3,974	1,270	1,400	1,501
Grout	GG	2	NA	4,320	4,400	4,480	2,078	2,200	2,321

Note: Units are in psi. NA=Not applicable

3.2.4 Numerical Solution Set-up and Mesh Refinement Study

The dry-stack prism behavior under compression is simulated considering both self-weight and the static vertical compressive pressure (*q,* in Fig. 3-3*).* Pressure applied on the upper surface of the steel plate is increased until failure is reached in the prism. Obtaining converged numerical solutions is challenging for this problem due to the combined effects of material nonlinearity (concrete cracking and crushing) and nonlinear boundary conditions at the contact surfaces. The FE model is solved using the iterative Newton-Raphson algorithm (Madenci and Guven 2015), tracing the equilibrium path during the load-deformation response. The Newton-Raphson scheme updates the tangent matrix and the restoring force vectors analogous to the element internal forces (Bathe 1996; Prabhu et al. 2014; Subramani et al. 2014).

The localized nonlinear behavior that involves cracking and crushing of the material makes it crucial to evaluate the adequacy of the mesh size to yield accurate solutions. The authors used the Grid Converge Index (GCI) to quantify the order of convergence and the bounds for discretization error (Roache 1994; Schwer 2008; Atamturktur 2009; Kwasniewski 2013). GCI is based on a generalized Richardson Extrapolation using the responses obtained with three mesh sizes (Δ_F=*0.5* in., Δ_M=*1* in., and Δ_C=*2* in.). The GCI value is calculated as $GCI=(F_S\varepsilon)/(R^p-1)\times 100\%$, where F_S is a factor of safety with a suggested value of 1.25 when three mesh sizes are evaluated; ε is the difference between subsequent solutions for a group of meshes (i.e., fine (Δ_F) to medium (Δ_M) and medium (Δ_M) to coarse (Δ_C)) at each load stage; *R* denotes the refinement ratio, which is the ratio of mesh sizes; and *p* denotes the rate of convergence. The rate of convergence can be estimated through Eq. 1.:

$$\boldsymbol{p} = \frac{\boldsymbol{log}\left(\frac{\boldsymbol{y(\Delta_M)-y(\Delta_C)}}{\boldsymbol{y(\Delta_F)-y(\Delta_M)}}\right)}{\boldsymbol{log\, R}} \qquad \text{Eq. 3-1.}$$

where $y(\Delta_x)$ is the discrete solution for displacements of the different mesh sizes. When the rate of convergence is estimated using the group from fine (Δ_F) to medium (Δ_M) or from medium (Δ_M) to coarse (Δ_C), a rate of convergence value of approximately $p=1$ is obtained, indicating first-order convergence as $\Delta_x \rightarrow 0$. This matches the first-order of accuracy of the 8-noded *SOLID65* element, indicating the suitability of the evaluated mesh sizes. Finally, the results of the mesh refinement study show a value of 2.13% for and 4.18% for $GCI_{M\text{-}C}$. The value obtained for $GCI_{F\text{-}M}$ results in a numerical uncertainty that is sufficiently lower than the experimental variability; therefore, the fine mesh size (i.e., 0.5 in.) is deemed appropriate.

3.3 Experimental Validation of FE Models

The response of two-stack mortarless masonry prisms under compressive loads are experimentally measured and compared against the predictions of the developed FE models. The experimental campaign involved two-unit dry-stacked, prisms built with units that had ground and unground bed surfaces. Two distinct types of model response are compared with experiments: the failure pattern, which is evaluated through a visual comparison, and the ultimate compressive strength of the prisms, which is evaluated quantitatively considering the experimental variability.

3.3.1 Hollow and Grouted Prism Tests

A total of 124 hollow prisms are built by dry-stacking two standard 8”×8”×16” units (half of which are built with ground units and the other half with unground units). The compressive strength of the prisms is determined according to ASTM C1314 (ASTM 2011) using a SATEC Systems M11-400RD universal testing machine (Fig. 3-4).

Fig. 3-4. Experimental setup for prism masonry test.

Fig. 3-5 compares two hollow representative prisms with ground and unground units. At ultimate compressive strength, the prism with unground units exhibits significantly larger deformations (strain of 0.73%) than the prism with ground units (strain of 0.53%). For grouted prisms, four specimens are available, two with ground units and two with unground units. The grout is poured in the cells, tamped with a metal rod, and finished to a smooth, level surface. The experimental test includes procedures for providing plane surfaces on the two bearing surfaces of the prisms through capping according to ASTM C1552 (ASTM 2016c).

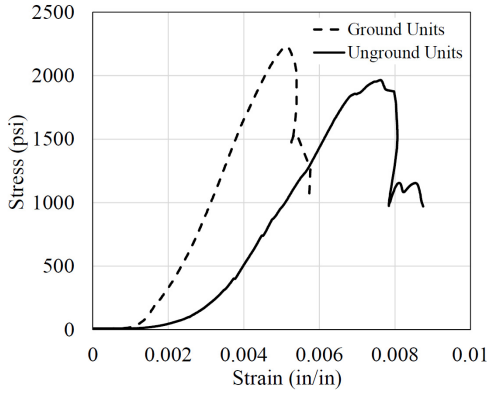

Fig. 3-5. Representative stress–strain curve for hollow prisms with ground and unground units.

3.3.2 Test-Analysis Comparison

3.3.2.1 Failure Patterns

Failure patters are experimentally observed and numerically predicted failure patterns are compared for hollow prisms with ground units for the G1 category as shown in Fig. 3-6. Model predictions agree with experimental observations in that cracking initiates at approximately 80% of the ultimate load near the top and bottom corners of the ground units. It extends diagonally across the end shells and propagates along the height (Fig. 3-6). Fig. 3-7 depicts the stress-strain diagrams obtained from compressive tests conducted on 22 nominally identical hollow prisms with ground units (i.e., G1 category). The scatter in the stress-strain plots can be explained by the inherent variability in the dry-stacked bed joints as well as the unit-to-unit variations in material properties, which could collectively lead to different failure mechanisms for the prisms. Indeed, during the 22 replication tests, different failure patterns are observed in the experiments; the most frequently observed failure pattern is presented in Fig. 3-7.

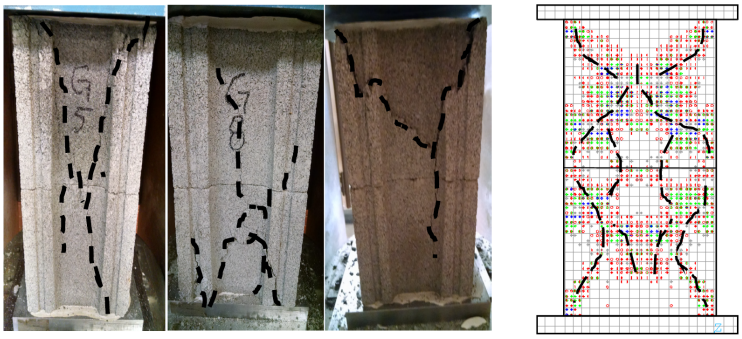

(a) (b)

Fig. 3-6. (a) Crack/crush pattern comparison in the end shell between experiments and (b) numerical model for hollow prisms with ground units.

However, in both the experimental observations and the model predictions, cracking initiates in the face shell when the load reaches approximately 90% of the ultimate load. Cracks at the corners of the units start to propagate diagonally across the face shell, forming an X shape, at which point severe crushing occurs across the contact area between units. The calculated compressive strength at failure is considered to be the load at which a considerable number of solid elements have cracked and/or crushed; beyond this load, rigid body motion governs the behavior. The post-peak response of the dry-stacked prisms is omitted due to the issues regarding numerical instability. Thus, the simulation is terminated at the ultimate load.

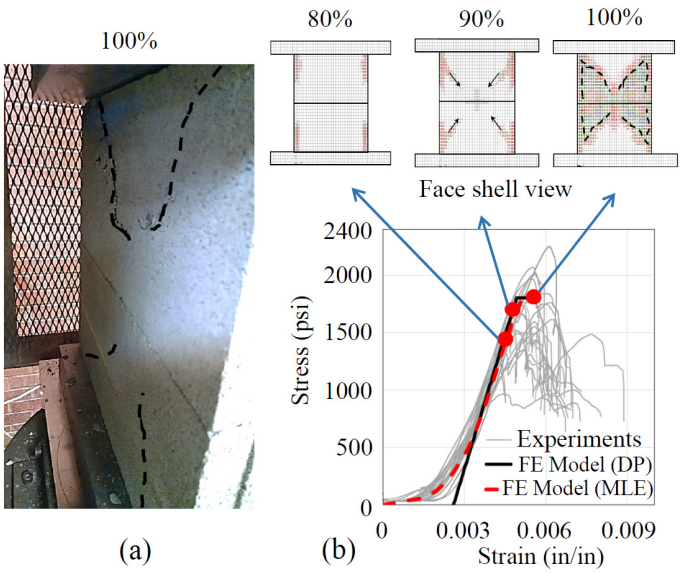

Fig. 3-7. (a) Crack/crush pattern comparison in the face shell between experiments and (b) numerical model for hollow prisms with ground units.

Also, Fig. 3-7 and Fig. 3-9 show a seating effect (Oh 1994; Kaushik et al. 2007; Andreev et al. 2012; MSJC 2013; Lin et al. 2015), especially in the experiments of prism with unground units at compressive stresses less than 300 psi (Recall Fig. 3-5). In this study, the elastic perfectly plastic Drucker-Prager (DP) material model that takes into account plastic deformations is implemented to simulate the ultimate compressive behavior of dry-stacked prisms. The numerical model using the DP material model omits the seating effect given that the basis of this material model is an elastic perfectly plastic behavior. Hence, the graph is aligned to match the experimental curves at high strains. When it is desired to represent the seating effect with the FE simulation, one could implement a multilinear elastic material (MLE) model. It is, however, important to note that the DP model is 30% more computationally efficient than the MLE, and as evidenced in the stress-

strain plots of Fig. 3-7 and Fig. 3-9, both models converge to approximately similar ultimate compressive strengths.

The same comparative study is repeated for prisms with unground units as shown in Fig. 3-8 for the U1 category. Both the experiments and the numerical model show a concentration of stresses in the dry contact surface and crushing initiates at early load stages in the contact area. The end shell exhibits vertical cracking that begins at the contact area and propagates along the height when the load reaches approximately 70% of the ultimate load. Fig. 3-9 shows a comparison of the failure pattern in the face shell observed during the experiments to that predicted by the FE model. In both the experiments and the numerical models, when the load reaches 75% of the ultimate load, cracks in the face shell at the unit interface propagate up and down from the corners at a 45-degree angle. Through the test-analysis comparison presented in from Fig. 3-6 to Fig. 3-9, the numerical model is deemed to be capable of providing a representative failure pattern of the experimental tests.

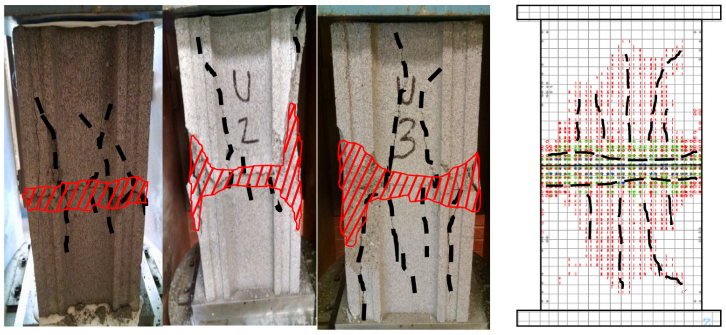

(a) (b)

Fig. 3-8. (a) Crack/crush pattern comparison in the end shell between experiments and (b) numerical model for hollow prisms with unground units.

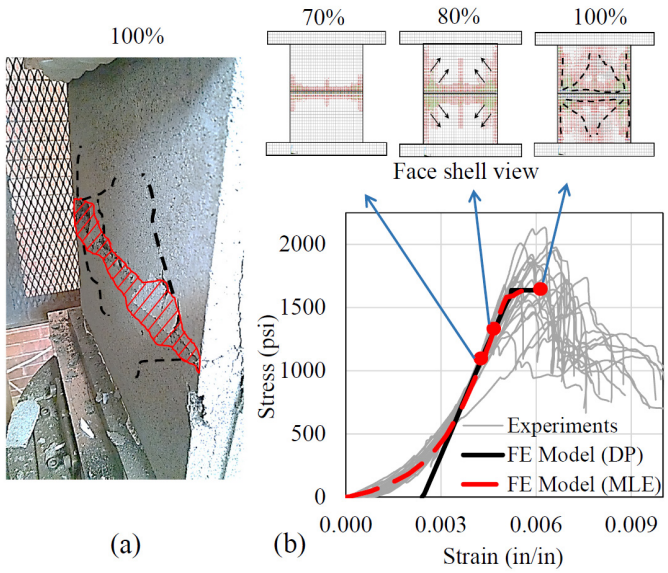

Fig. 3-9. (a) Crack/crush pattern comparison in the face shell between experiments and (b) numerical model for hollow prisms with unground units.

Fig. 3-10 shows the failure pattern in the face shell of grouted prisms with ground and unground units (i.e., the GG+G1 and GG+U1 categories). From the figure, a diminished seating effect can be seen in the experiments in grouted prisms. This observation applies to both ground and unground units. The failure pattern in prisms with both ground and unground units exhibits an X shape across the height of the prism. However, a stress concentration around the bed joint in the grouted prisms with unground units is still noticeable.

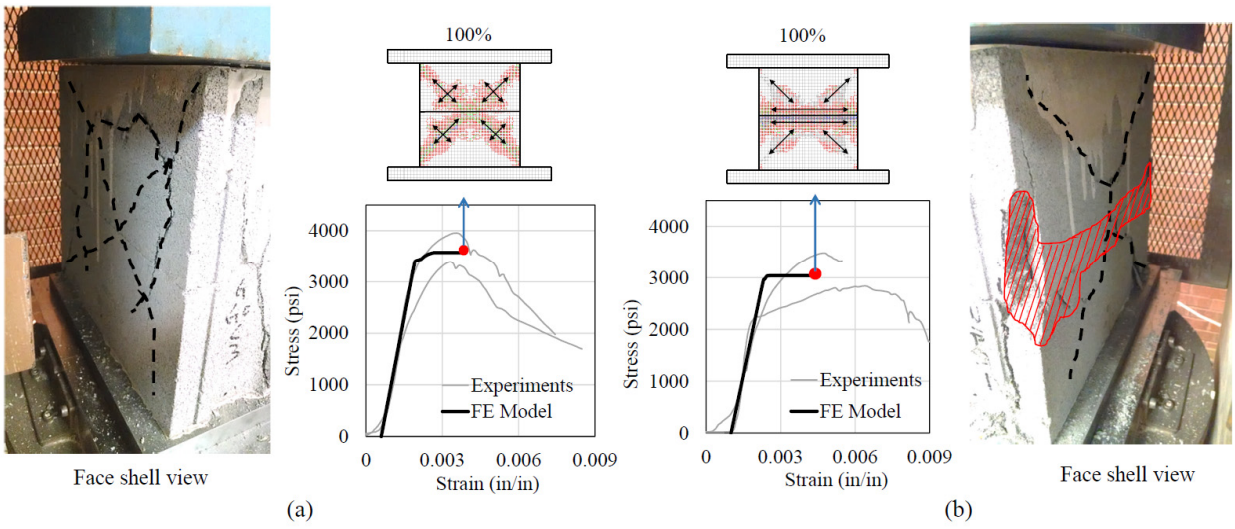

Fig. 3-10. Cracking and/or crushing pattern within the face shell of grouted prisms observed in the experiments and calculated by the numerical model prisms with (a) ground units and (b) unground units.

3.3.2.2 Ultimate Compressive Strength

The experimental measurements and the corresponding model predictions for the prisms under compressive load are compared in Table 3-3. The differences between the measured ultimate compressive strength of the prisms and their corresponding FE models are within one standard deviation as shown in Table 3-3. The compressive strength of the prisms predicted by the FE model is within the range of variability of the prism compressive strength measured during the experiments. Thus, the comparison of the experimental prism tests and the FE model predictions indicates that the developed models are an adequate representation of mortarless masonry behavior.

Table 3-3. Comparison of measured and calculated prism response.

Unit Type	Category	# of Tests	Measured Strength				Calculated Strength	Within Range?
			Min.	Mean	Max.	S.D.		
Ground	G1	22	1,643	1,776	1,909	235	1,805	Yes
	G2	19	1,990	2,224	2,458	407	2,235	Yes
	G3	20	2,444	2,688	2,932	424	2,629	Yes
Unground	U1	20	1,541	1,797	2,053	221	1,647	Yes
	U2	20	1,461	1,700	1,939	243	1,706	Yes
	U3	23	1,605	1,788	1,971	249	1,953	Yes
Grouted	GG+G1	2	3,390	3,672	3,954	282	3,574	Yes
	GG+U1	2	2,837	3,161	3,484	323	3,038	Yes

Note: Units are in psi.

3.4 Parametric Study of Prism Strength

One of the main purposes of a validated numerical model is to predict the response of the system at untested settings or configurations. Here, the FE models of the prisms are executed to predict the ultimate compressive strength of the dry-stacked prisms for varying unit strength, grout strength, surface roughness, and unit dimensions through a parametric analysis.

3.4.1 The Effect of Unit Strength

To derive a functional relationship between the unit compressive strength (f'_{unit}) and prism strength, the latter is numerically evaluated for varying values of the former. During this evaluation, the modulus of elasticity and the unit tensile strength (f'_t) are varied with respect to the compressive strength. The modulus of elasticity is defined as 900 times the compressive strength of the unit, while the tensile strength is defined to be within 10-20% of the ultimate compressive strength (Drysdale et al. 1994). The results are obtained for prisms built with ground and unground units, as illustrated in Fig. 3-11. As seen in this

figure, both prisms exhibit similar near-linear relationships between unit and prism strength; however, prisms with unground units exhibit approximately 15% less strength capacity compared to prisms with ground units.

When the ratio between unit tensile and compressive strengths increases in increments of 2% (i.e., tensile strength = 10, 12, 14,…20% of compressive strength), the ultimate capacity of the prisms increases by 7-11% for prisms with ground units and by 8-12% for prisms with unground units. The response of both hollow prisms with ground and unground units can be predicted through Eq. 3-2 and Eq. 3-3, respectively, where a valid domain for f'_{unit} is from 2,000 psi to 4,500 psi and for f'_t is from $0.1f'_{unit}$ to $0.2f'_{unit}$.

$$f'_{prism} = 492 + 0.21f'_{unit} + 2.8f'_t, \quad \text{Eq. 3-2}$$

$$f'_{prism} = 319 + 0.19f'_{unit} + 2.7f'_t, \quad \text{Eq. 3-3}$$

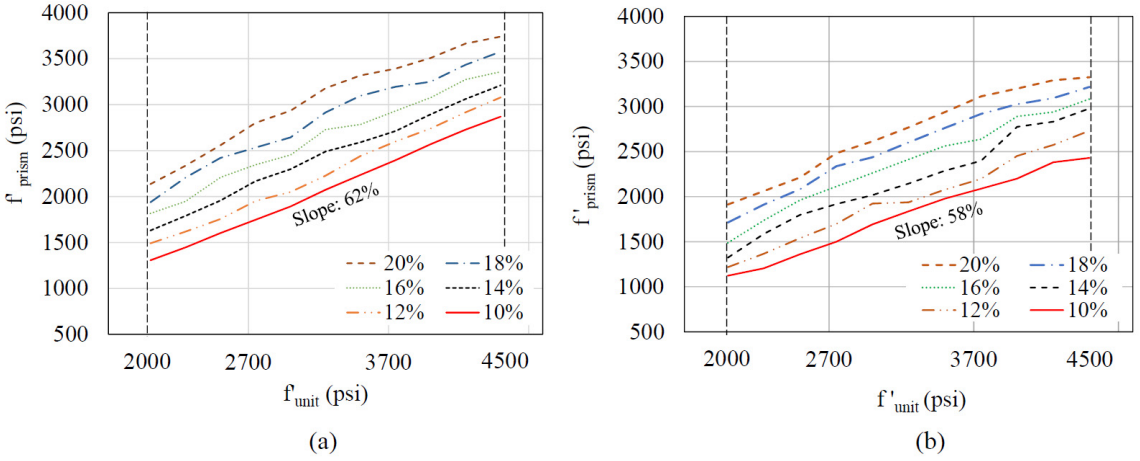

Fig. 3-11. Predictions for different tensile strengths as percentages of compressive strength for the prisms with (a) ground and (b) unground units.

3.4.2 The Effect of Surface Roughness

Another parameter of interest is the surface roughness of the units at the bed joint. This effect is evaluated through a roughness index (RI) defined as the ratio between the volume of the void and the solid portions contained in one representative section of asperities (see Fig. 3-12 (a)). Assuming a periodic distribution of asperities and uniform asperity height, this ratio can be described mathematically by Eq. 3-4 and Eq. 3-5:

$$RI = \frac{L^2h - \frac{1}{3}L^2h + a^2h}{\frac{1}{3}L^2h}, \text{ when b=0,} \quad \text{Eq. 3-4}$$

$$RI = \frac{\frac{2}{3}L^2h - bhL - b^2h}{\frac{1}{3}(L^2 + bL + b^2)h}, \text{ when a=0,} \quad \text{Eq. 3-5}$$

where L is the representative unit length in which the asperity is developed, a is the width of the valley, b is the width of the peak, and h is the height of the asperity. In this study, a mean value of 0.01 in for h is identified through laboratory experiments on commercially available CMUs. The rougher case from Fig. 3-12 (a) occurs when the widths of both the peak and the valley are equal to zero, indicating that the ratio of the enclosed void volume and the volume of a solid square pyramid (roughness index) is 2. Note that Equations 4 and 5 focuses on cases with sharp peaks and valleys, which are commonly observed asperities of CMUs. These equations would need to be expanded to consider cases where the asperities have a tooth-like form (i.e., b≠0 and a≠0).

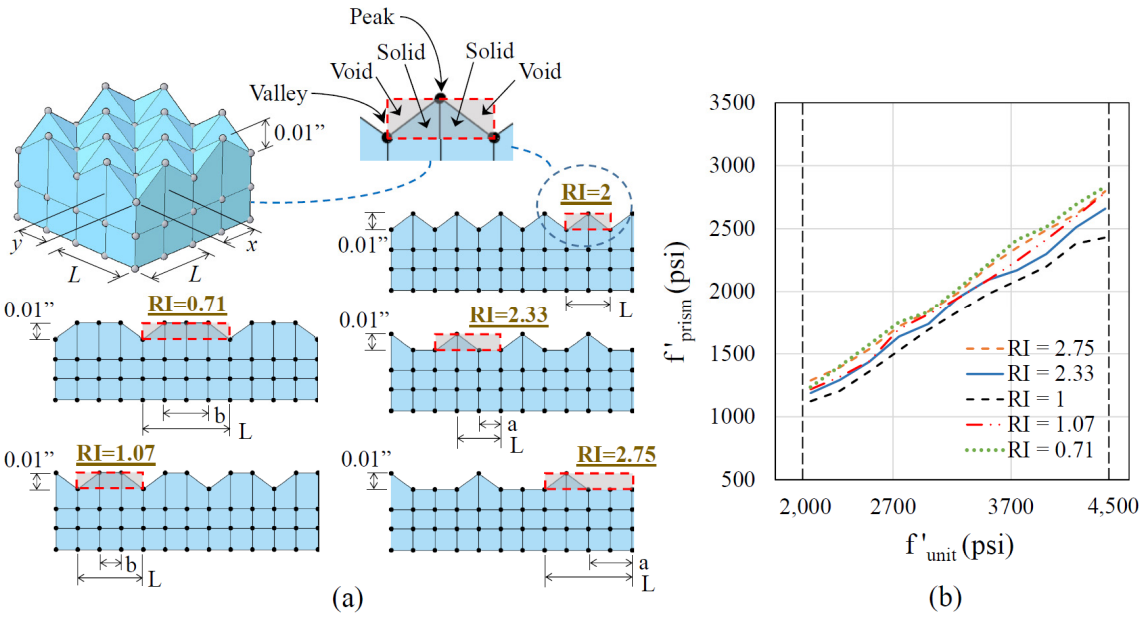

Fig. 3-12. (a) Schematic representation of surface roughness in the bed joint and (b) predictions of compressive strength of prisms with unground units at different RI.

All models discussed previously are simulated using an RI=2, meaning that surface roughness is represented as a continuous series of peaks and valleys with equal widths (the widths are defined by the mesh size x and y). Fig. 3-12 (b) shows that the relationship between unit and prism strengths is nearly linear for all five values of RI analyzed. At lower or higher values of RI, the initial gap closes at lower load levels, increasing the contact area between units. As a result, the stress distribution in the bed joint becomes more uniform in the valleys at lower load levels than the prisms with lower RI values. This helps reduce the extent of local failures around the peaks and allows for an increase in the load-carrying capacity of the prism.

3.4.3 The Effect of Unit Size

The effect of unit size is investigated for two-core hollow units ranging from 6” to 12” in depth, all of which are widely available commercial CMUs in the United States. Fig. 3-13 depicts an increase in the ultimate load capacity of the prism (F_{prism}) as the unit size increases, and Eq. 3-6 supplies an empirical representation of this increase using shape factors (i.e., a, b, and c that are given in Fig. 3-13).

$$F_{prism} = a + bf'_{unit} + cf'_{prism\,8"}, \quad \text{Eq. 3-6}$$

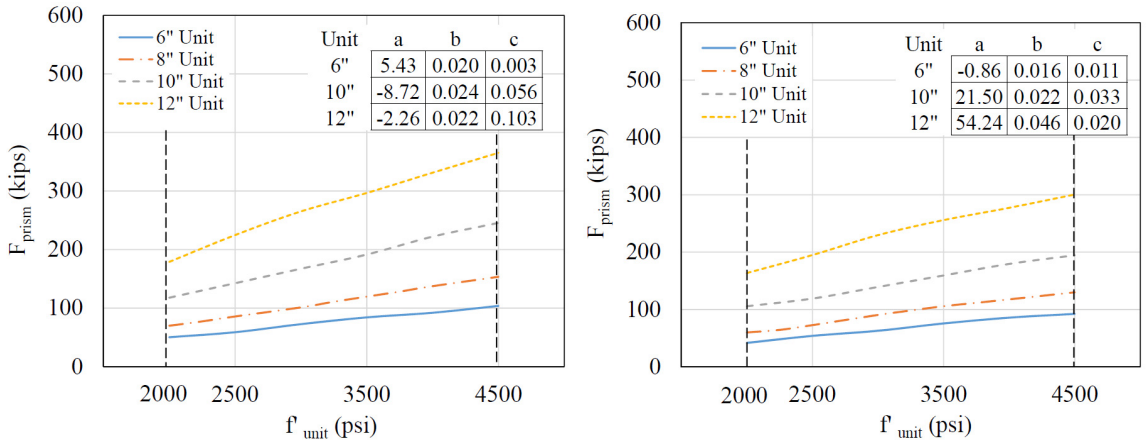

Fig. 3-13. Plots of ultimate force on the prisms for different unit sizes as a function of the compressive strength of (a) ground and (b) unground units.

Fig. 3-14 shows the lateral and axial stress distributions at the face shell along the height of the two types of prisms for different unit sizes at the same load level. However, there is no appreciable difference in the *shape* of stress distribution in that a high concentration of stresses is visible in the contact area between units, indicating a consistent behavior under axial loads for all unit dimensions studied.

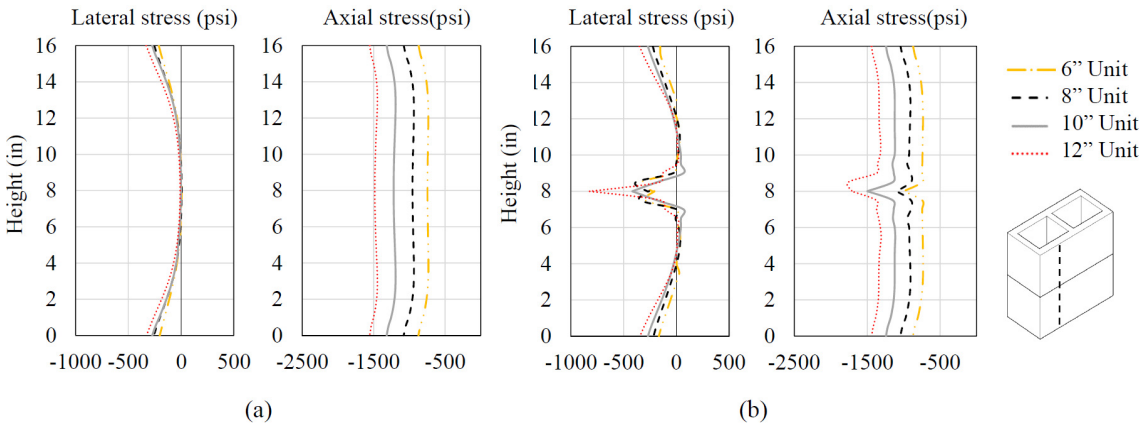

Fig. 3-14. Lateral and axial along the height of prisms with (a) ground and (b) unground units at the same load level.

3.4.4 The Effect of Grouting

To compare the differences in the performance of units with and without grout, the results shown in Fig. 3-15 are evaluated with full grout (with a grout compressive strength of 4400 psi and a modulus of elasticity of 2.2E+6 psi). The results show that for both prisms with ground and unground units, the contribution of the grout to the ultimate compressive strength of prisms is independent of the unit strength. Grout contributes to the ultimate capacity by approximately 1730 and 2000 psi for prisms with ground and unground units, respectively. The ultimate strength of the grouted prisms, however, is nearly identical regardless of whether ground or unground units are used. Different grout strengths are simulated and give similar results. Thus, grouting is observed to diminish the differences in the strength between prisms with ground and unground units. The response of the grouted prisms with ground and unground units can be predicted through Eq. 3-7 and Eq. 3-8, where a valid domain for f'_{unit} is from 2,000 psi to 4,500 psi, and for f'_{grout} is from 2,000 psi to 4,500 psi.

$$f'_{prism} = 346 + 0.5f'_{unit} + 0.43f'_{grout}, \quad \text{Eq. 3-7}$$

$$f'_{prism} = 167 + 0.46f'_{unit} + 0.46f'_{grout}, \quad \text{Eq. 3-8}$$

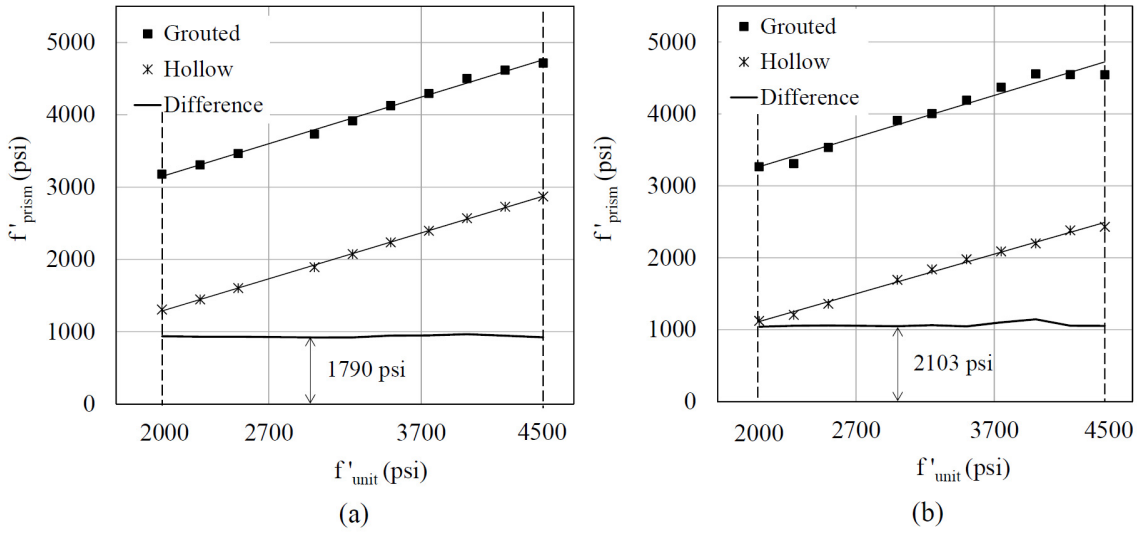

Fig. 3-15. Compressive strength for the hollow and grouted prisms with (a) ground and (b) unground units.

Stress distributions across the height of the face shell for hollow and grouted prisms are compared in Fig. 3-16. This figure also compares the behavior of prisms built with ground and unground unit surfaces. For prisms with ground units, the axial stress distribution before failure is highly uniform; however, for prisms with unground units, a stress concentration in the contact area is noticeable. Stress distribution across the height of the end shell before and after failure is shown in Fig. 3-17 for both hollow and grouted prisms with ground and unground units. In grouted prisms, the axial load laterally expands the grouted core and thus pushes the face shell outward due to the triaxial stress state of the grout. The axial stress is nearly uniform across the height of prisms with ground units;

however, for prisms with unground units, there is a stress concentration in the contact area between units. For lateral stresses, there is again a concentration in the contact area for prisms with unground unit surfaces.

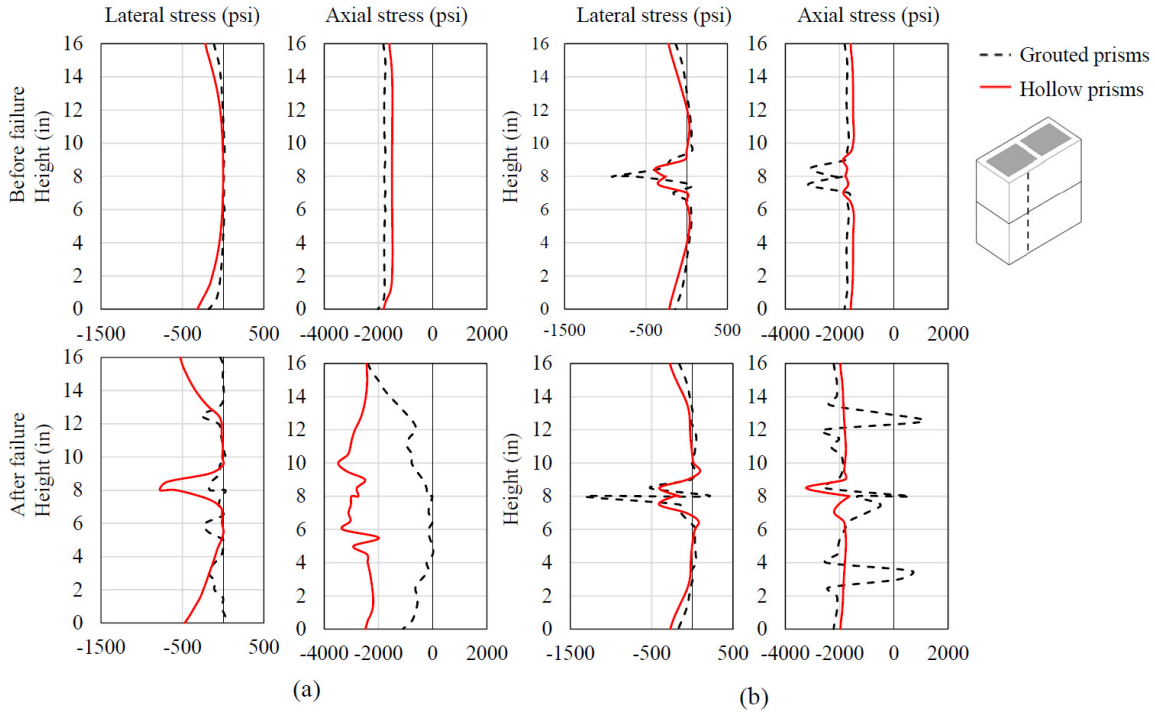

Fig. 3-16. Stress distribution across the height of the face shell before and after failure in the prism with (a) ground and (b) unground units.

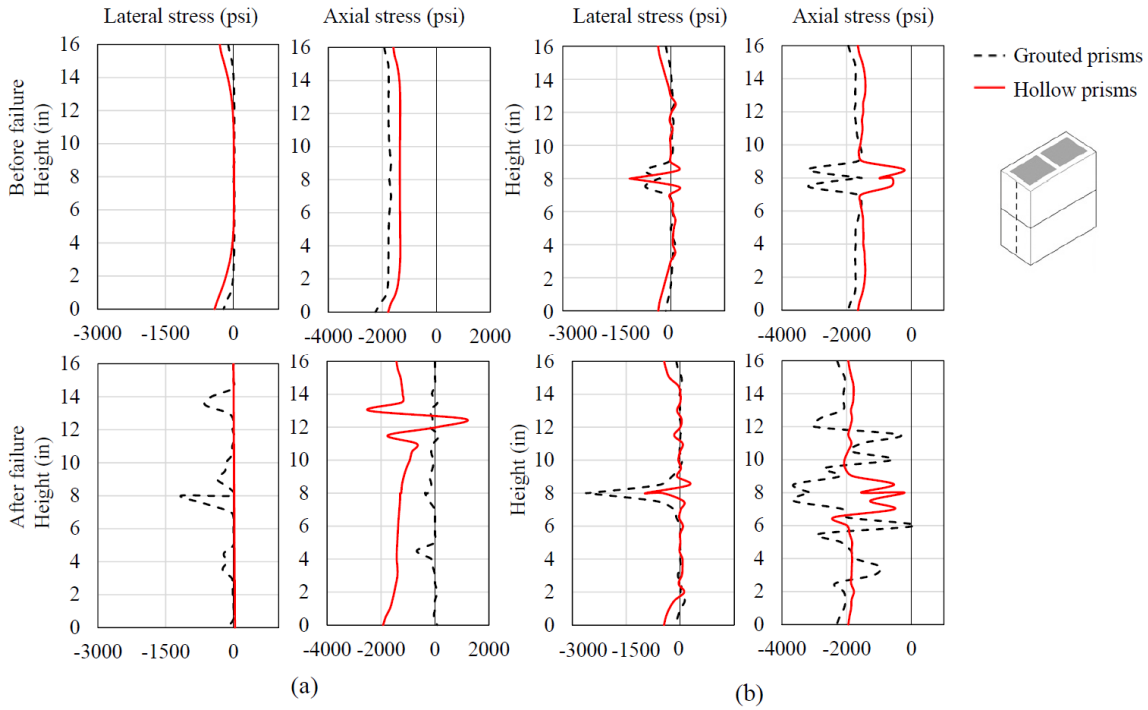

Fig. 3-17. Stress distribution across the height of the end shell before and after failure in the prism with (a) ground and (b) unground units.

Grout and the contact condition between units greatly influence the failure pattern (Fig. 3-18). For both hollow and grouted prisms with ground units (see Fig. 3-18 (a) and (b)), cracking in the end shells is followed by cracking in the web and face shell. Prisms with unground unit surfaces demonstrate a different cracking pattern (see Fig. 3-18 (c) and (d)). For both hollow and grouted prisms, stress concentration in the contact area between units is followed by cracks that appear in the following sequence: the end shell, web, and face shell.

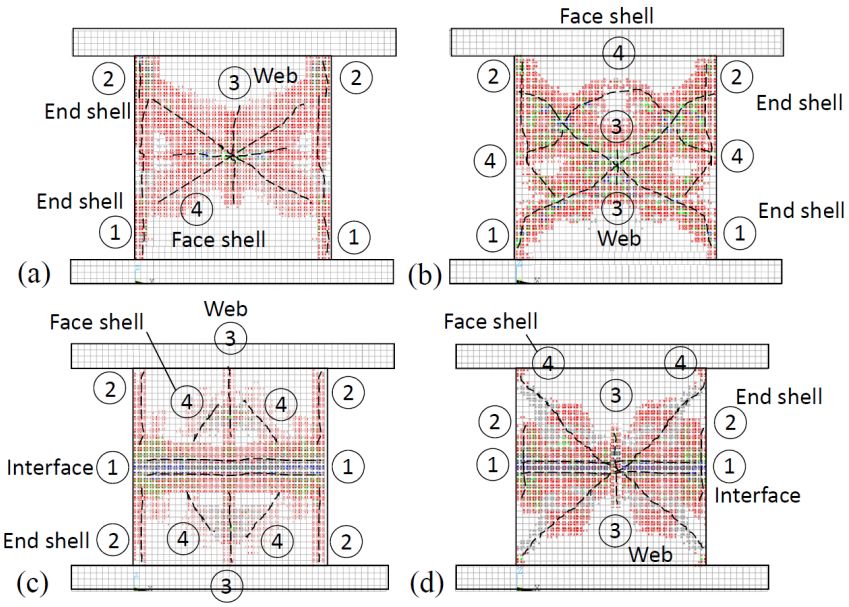

Fig. 3-18. Failure sequence in hollow and grouted prisms with ground and unground units (face shell view): (a) hollow prism (ground units); (b) grouted prism (ground units); (c) hollow prism (unground units); (d) grouted prism (unground units).

3.5 Conclusions

Numerical models provide an efficient means of predicting the structural behavior of dry-stack masonry systems under a variety of conditions without the need for an inordinate number of experiments. In this study, experimental tests on dry-stacked prisms are used to inform and assess the validity of the numerical simulation predictions. The FE models include material nonlinearity and nonlinear boundary conditions at the contact surfaces to capture the local behavior in the models. The FE models incorporate two different levels of surface roughness at the bed joint, i.e., representing prisms with ground and unground units. These two types of prisms exhibit different behaviors under

compressive loads, confirming that the surface topography influences the mechanical behavior of the prisms.

Finally, the FE models are used to predict the behavior of dry-stacked prisms by carrying out a parametric study. The main findings are:

- There is a near-linear relationship between unit strength and prism strength for both ground and unground units and all levels of surface roughness considered in this study. Prisms with unground units exhibit approximately 15% less capacity than prisms with ground units.
- The tensile strength of masonry assemblies is typically approximated as 10% of the compressive strength. Increasing this ratio in increments of 2% (i.e., to 12, 14,...20%) results in an increase in the ultimate capacity by 7-11% for prisms with ground units and 8-12% for prisms with unground units.
- Failure mechanisms of prisms with varying unit sizes are observed to be consistent. This observation holds true for prisms with both ground and unground units. For prisms with ground units, compressive stresses are observed to be uniformly distributed, whereas for prisms with unground units, compressive stresses are concentrated near the bed joint.
- For fully grouted prisms, the grout contributes to the compressive strength by a constant amount independent of the unit strength. This amount, however, depends on whether the units are ground or unground. The ultimate strength of fully grouted prisms with ground and unground units is observed to be nearly identical.

In future studies, the approach presented in this paper for modeling rough unit surfaces can be applied to extend the understanding of dry-stack masonry assemblies under eccentric axial, flexural, and shear loads. However, the seating effect can be monitored with instrumentation during the test to adjust the material model to its characteristics. The modeling technique can also be used to study non-standard units (i.e., those with interlocking components). Based on the results presented herein, look-up tables can be developed and implemented in building codes and specifications for masonry structures.

References

Ainsworth, M. (2001). "Essential Boundary Conditions and Multi-point Constrains in Finite Element Analysis." *Computer Methods in Applied Mechanics and Engineering*, 190(48), 6323-6339.

Anand, K. and Ramamurthy, K. (2000). "Development and Performance Evaluation of Interlocking-Block Masonry." *J. Archit. Eng.*, 10.1061/(ASCE)1076-0431(2000)6:2(45), 45-51.

Anand, K., and Ramamurthy, K. (2005). "Development and Evaluation of Hollow Concrete Interlocking Block Masonry System." *The Masonry Society Journal*, 23(1), 11-20.

Andreev, K., Sinnema, S., Rekkik, A., Allaoui, S., Blond, E., and Gasser, A. (2012). "Compressive Behavior of Dry Joints in Refractory Ceramic Masonry." *Construction and Building Materials*, 34(1), 402-408.

ANSYS® Academic Research. Release 15.0. *Help System, Element Reference* ANSYS, Inc.

ASTM. (2010). "Standard Test Method for Young's Modulus, Tangent Modulus, and Chord Modulus." *ASTM E111-04*, West Conshohocken, PA.

ASTM. (2011). "Standard Test Method for Compressive Strength of Masonry Prism." *ASTM C1314-11a*, West Conshohocken, PA.

ASTM. (2014). "Standard Test Methods for Sampling and Testing Concrete Masonry Units." *ASTM C140/C140M-14*, West Conshohocken, PA.

ASTM. (2015). "Standard Test Method for Measuring Pavement Macrotexture Depth Using a Volumetric Technique." *ASTM E965-15*, West Conshohocken, PA.

ASTM. (2016a). "Standard Specification for Grout for Masonry." *ASTM C476-16*, West Conshohocken, PA.

ASTM. (2016b). "Standard Test Method for Sampling and Testing Grout." *ASTM C1019-16*, West Conshohocken, PA.

ASTM. (2016c). " Standard Practice for Capping Concrete Masonry Units, Related Units and Masonry Prisms for Compression Testing." ASTM C1552-16, West Conshohocken, PA.

Atamturktur, S. (2009). "Verification and Validation under Uncertainty Applied to Finite Element Models of Historic Masonry Monuments." *Proceedings of the IMAC-XXVII*, Orlando, Florida, USA. February 9-12.

Atamturktur, S., Ross, B. E., Thompson, J., and Biggs, D. (2016). "Compressive Strength of Dry-Stacked Concrete Masonry Unit Assemblies." *Journal of Materials in Civil Engineering*, 29(2), 1-4.

Baggio, C., and Trovaluski, P. (1993). "Discrete Models for Joined Block Masonry Walls." *Proc., 6th North American Masonry Conf.,* Drexel University, PA, 939-949.

Bathe, K. (1996). *Finite Element Procedures,* Prentice Hall, NJ.

Beall, C. (2000). "New Masonry Products and Materials." *Prog. Struct. Engng. and Mater.*, 2(3), 296-303.

Bertsekas, D. (1996). *Constrained Optimization and Lagrange Multiplier Methods,* Athena Scientificm, Belmont, Massachusetts.

Campbell, J. (2012). "Numerical Model for Nonlinear Analysis of Masonry Walls." *Ph.D. thesis*, Rheinisch-Westfälischen Technischen Hochschule Aachen University, Aachen, Germany.

Chen, W. (1982). *Plasticity in Reinforced Concrete,* McGraw-Hill, NY.

Contamine, R., Si-Larbi, A., Than, N. Q., and Hamelin, P. (2011). "Numerical Modeling of Reinforced Concrete Beams under Shear Stress with and without External Textile-Reinforced Concrete Reinforcement." *Journal of Reinforced Plastics and Composites*, 30(15), 1293-1303.

Cunningham, P. (2014). "Why Use MPC Based Contact for "Bonded" Connections?." *CAE Associates,* accessed 26 March, 2016, https://caeai.com/.

Dahl, K. (1992). "A Failure Criterion of for Normal and High Strength Concrete." *Rep. R. 286,* Depart. Struc. Engng, Technical Univ. of Denmark, Lyngby, Denmark.

Dahmani, L., Khennane, A., and Kaci, S. (2010). "Crack Identification in Reinforced Concrete Beams Using ANSYS Software." *Strength of Materials*, 42(2), 232-240.

Drucker, D., Prager, W., and Greenberg, H. (1952). "Extended Limit Design Theorems for Continuous Media." *Quart. Appl. Math.*, 9(4), 381-389.

Drysdale, R., Hamid, A., and Baker, L. (1994). *Masonry Structures: Behavior and Design,* Prentice-Hall, NJ.

Fanning, P. (2001). "Nonlinear Models of Reinforced and Post-tensioned Concrete Beams." *Electronic Journal of Structural Engineering*, 2(1), 111-119.

Ferozkhan, M. (2005). "Development of a Dry Stack Masonry System for Effective Resistence to Out-of-Plane Bending." *M.S. thesis,* Central Queensland University, Brisbane, Australia.

Gorst, N.J., Williamson, S.J., Pallett, P.F., and Clark, L.A. (2003). *Friction in Temporary Works,* Research Report 071, University of Birmingham, Edgbaston, Birmingham, UK.

Jaafar, M., Thanoon, W., Najm, A., Abdulkadir, M., and Ali, A. (2006). "Strength Correlation between Individual Block, Prism and Basic Wall Panel for Load Bearing Interlocking Mortarless Hollow Block Masonry." *Construction and Building Materials*, 20(7), 492-498.

Jackson, R., and Streator, J. (2006). "A Multi-scale Model for Contact between Rough Surfaces." *Wear*, 261(1), 1337-1347.

Kachlakev, D., Miller, T., Yim, S., Chansawat, K., and Potisuk, T. (2001). *Finite Element Modeling of Reinforced Concrete Structures Strengthened with FRP Laminates,* Final Report: Oregon Department of Transportation, OR.

Kaushik, H., Rai, D., and Jain, S. (2007). "Stress-Strain Characteristics of Clay Brick Masonry under Uniaxial Compression." *J. Mater. Civ. Eng.*, 10.1061/(ASCE)0899-1561(2007)19:9(728), 728-739.

Klingner, R. (2010). *Masonry Structural Design.* McGraw-Hill Education, NY.

Köksal, H. O., Karakoc, C., and Yildirim, H. (2005). "Compression Behavior and Failure Mechanisms of Concrete Masonry Prisms." *Journal of Materials in Civil Engineering*, 17(1), 107-115.

Kwasniewski, L. (2013). "Application of Grid Convergence Index in FE Computation." *Bulletin of the Polish Academy of Sciences*, 61(1), 123-128.

Laursen, T. (2003). *Computational Contact and Impact Mechanics,* Springer, NY.

Lin, K., Totoev, Y., Liu, H., and Wei, C. (2015). "Experimental Characteristics of Dry Stack Masonry under Compression and Shear Loading." *Materials*, 8(12), 8731-8744.

Lourenço, P. B., Oliveira, D. V., Roca, P., and Orduña, A. (2005). "Dry Joint Stone Masonry Walls Subjected to In-plane Combined Loading." *Journal of Structural Engineering*, 131(11), 1665-1673.

Lü, W., Wang, M., and Liu, X. (2011). "Numerical Analysis of Masonry Under Compression via Micro-Model." *Advance Materials Research* 243-249, 1360-1365.

Madenci, E., and Guven, I. (2015). *The Finite Element Method and Applications in Engineering Using ANSYS,* Springer, NY.

Mahboubi, A., and Ajorloo, A. (2005). "Experimental Study of the Mechanical Behavior of Plastic Concrete in Triaxial Compression." *Cement and Concrete Research*, 35(1), 412-419.

Marzahn, G. (1999). "Investigation on the Initial Settlement of Dry-stacked Masonry Under Compression." *Liepzig Annual Civil Engineering Report 3,* 353-365.

Michel, K. (2015). "Failure Behaviour of Masonry under Compression Based on Numerical and Analytical Modelling." *Ph.D. Dissertation*, Technische Universität Dresden, Germany.

MSJC, Masonry Standards Joint Committee. (2013). *Building Code Requirements and Specification for Masonry Structures and Related Commentaries,* TMS 602-11/ACI 530.1-11/ASCE 6-11, Boulder, CO.

Murray, E. (2007). "Dry Stacked Surface Bonded Masonry - Structural Testing and Evaluation." *M.S. thesis,* Brigham Young University, Provo, UT.

Oh, K. (1994). "Development and Investigation of Failure Mechanism of Interlocking Mortarless Block Masonry System." *Ph.D. Dissertation.* Drexel University, PA.

Parvanova, S., Kazakov, K. S., Kerelezova, I., Gospodinov, G., and Nielsen, M. P. (2005). "Modelling the Nonlinear Behaviour of R/C Beams with Moderate Shear Span and Without Stirrups using ANSYS". *Proc. of Scientific International Conference, VSU "Liuben Karavelov"*, 26-27 May, Sofia, Bulgaria

Pave, R. (2007). "Strength Evaluation of Dry-stack Masonry." *M.S. thesis,* University of the Witwatersand, Johannesburg, South Africa.

Peng, W., and Bhushan, B. (2001). "Three-dimensional Contact Analysis of Layered Elastic/Plastic Solids with Rough Surfaces." *Wear*, 249(1), 741-760.

Prabhu, S., Atamturktur, S., Brosnan, D., Messier, P., and Dorrance, R. (2014). "Foundation Settlement Analysis of Fort Sumter National Monument: Model Development and Predictive Assessment." *Engineering Structures*, 65(1), 1-12.

Ramamurthy, K., and Nambiar, K. (2004). "Accelerated Masonry Construction: Review and Future Prospects." *Progress in Structural Engineering and Materials*, 6(1), 1-9.

Roache, P.J. (1994). "Perspective: A Method for Uniform Reporting of Grid Refinement Studies." *ASME J. Fluids Eng.,* 116(3), 405-413.

Rots, J. G., and Blaauwendraad, J. (1989). "Crack Models for Concrete, Discrete or Smeared? Fixed, Multi-Directional or Rotating?." *HERON*, 34 (1), 5-59.

Safiee, N., Jaafar, M., Noorzaie, J., and Kadir, M. (2009). "Finite Element Analysis of Mortarless Wall Panel." *Report and Opinion*, 1(2), 1-16.

Salas, C., and Sánchez, H. (2012). "Structural Behavior of Process Steel Towers Submitted to Seismic Actions." *Proc. 15th World Conference on Earthquake Engineering,* Lisbon, Portugal.

Sayed-Ahmed, E. Y., and Shrive, N. G. (1996). "Nonlinear Finite-Element Model of Hollow Masonry." *Journal of Structural Engineering*, 122(6), 683-690.

Schwer, L. (2008). "Is Your Mesh Refined Enough? Estimating Discretization Error Using GCI." *7th LS-DYNA Anwenderforum,* Bamberg, I-I-45-54.

Sellgren, U., Björklund, S. and Andersson, S. (2003). "A Finite Element-based Model of Normal Contact between Rough Surfaces." *Wear*, 254(11), 1180-1188.

Stefanou, I., Sab, K., and Heck, J. V. (2015). “Three-Dimensional Homogenization of Masonry Structures with Building Blocks of Finite Strength: A Closed Form Strength Domain.” *International Journal of Solids and Structures*, 54, 258-270.

Subramani, T., Manivannan, R., and Kavitha, M. (2014). "Crack Identification in Reinfoced Concrete Beams Using Ansys Software." *Journal of Engineering Research and Applications*, 4(6), 133-141.

Thamboo, J. A., Dhanasekar, M., and Yan, C. (2013). “Flexural and Shear Bond Characteristics of Thin Layer Polymer Cement Mortared Concrete Masonry.” *Construction and Building Materials*, 46(1), 104-113.

Thamboo, J. A., and Dhanasekar, M. (2015). “Characterisation of Thin Layer Polymer Cement Mortared Concrete Masonry Bond.” *Construction and Building Materials*, 82, 71-80.

Thanoon, W., Jaafar, M., Noorzaei, J., Razali, M., Kadir, A., and Fares, S. (2007). "Structural Behavior of Mortar-Less Interlocking Masonry System Under Eccentric Compressive Loads." *Advances in Engineering,* 10(1), 11-24.

Truong-Hong, L., and Laefer, D.F. (2008). "Micro vs. Macro Models for Predicting Building Damage Underground Movements." *Proc. International Conference on Computational Solid Mechanics,* Hochiminh City, Vietnam, 1-10.

Vasconcelos, G., and Lourenço, P. (2009). "Experimental Characterization of Stone Masonry in Shear and Compression." *Construction and Building Materials*, 23(11), 3337-3345.

Willam, K., and Warnke, E. (1974). "Constritutive Model for the Triaxial Behavior of Concrete." *Proc. Seminar on Concrete Structures Subjected to Triaxial Stresses,* Int. Association of Bridge and Structural Engineering, Zurich, Switzerland.

Yastrebov, V., Anciaux, G., and Molinari, J. (2012). "Contact between Representative Rough Surfaces." *Physics Review*, 86(3), 1-18.

Yastrebov, V., Anciaux, G., and Molinari, J. (2015). "From Infinitesimal to Full Contact between Rough Surfaces: Evolution of the Contact Area." *Journal of Solids and Structures*, 52(1), 83-102.

CHAPTER FOUR

EXPERIMENTAL AND NUMERICAL EVALUATION OF REINFORCED DRY-STACKED CONCRETE MASONRY WALLS

4.1 Introduction

In dry-stack concrete masonry construction, the units are laid without mortar bonding the joints. This type of masonry construction requires smaller amounts of wet material and reduces the need for highly skilled labor, thereby reducing workmanship cost (Murray 2007; Uzoegbo et al. 2007) and a significantly improved efficiency (Anand and Ramamurthy 2003). Mortarless construction is, however, a low bending capacity system. Hence, the dry-stacked walls resisting lateral loads (e.g., wind, soil pressure, seismic loads, and eccentric gravity loads) need to be augmented to increase their bending capacity through the use of interlocking units, grouting, steel reinforcement, post-tensioning, surface bonding or a combination of these techniques (Glitza 1991; Lohr 1992; Marzahn 1997; Biggs 2002; Murray 2007; Biggs and Forsberg 2008; Okail et al. 2016; Sokairge et al. 2017).

Over the last three decades, several proprietary mortarless construction systems, a significant portion of which involve interlocking units, have become available on the market. The studies investigating these proprietary systems constitute the vast majority of the literature on dry-stack construction (Hatzinikolas et al. 1986; Vargas 1988; Harris et al. 1992; Hines 1993; Drysdale and Guo 1995; Anand and Ramamurthy 2000; Uzoegbo 2001; Thanoon et al. 2004; Uzoegbo and Ngowi 2004; Ferozkhan 2005; Ngowi 2005; Pave 2007; Safiee et al. 2011; Molnár and Jönsson 2012). The primary focus of the pertinent literature

on the various shapes and forms of these proprietary interlocking units and the scarcity of generally applicable findings regarding the behavior of dry-stack masonry systems have hindered the development of a unifying building code that can regulate construction with mortarless masonry assemblies.

To help address this knowledge gap, the present study aims to obtain generalizable findings regarding the behavior of dry-stacked wall systems. In this study, we focused on standard (8 in.×8 in.×16 in.) concrete masonry units (CMUs), i.e., the CMU type most commonly used in the United States (Heiserman 2015) and developed experimentally validated finite element (FE) models to reduce the need to conduct resource-intensive experimentation. The purpose of the FE models developed herein is to predict the ultimate behavior of the walls. Hence, to realistically represent the mechanics of the structural failure, major sources of nonlinear behavior are taken into account in these models, including: (1) material nonlinearity (i.e., the nonlinear characteristics of the concrete masonry units, grout, and reinforcing bars) due to plasticity, cracking, and crushing; (2) geometric nonlinearity due to large displacements prior to failure (i.e., P-Δ effects); and (3) contact nonlinearity due to changes in stiffness when bodies come in or out of contact with each other. To ensure that the FE models are accurate representations of reality, model predictions were checked against laboratory experiments. After experimental validation, the FE models were then used to investigate the ultimate behavior and failure modes of various wall designs, providing a wide range of wall performance of dry-stacked walls to aid in the development of future design codes.

4.2 Reinforced Dry-stacked Concrete Masonry Walls Test

To obtain experimental data regarding the flexural behavior of reinforced, grouted dry-stacked masonry walls, four nominally identical wall specimens are tested under 4-point out-of-plane loading using a self-reacting steel test frame and a hydraulic jack (Fig. 4-1 (a)). The wall specimens are set to stand vertically on a frictionless ground surface to withstand lateral loads imparted by frictionless rollers at two loading and two supporting lines. To prevent local crushing of the CMU at the loading locations, light-gauge steel platens are positioned between the walls and rollers. The two-line loads are applied by a hydraulic actuator, ENERPAC RCH302, bolted to the self-reacting steel frame.

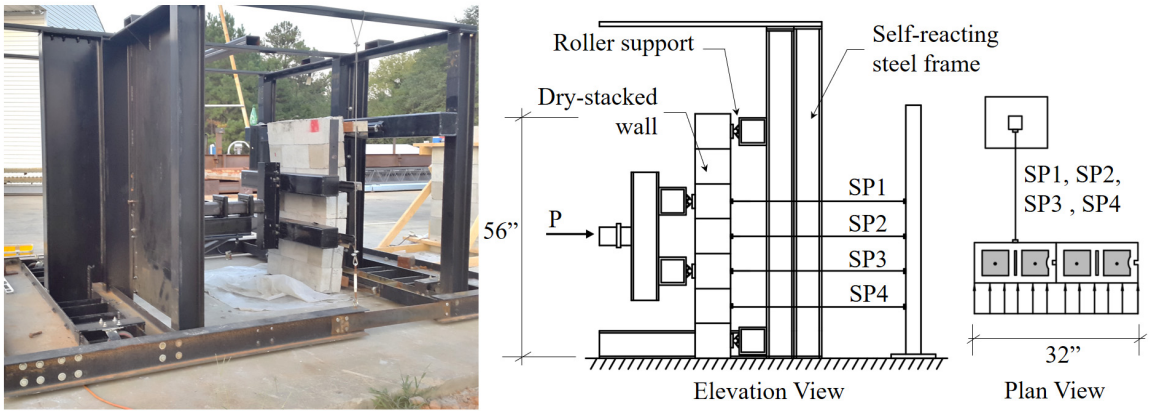

Fig. 4-1. Representative dry-stacked wall test setup, (a) photo taken during experiments and (b) elevation view and plan view.

The wall specimens are 32 in. (two units) wide by 56 in. (seven courses) high, and are built with nominal 8 in.×8 in.×16 in. CMUs to meet the requirements of ASTM C90 (ASTM 2016c), with half-units being placed at the ends of every second course. The wall specimens are fully grouted with pre-mixed non-shrink grout prepared on site and

reinforced with No. 3 reinforcing steel bars constituting 0.18% of the cross-sectional area of the wall. When the wall is fully engaged, the applied load is measured with a pressure gauge and the corresponding wall displacement is measured with string pots at four locations as shown in Fig. 4-1 (b), i.e., at the height of line loads (SP1 and SP3), mid-height (SP2), and between the lower support and line load (SP4). The load and the displacement data recorded during the experiments are shown in Table 4-1.

Table 4-1. Wall test results for SP locations.

Wall	Ultimate Load (k)	Ultimate Displacements (in.) SP1	SP2	SP3	SP4
W1	23.520	1.348	1.603	1.475	0.907
W2	23.021	1.595	2.238	2.026	1.289
W3	26.129	1.472	2.029	1.836	1.119
W4	24.571	1.501	2.043	1.867	1.032
Mean	24.307	1.475	1.975	1.795	1.087

4.3 Numerical Models for Reinforced Dry-Stacked Walls

In parallel with the laboratory experiments, FE models are developed in ANSYS v.15 to numerically simulate the behavior of the tested reinforced dry-stacked concrete masonry walls (see Fig. 4-2). These FE models are developed using the actual unit dimensions of a concrete masonry two-core stretcher with a 7⅝ in. depth and height, a 15⅝ in. length, a 1¼ in. thickness in the face shell, and a 1 in. thickness in the end shell and web. Fillets at the inner and outer edges and the tapering of the web are excluded from the model geometry to simplify the mesh discretization.

The interfaces between the CMUs are modeled using contact elements to reflect the discontinuity (i.e., lack of bonding) between units in dry-stack construction. The grout in

the cells is modeled monolithically along the height of the wall, and full bonding is assumed between the grout and the CMUs as well as between the grout and the reinforcing bars.

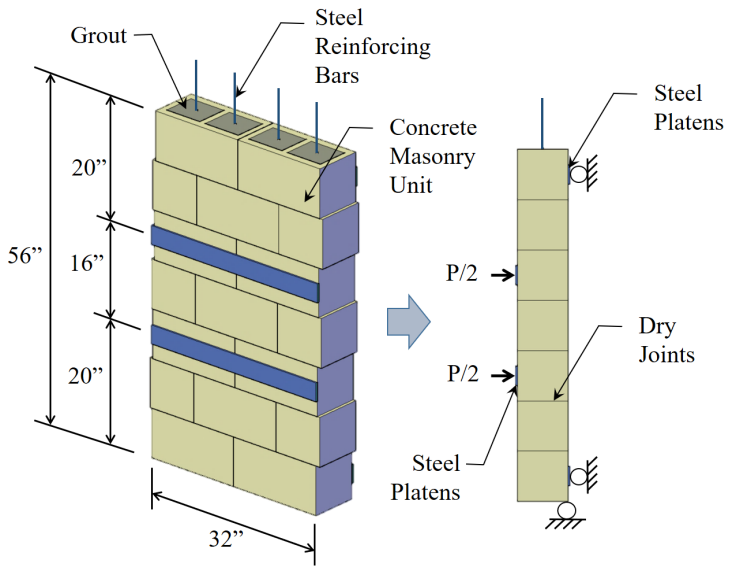

Fig. 4-2. Reinforced dry-stack concrete masonry wall model.

In representing the 4-point bending scenario, steel platens are modeled to as uniformly distributing the load at the point of contact along the width of the wall to prevent stress concentrations. Two platens are located on one side of the wall to act as supports and to represent part of the self-reacting steel test frame discussed in Section 2. These platens are attached to the wall to allow rotations but to restrain horizontal movement. On the other side of the wall, two more platens are modeled attached to the units to distribute the line loads applied by the hydraulic jack. The frictionless boundary condition at the base of the wall is represented by restraining vertical movements but allowing rotations and lateral movement at the edge of the bottom of the wall as shown in Fig. 4-2.

4.3.1 Element Types and Material Models

Elements types and material models are selected to represent two major effects (see Fig. 4-3), (i) *cracking* and *crushing* in the grout and/or units and (ii) *plasticity* in the grout and/or units and in the steel reinforcing bars.

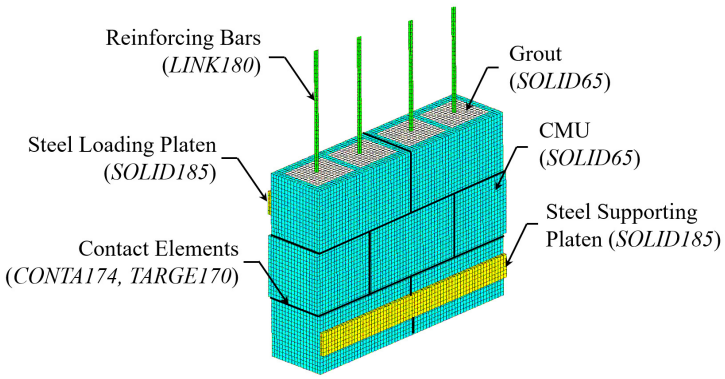

Fig. 4-3. Element types in the reinforced dry-stacked wall.

Concrete Masonry Units and Grout. Concrete masonry units and grout are modeled using the *SOLID65* element from the ANSYS library. *SOLID65* is an 8-noded three-dimensional solid isoparametric hexahedron capable of crushing in compressive and cracking in tensile stresses. The material behavior of the units and the grout is represented under triaxial conditions based on the Drucker-Prager yield criterion (Drucker et al. 1952) in earlier stages of the loading and based on the Willam-Warnke failure criterion (Willam and Warnke 1974) in the later stages, i.e., at the strength limit of the materials. These surfaces are shown schematically in Fig. 4-4.

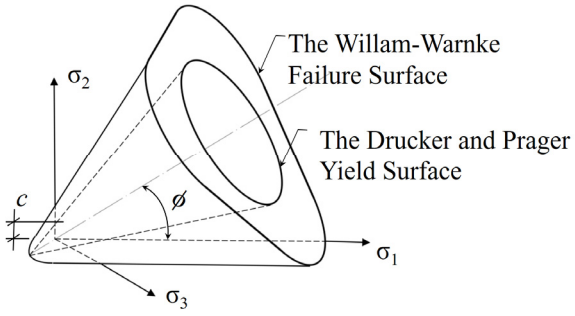

Fig. 4-4. Schematic failure surfaces of the units and grout material in the three orthogonal dimensions of the stress space.

The Drucker-Prager criterion introduces a perfectly plastic behavior after the elastic limit has been reached and before crushing and cracking occur. Widely implemented for masonry structures (Sayed-Ahmed and Shrive 1996; Köksal et al. 2004; Angelillo et al. 2010), this criterion defines a surface formed in the principal stress space that takes into account the plastic-flow ability. This surface is characterized by two defining parameters: internal friction angle ϕ and cohesion c. In this study, ϕ=36.65°-*1.1°*(f_{unit}/1000*)*, proposed by Dahl (1992) and Mahboubi and Ajorloo (2005), and $c=f_{unit}/4$, proposed by Chen (1982), are used to represent the CMUs, and $\phi=0.01f_{grout}$, and $c=0.129f_{grout}+268.32$, proposed by Köksal et al. (2005), are used to represent the grout.

The Willam-Warnke criterion defines the cracking and crushing conditions of elements. Cracking occurs when the principal tensile stress in any direction lies outside its failure surface. In a cracked element, the stiffness of the finite element at the integration point is set to 0.6 (as a default value) in the direction parallel to the principal tensile stress orientation to ensure convergence of the calculations (Betti and Galano 2012; Prabhu et al. 2014). Similarly, crushing occurs when the principal stresses of the element are in

compression and lie outside the Willam-Warnke failure surface. After crushing occurs, the stiffness of the element at the integration point is set to 0.5 in all directions of the principal stresses to ensure a converged solution. The Willam-Warnke failure surface is expressed in terms of five input parameters: the ultimate uniaxial tensile strength (f_t), the compressive strength (f'_c), the biaxial compressive strength (f_{cb}=1.2f'_c), the ultimate compressive strength for a state of biaxial compression (f_1=1.45f'_c), and an ultimate compressive strength for a state of uniaxial compression (f_2=1.725f'_c) (Kachlakev 2001).

With *SOLID65* elements, shear transfer coefficients for open (β_t) and closed (β_c) cracks must also be defined. These coefficients reflect the shear strength reduction factor for loads that induce sliding across the crack face. Shear transfer coefficients range from values of 0 to 1, with 0 representing a smooth crack with no shear transfer and 1 a rough crack with full shear transfer. In the present study, β_t is set to 0.2 and β_c to 0.6.

Reinforcing Bars. Reinforcing bars embedded in grout are most commonly represented through one-dimensional link elements that have nodes coincident with the tridimensional solid elements of the surrounding grout as shown in Fig. 4-5 (Tavárez 2001; Ramadan et al. 2009; Kamonna 2010; Ashour 2016). This node-sharing ensures displacement compatibility and a perfect bond between the grout and the steel reinforcing bars in the FE model.

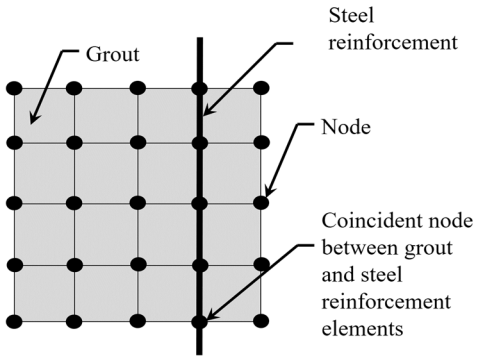

Fig. 4-5. Coincident nodes between *SOLID65* and *LINK180* elements.

In this study, steel reinforcing bars are modeled using the *LINK180* element. This element is a uniaxial spar capable of carrying an axial load and is defined by two nodes with three translational degrees of freedom at each. While the *LINK180* element does not allow bending due to its pin-jointed configuration, it allows plasticity, creep, rotation, large deflection, and large strain to be considered. Herein, a bilinear isotropic hardening plasticity model based on the Von Mises failure criteria is adopted for the steel reinforcing bars (Asare 2015; Elmezaini and Ashour 2015). The initial slope of the stress-strain curve is defined by the modulus of elasticity until the yield stress is reached, beyond which the material model is defined by the tangent modulus, which is set to 0.01 times the initial modulus of elasticity.

Steel Platens. In accordance with the experiments, one-quarter inch thick steel platens are added at the locations of the point loads and horizontal supports. These platens, modeled using 8-noded isoparametric *SOLID185* hexahedron elements, are put in place to provide an even stress distribution over an area across the loading and supporting lines. Nodes aligned along the center of the steel platens are used as loading and support points for the wall, allowing rotation of the platens (Recall Fig. 4-2).

Contact Elements. The 8-noded *CONTA174* and *TARGE170* elements are used to model the deformations and load transfer between the dry-stacked units. A "contact surface" and a "target surface" form a contact pair to represent sliding in the tangential direction and translation in the normal direction. The contact and target elements have three translational degrees of freedom at each node and are located on the surfaces of the three-dimensional *SOLID65* elements.

4.3.2 Material Properties Values

To determine the material properties of CMUs, five individual units are tested according to ASTM C140 (ASTM 2014) using a SATEC Systems M11-400RD universal testing machine (Fig. 4-6). The compressive strength is determined as the average of the measurements of applied compressive force at failure, while the modulus of elasticity of the CMUs is the average of the slope of the chord modulus between 5% and 33% of the unit strength according to ASTM E111 (ASTM 2010). The unit tensile strength is approximated as 10% of the compressive strength (Klingner 2010). To determine the material properties of the grout used to build the walls, five grout samples are prepared according to ASTM C1019 (ASTM 2016b) and tested based on ASTM C39 (ASTM 2016a) to determine the compressive strength and the modulus of elasticity. Past studies suggest that grout tensile strength falls between 8% and 15% of its compressive strength (Wight and MacGregor 2011); accordingly, a tensile to compressive strength ratio of 10% is selected for this study. The material properties of the reinforcing bars are defined as specified by the manufacturer. Table 4-2 lists the material properties of the CMUs, the grout, and the reinforcing bars.

Fig. 4-6. Experimental setup of the CMU test.

Table 4-2. Material properties by testing.

CMU (unit)	Compressive strength (f_{unit})	2,131 ± 61 psi
	Tensile strength (ft_{unit})	213 psi
	Modulus of elasticity (E_{unit})	2,000,000 psi
Grout	Compressive strength (f_{grout})	5,700 ± 751 psi
	Tensile strength (ft_{grout})	570 psi
	Modulus of elasticity (E_{grout})	1,333,333 psi
Reinforcing Bars	Designation	No. 3
	Cross-section area (A_s)	0.11 in^2
	Yield stress (f_y)	69,000 psi
	Ultimate stress (f_u)	107,000 psi
	Modulus of elasticity (E_s)	29,000,000 psi

4.3.3 Mesh Refinement Study

Previous research has demonstrated that dry-stacked concrete masonry systems behave in a highly nonlinear fashion (De Castro 2003), the modeling of which in FE analysis requires a careful evaluation of the numerical uncertainties that arise from the mesh discretization (Hemez 2005; Roache 2009). Accordingly, a mesh convergence study is conducted to determine a mesh size that yields a balance between solution accuracy and

computational time. This is important because an excessively coarse mesh can degrade solution accuracy, while an excessively fine mesh can result in prohibitive computational demands.

The Grid Convergence Index (GCI) is a widely used estimator for numerical uncertainties that result from discretization (Schwer 2008; Atamturktur 2009; Roache 2009; Kwaśniewski 2013). The GCI is calculated as $GCI=(F_s\,\varepsilon)/(R^p-1)\times 100\%$, where F_s is a factor of safety with a suggested value of 1.25 when three mesh sizes are evaluated; ε is the difference between subsequent solutions for a group of meshes (i.e., fine (Δ_F) to medium (Δ_M) and medium (Δ_M) to course (Δ_C)); R denotes the refinement ratio, which is the ratio of mesh sizes; and p denotes the order of convergence.

In evaluating different mesh sizes, the lateral displacement of the wall at mid-height $y(\Delta x)$ is predicted under three different load levels. Load level P_1=2,500 lbs leads to the wall behaving in a linear, elastic manner, while load levels P_2=7,500 lbs and P_3=12,500 lbs lead to the wall behaving in a nonlinear, inelastic manner due to extensive cracking and/or crushing elements. At these three load levels, three different mesh sizes are evaluated: Δ_F=0.5 in., Δ_M=1 in., and Δ_C=2 in. Fig. 4-7 shows the solution error versus the mesh size on a log-log scale. As the mesh size is refined, the displacement response ($y(\Delta x)$) converges from above, meaning that the numerical solutions overestimate the reference solution ($y_{reference}$).

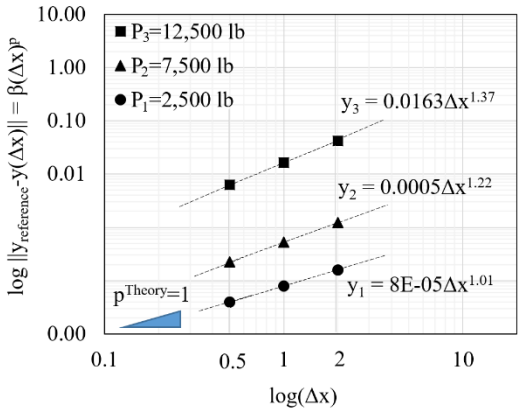

Fig. 4-7. Mesh refinement study showing an asymptotic convergence behavior at three load stages.

In Fig. 4-7, the slope of the curves represents the rate of convergence p to the reference solution as mesh size is reduced (i.e., as $\Delta x \rightarrow 0$). The calculated rate of convergence should ideally match the theoretical first-order convergence (i.e., $p^{theory}=1$) expected from *SOLID65* elements with linear shape functions. When the rate of convergence is calculated for the low load amplitude (P_1=2,500 lbs) as shown in Table 4-3, the value of p is observed to be close to 1, confirming the expected behavior $\Delta x \rightarrow 0$.

Table 4-3. Results of grid convergence index.

Load (lbs)	$GCI_{F\text{-}M}$ (%)	$GCI_{M\text{-}C}$ (%)	p	$GCI_{M\text{-}C}/R^pGCI_{F\text{-}M}$
P_3=12,500	9.61	23.21	1.37	1.20
P_2=7,500	2.88	6.57	1.22	1.14
P_1=2,500	1.38	2.74	1.01	0.98

An increase in the applied lateral load, however, results in more pronounced cracking and crushing of the CMUs. Hence, when the load amplitude P increases, so does the nonlinearity of the response. This is observed in Table 4-3 with increasing deviation of the calculated p from theoretical value of 1.0 as well as increasing GCI values for

increasing load levels, both of which in turn make a finer mesh necessary. Hence, the appropriate mesh size must be evaluated at the highest expected load to be applied to the system. At load amplitude P3, the numerical uncertainty in lateral displacement at mid-height obtained with fine-medium mesh is 9.6%, which is lower than the experimental variability of 18.8% observed for the same response. Therefore, a fine mesh of 0.5 in. was deemed to provide an acceptable level of numerical uncertainty.

4.4 Experimental Validation of the Numerical Models

The experimental observations discussed earlier in Section 2 were compared against model predictions to assess the predictive abilities of the FE model discussed in Section 3 (see similar studies on experimental validation of numerical models of masonry systems: Sekender and Page 1988; Gabor et al. 2006; Atamturktur et al. 2012a; Atamturktur et al. 2012b). Specifically, the failure pattern, the separation at the joints between the CMUs, and the load and displacement responses of the walls were evaluated with this comparison.

Failure pattern. As seen in Fig. 4-8 and Fig. 4-9, the numerical predictions agree with the experimental observations in both the failure mode and the pattern of the cracks. In both the experiments and the numerical simulations, dry-stacked masonry walls are observed to fail in a ductile manner under flexure (Fig. 4-8). Horizontal tensile cracks first form in the grout surrounding the reinforcement facing the tension face of the unit cell.

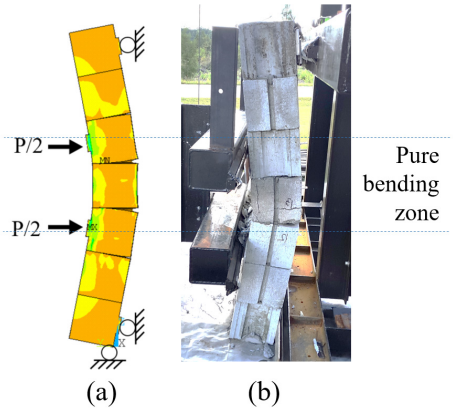

Fig. 4-8. Failure pattern comparison at ultimate: (a) numerical model and (b) experiments.

As shown in Fig. 4-9, the experiments and the model predictions agree that these cracks have a conical pattern at the bed joints concentrated in the pure bending zone. Such cracks would reduce the bond stresses between the grout and the reinforcing steel bars.

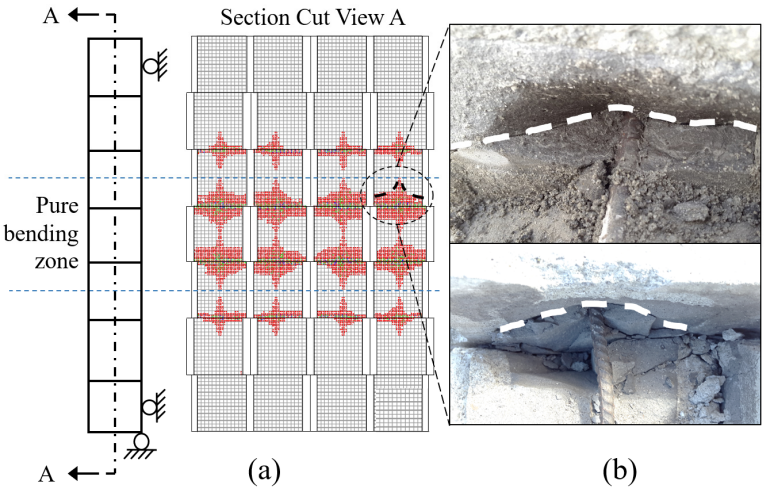

Fig. 4-9. Visual comparison regarding the crack pattern of the grout: (a) numerical model and (b) experiments at ultimate load.

The model predictions also agree with the experimental observations in the compression failure of the units as shown in Fig. 4-10. The cracks in the units first formed

in the tension face within the pure bending zone and then extended along the grout depth toward the compression face, causing crushing around the joints. The location and size of the crushed regions observed during the experiments agree with the model predictions.

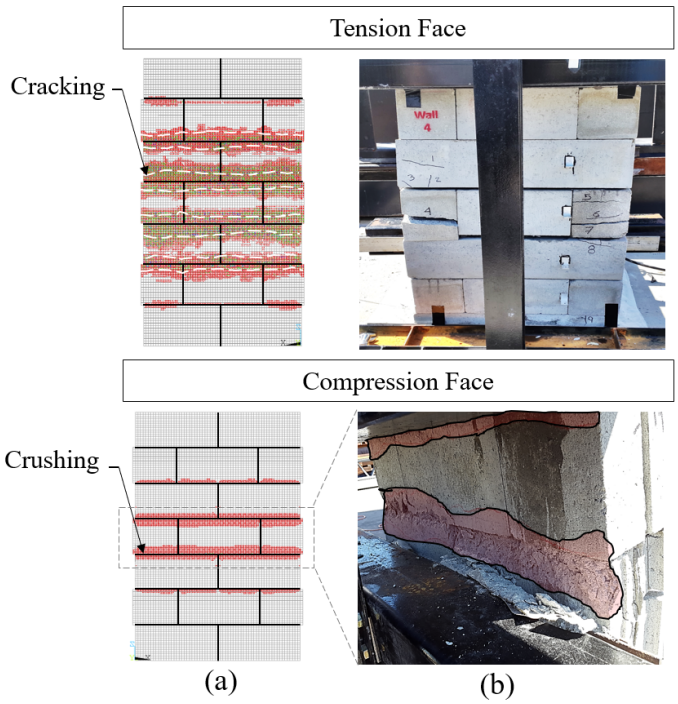

Fig. 4-10. Cracking in the tension face and crushing in the compression face of the units: (a) FE model and (b) experiments at ultimate load.

Separation at the bed joints. At the ultimate load, separations between the CMUs at the bed joints are measured with a caliper at several locations on the walls as shown in Fig. 4-11. Specifically, the extent of the separations is measured on the tension face at the pure bending zone (O21-O23 and 031-O33), outside the pure bending zone (O11-O13 and O41-43), and at the contact point with the ground on the compression face (O51-O53). The minimum and the maximum separations from the measurements of the four walls tested at

each location are listed in Table 4-4. Also available in this table is the separation predicted by the FE model at the ultimate load.

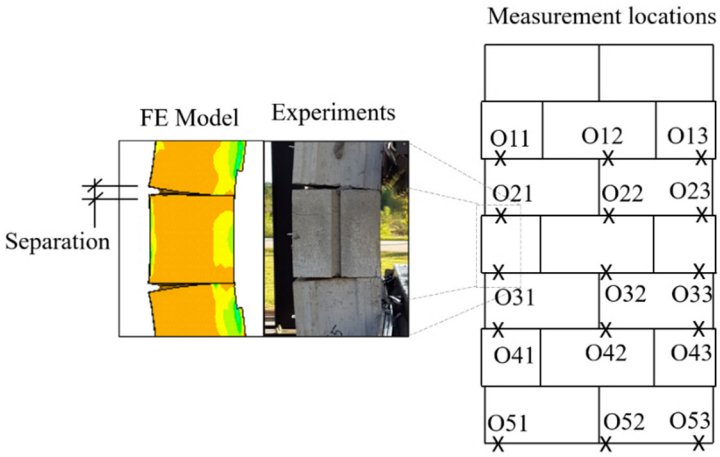

Fig. 4-11. Location of separation measurements at the bed joints.

Table 4-4. Results of separation measurements at the bed joints at ultimate load.

Location	Measurements		FE Model (in.)	Within range?
	Min. (in.)	Max. (in.)		
O11	0.039	0.191	0.159	Yes
O12	0.131	0.257	0.176	Yes
O13	0.117	0.170	0.158	Yes
O21	0.394	0.628	0.462	Yes
O22	0.310	0.579	0.472	Yes
O23	0.308	0.516	0.466	Yes
O31	0.319	0.653	0.464	Yes
O32	0.202	0.961	0.474	Yes
O33	0.421	0.803	0.464	Yes
O41	0.039	0.325	0.159	Yes
O42	0.202	0.314	0.178	No
O43	0.180	0.422	0.162	No
O51	0.813	1.219	1.319	No
O52	0.825	1.219	1.329	No
O53	0.720	1.215	1.318	No

Table 4-4 shows that the separations predicted by the FE model are within the range of separation measured during the test, except for the lower region on the wall. The separation observed in the lower region is overpredicted by the model by about 10%. This discrepancy could be explained by the fact that residual friction forces at the contact where the walls rest on the ground during the experiments are omitted in the FE models, in which this boundary condition is represented with a non-frictional surface.

Load-displacement wall response. Fig. 4-12 presents the numerically and experimentally obtained load-displacement curves at different locations along the height (SP1-SP4 as discussed in Section 2), which are in acceptable agreement. The load and displacement values are compared in **Error! Reference source not found.** at three significant stages: (1) the initiation of cracking in the unit and/or grout; (2) the yielding of the steel reinforcing bars; and (3) the ultimate load-carrying capacity when the units are crushed.

Table 4-5. Ultimate load and displacement comparison.

Response	Measurements		FE Model	Within range?
	Min	Max.		
Disp. @ SP1 (in.)	1.340	1.590	1.971	No
Disp. @ SP2 (in.)	1.603	2.240	2.382	No
Disp. @ SP3 (in.)	1.470	2.020	1.901	Yes
Disp. @ SP4 (in.)	0.910	1.290	1.024	Yes
Ult. Load (kip)	23.020	26.120	24.731	Yes

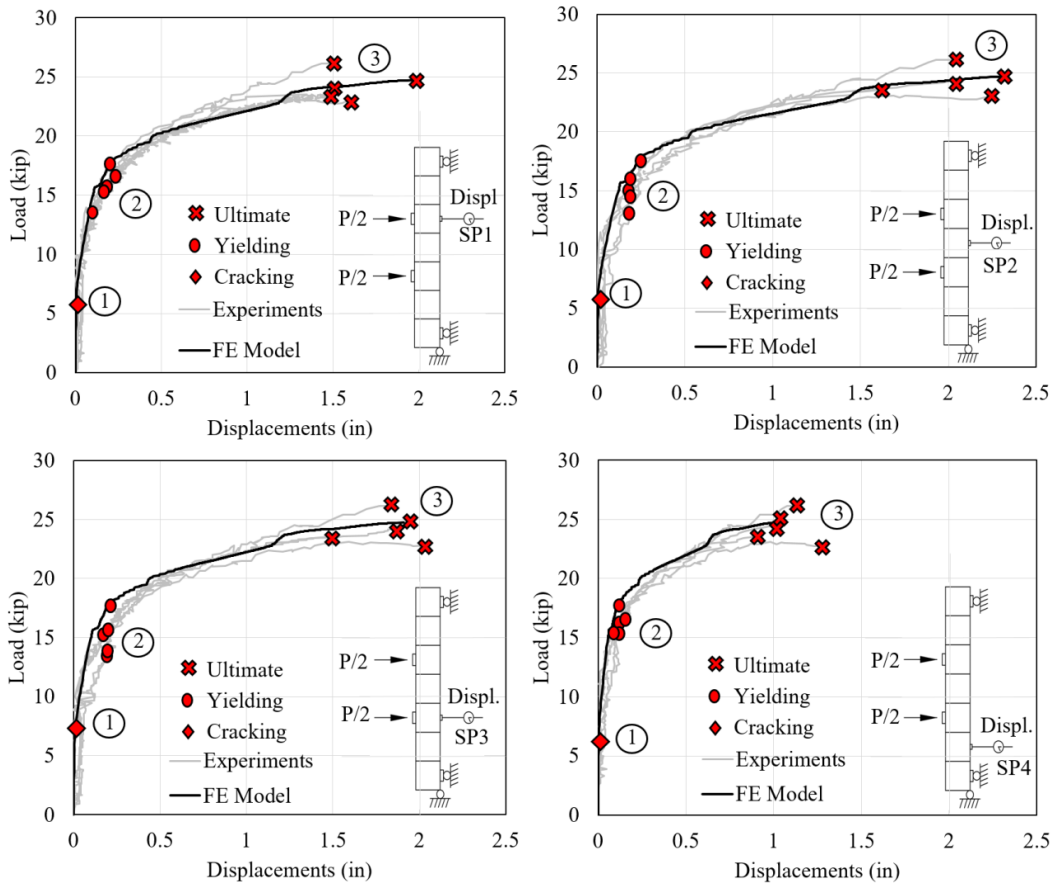

Fig. 4-12. Load-displacement behavior of experimental tests compared to FE model.

The first significant stage in the load-deflection curve is the initiation of cracking, indicated by the change in the slope of the initial tangent stiffness (Stage 1, indicated with a rhombus in Fig. 4-12). The second significant stage in this curve is the yielding behavior of the reinforcing bars (Stage 2, indicated with circles in Fig. 4-12). In the load-displacement curve predicted by the FE model, this transition stage can be found by tracking the stresses in the steel reinforcing bars as the lateral load increases. In the load-displacement curve measured during the experiments, this stage is harder to identify. Based on equivalent elasto-plastic yield approximation, Park (1988) proposed a method for

identifying the displacement at yielding as the intersection of the initial tangent stiffness and the tangent of the ultimate load (see Fig. 4-13). The third significant stage in the load-displacement curve is the ultimate load capacity of the wall (Stage 3, indicated with crosses in Fig. 4-12).

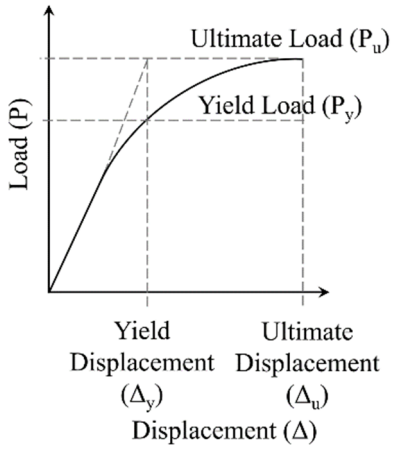

Fig. 4-13. Yield displacement based on equivalent elasto-plastic yield.

The reinforced dry-stacked concrete masonry walls can withstand lateral loads beyond the full elastic response as they exhibit displacement ductility. This displacement ductility (μ) can be calculated as the ratio between the ultimate displacement (at Stage 3 in Fig. 4-12) and the yield displacement (at Stage 2 in Fig. 4-12). The predicted displacement ductility is 8.39, which falls between the minimum (5.81) and maximum (15.25) displacement ductility observed during the experiments.

4.5 Parametric Analysis of Reinforced Dry-Stacked Masonry Walls

Section 4 demonstrated that the FE model developed herein can predict the behavior of the dry-stacked walls with an acceptable degree of accuracy with the experimental observations. In this section, the FE model is used to conduct a parametric

analysis to investigate the effect of the design parameters on the performance of dry-stack wall construction. The performance is evaluated in terms of the yield load (P_y) and the ultimate load (P_u), which are proportional to the internal compressive or tensile force of the section and the internal lever arm (see Fig. 4-14 (a)); and the yield displacement (Δ_y) and ultimate displacement (Δ_u), which are proportional to the yield load, ultimate load, modulus of elasticity, and moment of inertia of the section (see Fig. 4-14 (b)). The parametric analysis is conducted by varying one property at a time within practically plausible ranges while keeping all other properties at predefined nominal values. The properties under study are the unit compressive strength (nominal value, f_{unit}: 3,000 psi), the grout compressive strength (nominal value, f_{grout}: 5,000 psi), the yield strength of the reinforcing bars (nominal value, f_y: 60,000 psi), the reinforcement ratio (nominal value, ρ: 0.34%), and the percentage of grouting (nominal value, PG: 100%). The underlying assumption of this parametric analysis is that the fundamental mechanistic behavior of the walls remains unchanged when the selected design parameters are varied (Atamturktur and Laman 2012; Atamturktur et al. 2012b; Van Buren et al. 2014).

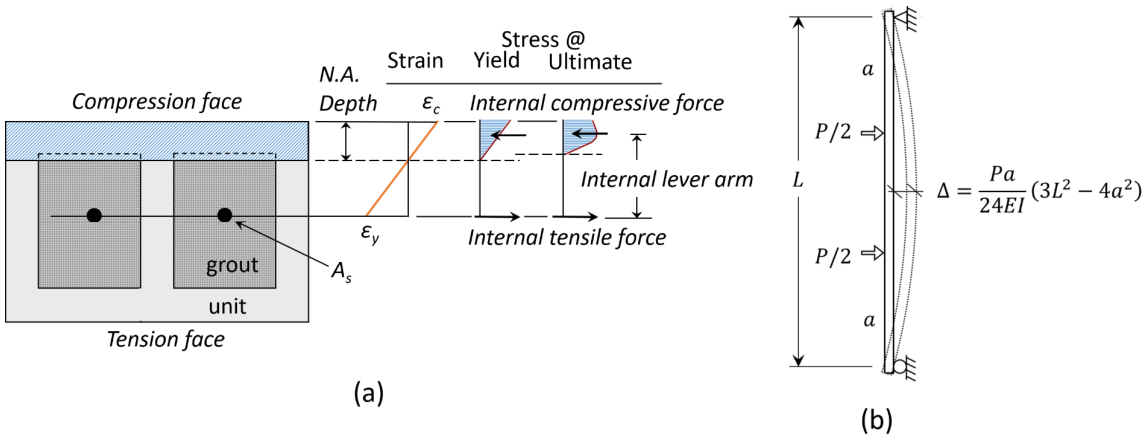

Fig. 4-14. (a) strains, stresses, and internal forces in the masonry wall cross-section and (b) wall mid-height displacement.

4.5.1 Effect of the Unit Compressive Strength

Load and displacement capacities of the fully grouted dry-stacked walls are predicted for varying unit compressive strengths (f_{unit}) of 2000, 3000, and 4000 psi. As seen in Fig. 4-15 (a), as the unit compressive strength increases from 2,000 to 4,000 psi, the yield load of the wall increases by approximately 2,200 lbs (14%) and the ultimate load increases by approximately 6,400 lbs (35%). These improvements in the wall's out-of-plane load capacity are expected, as increasing the unit compressive strength moves the neutral axis up towards the compression face of the wall. This in turn increases the internal lever arm and thus, the load-carrying capacity.

At the yield load, increasing the unit compressive strength from 2,000 to 4,000 psi decreases the yield displacement by 0.06 in. (22%) (Fig. 4-15 (b)). This can be explained by an increase in the unit modulus of elasticity (E_{unit}=900f_{unit} per MSJC 2013), which increases the wall stiffness for higher values of unit compressive strength. This effect, however, is countered by a slight reduction in the neutral axis depth, which leads to a

reduction in the moment of inertia of the section. At the ultimate load, increasing the unit compressive strength from 2,000 to 4,000 psi increases the ultimate displacement of the wall by 0.60 in. (120%) (Fig. 4-15 (b)). For walls with a higher unit compressive strength, the neutral axis moves up farther, and the cracked region of the cross-section becomes larger, which in turn reduces the moment of inertia of the section. Due to these changes in the yield and ultimate displacements, the displacement ductility increases from 2.0 to 5.7. In Fig. 4-15, these aforementioned relationships between the unit compressive strength and the lateral load (Fig. 4-15 (a)) as well as the mid-height displacement (Fig. 4-15 (b)) are approximated with a linear model. The ultimate and yield loads and displacements of the wall can be predicted though Eq. 4-1 to Eq. 4-4, respectively, where a valid domain for f'_{unit} is from 2,000 psi to 4,000 psi.

$$P_u = 3.20 f_{unit} + 12{,}390, \text{ with } R^2 = 0.96 \quad \text{Eq. 4-1}$$

$$P_y = 1.11 f_{unit} + 14{,}006, \text{ with } R^2 = 0.91 \quad \text{Eq. 4-2}$$

$$\Delta_u = 3(10)^{-4} f_{unit} + 0.14, \text{ with } R^2 = 0.96 \quad \text{Eq. 4-3}$$

$$\Delta_y = -3(10)^{-5} f_{unit} + 0.32, \text{ with } R^2 = 0.94 \quad \text{Eq. 4-4}$$

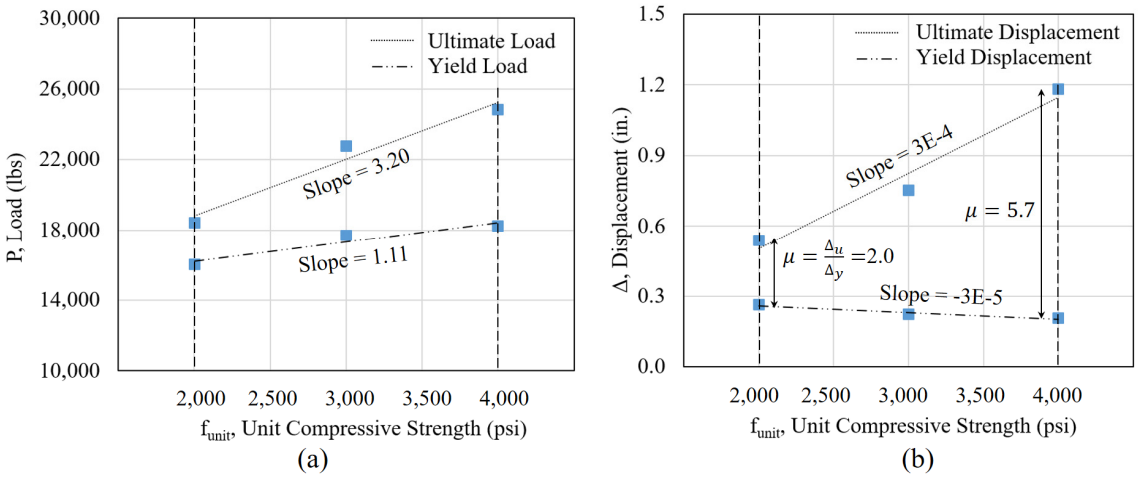

Fig. 4-15. Effect of unit compressive strength on the (a) load; (b) displacements on the masonry wall.

4.5.2 Effect of the Grout Compressive Strength

The effect of varying the grout compressive strength (f_{grout}) on the capacity of the dry-stacked masonry walls is evaluated by simulating the wall behavior for grout compressive strengths ranging from 4,000 to 7,000 psi in increments of 500 psi. Given this increase in grout compressive strength, the yield load of the wall increases by approximately 2,700 lbs (17%) and the ultimate load increases by approximately 4,500 lbs (22%). The improved wall capacity is due to the reduced neutral axis depth, which leads to an increase in the internal lever arm, increasing the section flexural capacity.

The same increase in the grout compressive strength leads to a reduction in the moment of inertia of the wall section, which occurs when the neutral axis moves up towards the compression face. This reduction is countered by a higher grout modulus of elasticity ($E_{grout}=500f_{grout}$ per ACI 318), which increases the wall stiffness, and as a result, the yield displacement of the wall decreases slightly by 0.02 in. (4%). On the other hand, the ultimate

displacement of the wall increases by approximately 0.60 in. (92%). This increase can be explained by the fact that for walls with a higher grout compressive strength, the neutral axis moves up farther towards the compression face of the wall, reducing the moment of inertia. This reduction, in turn, increases the cracked cross-sectional area and reduces the wall stiffness. Finally, these changes in the yield and ultimate displacements lead to an increase in the displacement ductility from 2.6 to 5.4. In Fig. 4-16, the relationships between the grout compressive strength and the lateral load (Fig. 4-16 (a)) as well as the mid-height displacement (Fig. 4-16 (b)) are represented with a linear model. The loads and displacements of the wall varying the grout compressive strength can be predicted though Eq. 4-5 to Eq. 4-8, respectively, where a valid domain for f_{grout} is from 4,000 psi to 7,000 psi.

$$P_u = 1.53 f_{grout} + 14{,}913, \text{ with } R^2 = 0.97 \quad \text{Eq. 4-5}$$

$$P_y = 0.82 f_{grout} + 13{,}287, \text{ with } R^2 = 0.90 \quad \text{Eq. 4-6}$$

$$\Delta_u = 1.6(10)^{-4} f_{grout} + 0.06, \text{ with } R^2 = 0.95 \quad \text{Eq. 4-7}$$

$$\Delta_y = -3(10)^{-6} f_{grout} + 0.22, \text{ with } R^2 = 0.97 \quad \text{Eq. 4-8}$$

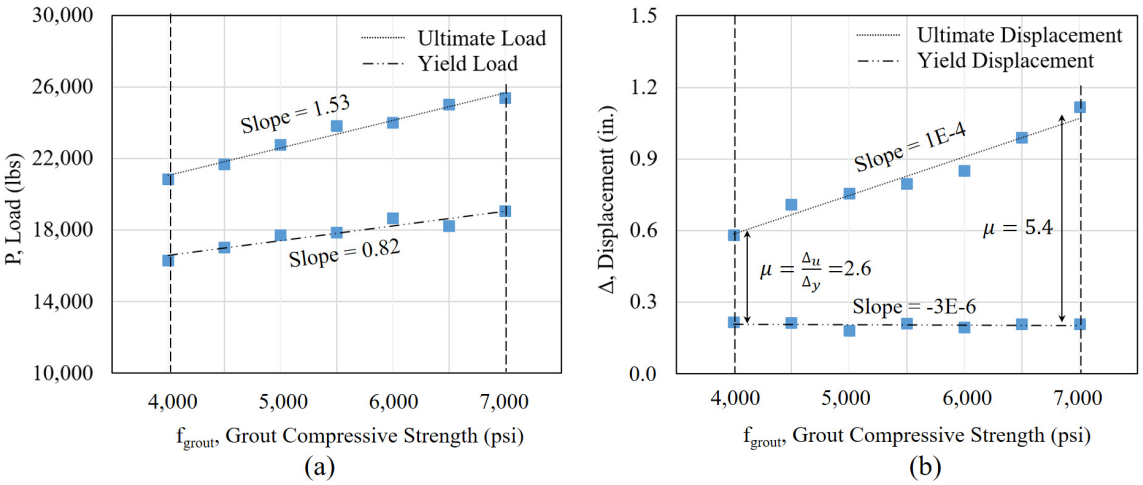

Fig. 4-16. Effect of grout compressive strength on the (a) load; (b) displacements on the masonry wall.

4.5.3 Effect of the Yield Strength of the Steel Reinforcing Bars

The effect of varying the yield strength (f_y) of steel reinforcement on the behavior of the dry-stacked masonry walls is investigated by varying f_y in the FE model simulations (in which the yield strain of steel reinforcement is also varied accordingly: $\varepsilon_y = f_y/E_s$). As the yield strength of the steel reinforcing bars is increased from 40,000 to 80,000 psi, the yield and ultimate load capacities of the wall are observed to increase by approximately 7,000 lbs (52%) and 2,200 lbs (10%), respectively. As the yield strength of the reinforcing bars increases, the neutral axis depth moves down towards the tension face and reduces the internal lever arm. This effect is countered by a considerable increase in the internal tensile force caused by the increased yield strength of the reinforcing bars, leading to an improvement in the load-carrying capacities.

Given the same increase in the yield strength, the wall mid-height displacement at yield load level increases by approximately 0.25 in. (194%). This increase can be explained

by a higher increase in the yield load for walls with a higher yield strength in the reinforcing bars; however, this effect is countered by a slight increase in the neutral axis depth, which increases the moment of inertia of the section. At the ultimate load, for walls with a higher yield strength in the reinforcing bars, the neutral axis depth further increases, which increases the moment of inertia of the section. This effect is countered by the increase in the ultimate load, and the ultimate displacement decreases by approximately 0.03 in. (5%). These changes in the yield and ultimate displacements, in turn, lead to a decrease in the displacement ductility ratio from 5.8 to 1.8. In Fig. 4-17, a linear model is used to approximate the dependencies of the lateral load (Fig. 4-17 (a)) and the mid-height displacement (Fig. 4-17 (b)) on the yield strength of the steel reinforcing bars. The loads and displacements of the wall varying the grout compressive strength can be predicted though Eq. 4-9 to Eq. 4-12, respectively, where a valid domain for f_y is from 40,000 psi to 80,000 psi.

$$P_u = 0.05f_y + 20{,}171, \text{ with } R^2 = 0.82 \quad \text{Eq. 4-9}$$

$$P_y = 0.18f_y + 6{,}709, \text{ with } R^2 = 0.99 \quad \text{Eq. 4-10}$$

$$\Delta_u = -9(10)^{-7}f_y + 0.81, \text{ with } R^2 = 0.67 \quad \text{Eq. 4-11}$$

$$\Delta_y = 6(10)^{-6}f_y + 0.13, \text{ with } R^2 = 0.96 \quad \text{Eq. 4-12}$$

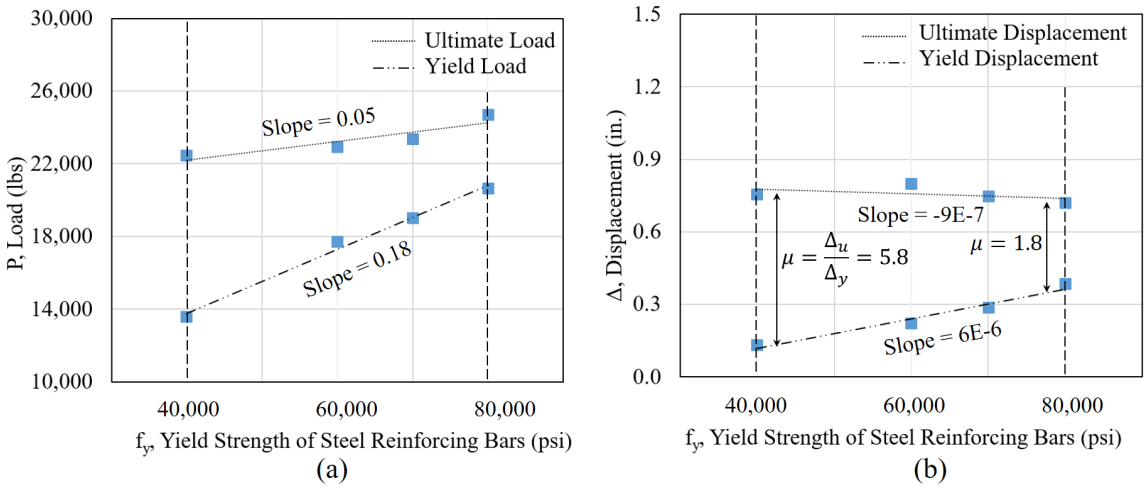

Fig. 4-17. Effect of yield strength of the steel reinforcement on the (a) load; (b) displacements on the masonry wall.

4.5.4 Effect of the Reinforcement Ratio

The effect of reinforcement ratio (ρ) is evaluated at values of 0.0034 (0.34%) and 0.0062 (0.62%) (corresponding to steel reinforcement No. 3 and No. 4 in each cell). The higher amount of steel reinforcement moves the neutral axis down towards the tensile face of the wall, reducing the internal lever arm, which has a negative effect on the load-carrying capacity of the wall. However, this effect is countered by a substantial increase in the internal tensile force of the section. As a result, when the reinforcement ratio increases from 0.0034 to 0.0062, the yield and ultimate loads increase by approximately 5,100 lbs (29%) and 2,300 lbs (10%), respectively.

The same increase in the reinforcement ratio causes the yield displacement to increase by 0.12 in. (66%). This increase can be explained by a large increase in the yield load for walls with a higher reinforcement ratio. This effect is countered by a slight increase in the neutral axis depth, which increases the moment of inertia of the section. For the

ultimate displacement, a decrease of approximately 0.18 in. (28%) is observed. For the walls with a higher steel content, an increase in the neutral axis depth increases the moment of inertia of the section, which reduces the mid-height displacement despite the increased ultimate load capacity. The combination of an increase in the yield displacement and a decrease in the ultimate displacement reduces the displacement ductility ratio from 4.4 to 1.9. Fig. 4-18 shows the relationship between the reinforcement ratio and the lateral load as well as the mid-height displacement.

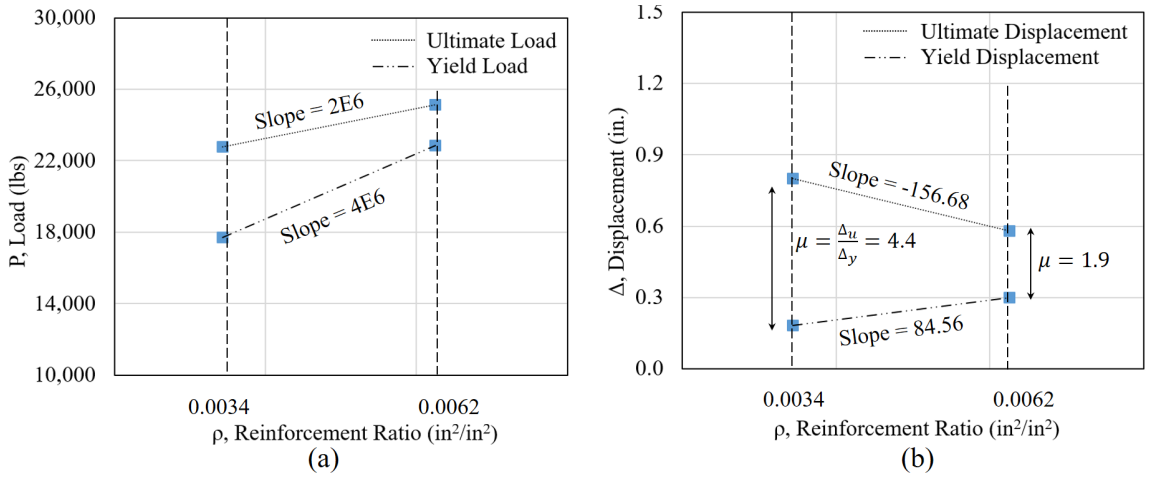

Fig. 4-18. Effect of reinforcement ratio for $0.0034 < \rho < 0.0062$: (a) yield and ultimate loads; (b) yield and ultimate displacements.

4.5.5 Effect of the Percentage of Grouting

The effect of the percentage of grouting (PG) is evaluated considering walls that are partially grouted (in every other cell, 0.5) and fully grouted (in all cells, 1.0). The steel content is kept the same in both walls; consequently, the reinforcement ratio is 0.0047 (0.47%) for the partially grouted wall and 0.0034 (0.34%) for the fully grouted wall. Fig. 4-19 shows the effect of the percentage of grouting on the lateral load and the mid-height

displacement. As the percentage of grouting increases from 50% (0.5) to 100% (1.0), the neutral axis depth moves down towards the tension face, which reduces the internal lever arm. In spite of this negative effect on the wall capacity, the additional compressive area due to the increase in grouting increases the yield load by approximately 4,200 lbs (31%) and the ultimate load by approximately 7,900 lbs (53%).

The same increase in the percentage of grouting causes a decrease in the mid-height displacement of the wall of approximately 0.02 in. (11%) at the yield load level. For walls with a higher percentage of grouting, the neutral axis depth increases, which leads to an increase in the moment of inertia of the section. This effect is somewhat countered by the increase in the yield load. At the ultimate stage, the neutral axis moves slightly down towards the tension face for walls with a higher percentage of grouting, which increases the moment of inertia of the section. This effect is countered by the increase in the ultimate load, which increases the ultimate displacement by approximately 0.36 in. (84%). As a result of the change in the yield and ultimate displacements, the displacement ductility ratio increases from 2.1 to 4.4.

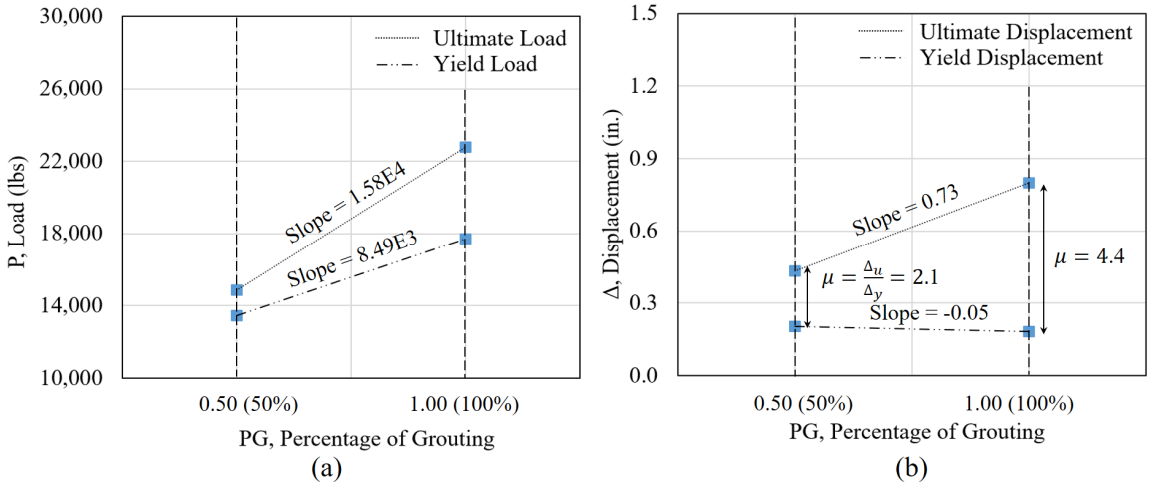

Fig. 4-19. Effect of percentage grouting for 0.5 < PG < 1.0: (a) yield and ultimate loads; (b) yield and ultimate displacements.

4.5.6 Summary of Results

Fig. 4-20 summarizes the results obtained from the parametric analysis discussed in previous section. Only the design parameters observed influencing the load and displacement capacities during the parametric analysis (refer back to Section 5) are considered. These parameters are the unit (f_{unit}) and grout (f_{grout}) compressive strengths, yield strength of the reinforcing bars (f_y), reinforcement ratio (ρ), and percentage of grouting (PG).

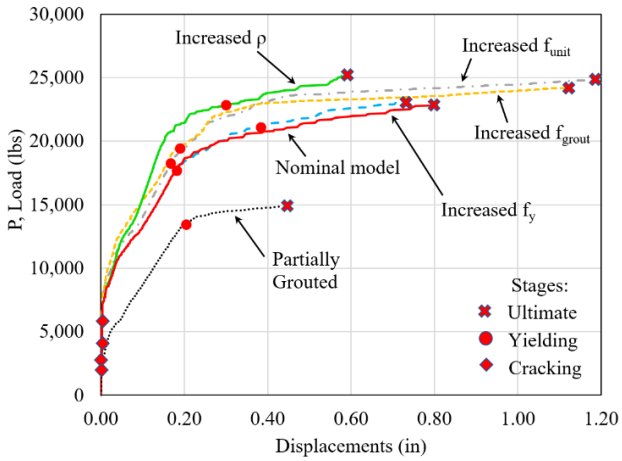

Fig. 4-20. Load-displacement plots of the nominal model, the partially grouted model, and the effects of increasing unit, grout compressive strength, yield strength, and reinforcement ratio.

4.6 Conclusions

This paper addresses the need for a better understanding of the behavior of dry-stacked concrete masonry walls under out-of-plane loading through a combined experimental and numerical study. The experimental study involved building and testing four dry-stacked reinforced concrete masonry walls in the laboratory. Along with the experimental investigation, a numerical model was built to analyze the dry-stacked wall in the same configuration and loading addressed experimentally. The capabilities of the numerical model have been demonstrated through a comparison of observed and predicted load-displacement curves. The FE model and experimental behavior showed a good agreement, supporting the view that the FE model developed in this study captured the behavior and the failure of dry-stacked masonry walls. Failure of dry-stacked masonry walls results from a local hinge-like rotation along a bed joint, which causes compression failure of the units on one side and tensile failure in the pure bending zone of the reinforced

dry-stacked wall. Using the experimentally validated models, the load and displacement capabilities at the yield and the ultimate stages are evaluated for varying unit and grout compressive strength, yield strength of the steel reinforcing bars, the reinforcement ratio, and the percentage of grouting to determine their influence on the wall behavior. Based on the parametric study, the following conclusions can be made for the dry-stacked wall configuration evaluated in this study:

- An increase from 2,000 to 4,000 psi in the unit compressive strength, and from 4,000 to 7,000 psi in the grout compressive strength improves the ultimate lateral load-carrying capacity by 35% and 22% of the dry-stacked wall, respectively. The displacement ductility of the wall increases 185% for the same increase in the unit compressive strength, and 107% for the same increase in the grout compressive strength.
- When the yield strength of the steel reinforcing bars increases from 40,000 to 80,000 psi, the ultimate load-carrying capacity increases by 10%, while the displacement ductility decreases by 69%.
- An increase from 0.0034 to 0.0062 in the reinforcement ratio causes the ultimate flexural capacity of the section to increase by 10%. However, the same increase in the reinforcement ratio also causes the displacement ductility of the wall to decrease by 57%.
- A change from partially grouted to fully grouted walls leads to a 53% improvement in the ultimate load-carrying capacity and increases the displacement ductility by 110%.

These findings demonstrate that dry-stacked masonry construction has a sufficient structural integrity to be incorporated in construction codes. To extend this research, in future studies, the numerical model presented in this paper can be applied to dry-stack masonry structures comprised of bonding agents, different unit geometries, and various combinations of loads to further our knowledge of these structures.

References

ACI Committee 318. (2015). *Building Code Requirements for Structural Concrete* (ACI 318-14): An ACI Standard: Commentary on Building Code Requirements for Structural Concrete (ACI 318R-14), an ACI Report. American Concrete Institute.

Anand, K.B. and Ramamurthy, K. (2000). "Development and Performance Evaluation of Interlocking-Block Masonry." *Journal of Architectural Engineering ASCE*, 6(2), 45-51.

Anand, K.B. and Ramamurthy, K. (2003). "Laboratory-Based Productivity Study on Alternative Masonry Systems." *Journal of Construction Engineering and Management ASCE*, 129(3), 237-424.

Angelillo, M, Cardamone, L., and Fortunato, A. (2010). "A Numerical Model for Masonry-Like Structures." *J. Mech. Mat. Struct.*, 5(4), 583-615.

Asare, A.K. (2015). "Finite Element Assessment of Precast Concrete Slab Using Ansys Structural." *M.S. thesis*, University of Ghana, Ghana.

Ashour, M.H. (2016). "Nonlinear Finite Element Analysis of RC Beams Strengthened with Steel Fiber-Reinforced Concrete Overlays." *Ph.D dissertation*, The Islamic University of Gaza, Gaza.

ASTM. (2010). "Standard Test Method for Young's Modulus, Tangent Modulus, and Chord Modulus." *ASTM E111-04*, West Conshohocken, PA.

ASTM. (2014). "Standard Test Methods for Sampling and Testing Concrete Masonry Units." *ASTM C140/C140M-14*, West Conshohocken, PA.

ASTM. (2016a). "Standard Test Method for Compressive Strength of Cylindrical Concrete Specimens." *ASTM C39-16*, West Conshohocken, PA.

ASTM. (2016b). "Standard Test Method for Sampling and Testing Grout." *ASTM C1019-16*, West Conshohocken, PA.

ASTM. (2016c). "Standard Specification for Loadbearing Concrete Masonry Units." *ASTM C90-16*, West Conshohocken, PA.

Atamturktur, S. (2009). "Verification and Validation under Uncertainty Applied to Finite Element Models of Historic Masonry Monuments." *Proceedings of the IMAC-XXVII*, Orlando, Florida, USA. February 9-12.

Atamturktur, S., and Laman, J. (2012). "Finite Element Model Correlation and Calibration of Historic Masonry Monuments: Review." *Struct. Design Tall Spec. Build*, 21(1), 96-113.

Atamturktur, S., Li, T., Ramage, M., and Farajpour, I. (2012a). "Load Carrying Capacity Assessment of a Scaled Masonry Dome: Simulations Validated with Non-Destructive and Destructive Measurements." *Construction and Building Materials*, 34(1), 418-429.

Atamturktur, S., Hemez, F., and Laman, J. (2012b). “Uncertainty Quantification in Model Verification and Validation as Applied to Large Scale Historic Masonry Monuments.” *Engineering Structures*, 43(1), 221-234.

Betti, M., and Galano, L. (2012). “Seismic Analysis of Historic Masonry Buildings: The Vicarious Palace in Pescia.” *Buildings*, 2(1), 63-82.

Biggs, D.T. (2002). “Development of a Mortarless Post-Tensioned Masonry Wall System.” *Proceedings of the Sixth International Masonry Conference*, 28-32.

Biggs D.T., and Forsberg, T.E. (2008). “A Mortarless Prestressed Masonry House: Case Study.” *Proceedings of the 14th International Brick and Block Masonry Conference,* Sydney, Australia, 1-11.

Chen, W. (1982). *Plasticity in Reinforced Concrete,* McGraw-Hill, NY.

Dahl, K. (1992). “A Failure Criterion of for Normal and High Strength Concrete.” *Rep. R. 286,* Depart. Struc. Engng, Technical Univ. of Denmark, Lyngby, Denmark.

De Castro, D.V. (2003). “Experimental and Numerical Analysis of Blocky Masonry Structures Under Cyclic Loading.” *Ph.D. thesis*, University do Minho, Portugal.

Drucker, D., Prager, W., and Greenberg, H. (1952). "Extended Limit Design Theorems for Continuous Media." *Quart. Appl. Math.*, 9(4), 381-389.

Drysdale, R.G., and Guo, P. (1995). “Strength Characteristics of Interlocking Dry-Stacked Concrete Block Masonry.” *Seventh Canadian Masonry Symposium*, Hamilton, Ontario, 160-171.

Elmezaini, N., and Ashour, M. (2015). “Nonlinear Analysis of Concrete Beams Strengthened with Steel Fiber-Reinforced Concrete Layer.” *J. Eng. Res. Tech.*, 2(3), 181-188.

Ferozkhan, M. (2005). “Development of a Dry-Stack Masonry System for Effective Resistance to Out-of-Plane Bending.” *M.S. thesis*, Central Queensland University, Australia.

Gabor, A., Ferrier, E., Jacquelin, E., and Hamelin, P. (2006). “Analysis and Modelling of the In-Plane Shear Behavior of Hollow Brick Masonry Panels.” *Construction and Building Materials*, 20(1), 308-321.

Glitza, H. (1991). “State-of-the-Art and Tendency of Development of Masonry without Mortar.” *Proceedings of the 9th International Brock/Block Masonry Conference in Berlin*, 2, 1028-1033.

Harris, H.G., Oh, K., and Hamid, A.A. (1992). “Development of New Interlocking and Mortarless Block Masonry Units for Efficient Building Systems.” *Proceedings of the 6th Canadian Masonry Symposium, Saskatoon,* 723-734.

Hatzinikolas, M., Elwi, A. E. and Lee, R. (1986). "Structural Behavior of an Interlocking Masonry Block." *4th Canadian Masonry Symposium*, Dept. of Civil Engineering, University of New Brunswick, Fredericton, Canada, 225-239.

Heiserman, D.L. (2015). “Concrete Masonry.” *Building Construction and Finishing*. Accessed 10 30, 2016. <http://free-ed.net/free-ed/Resources/Trades/carpentry/Building01/ ?iNum=0702>

Hemez, F.M. (2005). "Non-linear Error Ansatz Models for Solution Verification in Computational Physics." *Technical Report*, Los Alamos National Laboratory, Los Alamos, New Mexico. LA-UR-05-8228.

Hines, T. (1993). "Benefits of Drystack Interlocking Concrete Masonry as a Component of Cost Effective Construction." *Proceedings of the Sixth North American Masonry Conference*, Philadelphia, PA.

Kachlakev, D.I., Miller, T., Yim, S., Chansawat, K., and Potisuk, T. (2001). *Finite Element Modeling of Reinforced Concrete Structures Strengthened with FRP Laminates*, Final Report SPR 316, California Polytechnic State University, San Luis Obispo, CA and Oregon State University, Corvallis, OR for Oregon Department of Transportation.

Kamonna, H.H. (2010). "Nonlinear Analysis of Steel Fiber Reinforced Concrete Deep Beams by ANSYS." *Kufa Journal of Engineering*, 2(1), 109-124.

Klingner, R. (2010). *Masonry Structural Design.* McGraw-Hill Education, NY.

Köksal, H.O., Doran, B., Ozsoy, A.E., and Alacali, S., N. (2004). "Nonlinear Modeling of Concentrically Loaded Reinforced Blockwork Masonry Columns." *Can. J. Civ. Eng.*, 31(6), 1012-1023.

Köksal, H. O., Karakoc, C., and Yildirim, H. (2005). "Compression Behavior and Failure Mechanisms of Concrete Masonry Prisms." *Journal of Materials in Civil Engineering*, 17(1), 107-115.

Kwasniewski, L. (2013). "Application of Grid Convergence Index in FE Computation." *Bulletin of the Polish Academy of Sciences*, 61(1), 123-128.

Lohr, J.R. (1992). “Evaluation of “Formwall”: A Post-Tensioned Dry-Stacked Masonry System.” *M.S. thesis*, The Pennsylvania State University, PA.

Mahboubi, A., and Ajorloo, A. (2005). "Experimental Study of the Mechanical Behavior of Plastic Concrete in Triaxial Compression." *Cement and Concrete Research*, 35(1), 412-419.

Marzahn, G. (1997). "Dry-Stacked Masonry in Comparison with Mortar Jointed Masonry." *Liepzig Annual Civil Engineering Report 2,* 353-365.

Molnár, M., and Jönsson, J. (2012). “Bending Capacity of Dry-Stacked Lightweight Concrete Block Masonry.” *Proceedings of the 15th International Brick and Block Masonry Conference*, Florianópolis, Brazil.

MSJC, Masonry Standards Joint Committee. (2013). *Building Code Requirements and Specification for Masonry Structures and Related Commentaries,* TMS 602-11/ACI 530.1-11/ASCE 6-11, Boulder, CO.

Murray, E.B. (2007). “Dry-Stacked Surface Bonded Masonry – Structural Testing and Evaluation.” *M.S. thesis*, Brigham Young University, UT.

Ngowi, J.V. (2005). “Stability of Dry-Stack Masonry.” *Ph.D. thesis*, University of Witwatersrand, Johannesburg, South Africa.

Okail, H., Abdelrahman, A., Abdelkhalik, A., and Metwaly M. (2016). “Experimental and Analytical Investigation of the Lateral Load Response of Confined Masonry Walls.” *HBRC Journal,* 12(1), 33-46.

Park, R. (1988). "Ductility Evaluation from Laboratory and Analytical Testing." *Proceedings of 9th World Conference on Earthquake Engineering*, Auckland, New Zealand.

Pave, R.F. (2007). "Strength Evaluation of Dry-Stack Masonry." *M.S. thesis*, University of the Witwatersrand, Johannesburg, South Africa.

Ramadan, O.M., Abdelbaki, S.M., Saleh, A.M., and Alkhattabi, A.Y. (2009). "Modeling of Reinforced Concrete Beams with and without Opening by Using ANSYS." *Journal of Engineering Sciences*, 37(4), 845-858.

Roache, P.J. (2009). *Fundamentals of Verification and Validation*. Hermosa Publishers, NM.

Prabhu, S., Atamturktur, S., Brosnan, D., Dorrance, R., and Messier, P. (2014). "Foundation Settlement Analysis of Fort Sumter National Monument: Model Development and Predictive Assessment." *Engineering Structures (Elsevier),* 65(1), 1-12.

Safiee, N.A., Jaafar, M.S., Alwathaf, A.H., Noorzaei, J., and Abdulkadir, M.R. (2011). "Structural Behavior of Mortarless Interlocking Load Bearing Hollow Block Wall Panel under Out-of-Plane Loading." *Advances in Structural Engineering*, 14(6), 1185-1196.

Sayed-Ahmed, E.Y., and Shrive, N.G. (1996). "Nonlinear Finite-Element Model of Hollow Masonry." *J. Struct. Eng.*, 10.1061/(ASCE)0733-9445(1996)122:6(683), 683-690.

Schwer, L. (2008). "Is Your Mesh Refined Enough? Estimating Discretization Error Using GCI." *7th LS-DYNA Anwenderforum,* Bamberg, I-I-45-54.

Sekender, A., and Page, A. (1988). “Finite Element Model for Masonry Subjected to Concentrated Loads.” *J. Struct. Eng.*, 114(8), 1761-1784.

Sokairge, H., Rashad, A., and Elshafie, H. (2017). “Behavior of Post-Tensioned Dry-Stack Interlocking Masonry Walls under Out-of-Plane Loading.” *Construction and Building Materials*, 133(1), 348-357.

Tavárez, F.A. (2001). “Simulation of Behavior of Composite Grid Reinforced Concrete Beams Using Explicit Finite Element Methods.” *M.S. thesis*, University of Wisconsin – Madison, WI.

Thanoon, W.A., Jaafar, M.S., Kadir, M.R., Ali, A.A., Trikha, D.N., and Najm, A.M. (2004). “Development of an Innovative Interlockig Load Bearing Hollow Block System in Malaysia.” *Construction and Building Materials*, 18(1), 445-454.

Uzoegbo, H.C. (2001). “Lateral Loading Test on Dry Stack Interlocking Block Walls.” *Structural Engineering, Mechanics and Computation*, 1, 427-436.

Uzoegbo, H.C., and Ngowi, J.V. (2004). “Lateral Strength of Dry-Stack Wall System.” *Journal of the British Masonry Society*, 17(3).

Uzoegbo, H.C., Senthivel, R. and Ngowi, J.V. (2007). “Load Capacity of Dry-Stack Masonry Walls.” *The Masonry Society Journal*, 25, 41-52.

Van Buren, K., Atamturktur, S., and Hemez, F. (2014). “Model Selection through Robustness and Fidelity Criteria: Modeling the Dynamics of the CX-100 Wind Turbine Blade.” *Mechanical Systems and Signal Processing*, 43(1), 246-256.

Vargas, H.G. (1988), "Mortarless Masonry: The Mecano System", *International Journal for Housing Science and Its Applications*, 12(2), 145-157.

Wight, J.K., and MacGregor, J.G. (2011). *Reinforced Concrete: Mechanics and Design*. Prentice Hall, NJ.

Willam, K., and Warnke, E. (1974). "Constritutive Model for the Triaxial Behavior of Concrete." *Proc. Seminar on Concrete Structures Subjected to Triaxial Stresses,* Int. Association of Bridge and Structural Engineering, Zurich, Switzerland.

CHAPTER FIVE

THERMO-FLUID DYNAMIC ANALYSIS OF CONCRETE MASONRY UNITS VIA EXPERIMENTAL TESTING AND NUMERICAL MODELING

5.1 Introduction

The concrete masonry unit (CMU) is a widely-used construction material whose annual production is estimated at 4.3 billion units in the United States and Canada (Freedonia Group 2010; El-Hassan et al. 2013; Mahoutian et al. 2018). The thermal efficiency of CMUs is quantified in terms of the units' thermal resistance (R-value) (Al-Homoud 2005; Kosny and Christian 1995; Wati et al. 2017), where a higher R-value represents increased thermal efficiency caused by effective insulation properties (Ozel 2011). In the past, studies conducted on CMUs have used simplified methods of calculating R-values (e.g., series, parallel path, isothermal planes, zone methods) (Valore 1980; Van Geem 1986; Zmeureanu and Fazio 1988; Bilgen 2002; BIA 2016); however, these simplified methods have proven insufficient for representing the effect of complex three-dimensional air flow within the unit's molded interior space (also known as a cell) on the thermal performance of the CMU (del Coz Díaz et al. 2006, 2007, 2008; Li et al 2008b; Sun and Fang 2009; Henrique dos Santos et al. 2017). Different unit configurations (e.g., cell geometry, masonry material properties, the use of insulated materials) affect the air flow within the cells and thus influence the R-value of the unit. Taking the air flow into account in thermal analysis has the potential to improve the current state of knowledge regarding the thermal behavior of CMUs, and this increase in knowledge, in turn, could lead to significant improvements in the thermal performance. In this study, it has been

shown that an increase of 400% is achievable through the redesign of the unit geometry and insulation (Alhazmy 2010; NCMA TEK 6-2C 2013).

In the thermal analysis of CMUs, it is critical to consider not only air flow within the cells but also the three key mechanisms of heat transfer (i.e., conduction, convection, and radiation). For instance, changes in unit geometry may alter the paths of heat conduction through the unit (i.e., thermal bridges). In cases where the geometries of CMU cells are altered, the air flow within cells can increase or decrease the heat transported by convection through the air between the inner faces of the unit. Modifying the CMU by adding insulating materials or barriers within the cells affects heat radiation, as energy is emitted by electromagnetic waves or photons emanating from the inner faces of the cells (Incropera et al. 2006; Sanders and Brosnan 2010). Despite the importance of radiation in determining the thermal performance of CMUs, the established literature on the subject has primarily focused on the heat transfer mechanisms of conduction and convection (Alhazmy 2006; Mobedi 2008; Antar and Baig 2009; Alhazmy 2010). Only recently have studies conducted on the thermal behavior of CMUs begun to consider radiation in addition to conduction and convection (Sambou et al 2014; Ratanathavorn et al. 2015; Henrique dos Santos et al. 2017; Laaroussi et al. 2017). Because such studies are few and far between, the effects of different design parameters on the three mechanisms of heat transfer have not yet been fully understood. Such an understanding is essential for the design of new CMU configurations with improved thermal behavior.

In this paper, the authors perform a combined experimental and numerical study to investigate the effects of a variety of CMU design decisions (e.g., altering the unit geometry

and thus the thermal bridges of heat conduction) on the thermal efficiency of CMUs. Addressing the gaps in the pertinent literature, the present study considers the influence of air-filled cells on the thermal behavior of CMUs and takes all three heat transfer mechanisms of conduction, convection, and radiation into account. The study involves an experimental testing campaign in a hot-box, as well as the construction of detailed three-dimensional computational fluid dynamic models that are used to conduct thermo-fluid dynamics simulations. The authors recognize that both experimental tests and numerical simulations are important for gaining an improved understanding of the thermal behavior of CMUs. Simulations without experiments are speculative, and experiments without simulations are constrained within the scenarios tested (Atamturktur et al. 2012; Prabhu et al. 2014; Martínez et al. 2017; Stevens et al. 2016). In this study, experiments are conducted with the purpose of validating the simulations through rigorous test-analysis comparisons. The validated numerical models are then used to predict the thermal performance of untested CMUs and to explore different design configurations (see additional examples of using validated models in the evaluation of other construction materials: Wakili and Tanner 2003; Gu and Hunt 2007; Nayak et al. 2010; Zukowski and Haese 2010; Ratanathavorn et al. 2015).

This paper is organized as follows: Section 2 details the experimental and numerical research campaign. The description and development of the three-dimensional numerical models and thermo-fluid dynamics simulations are discussed in Section 3, as are the material properties (i.e., air density, air heat capacity, and thermal conductivity) of the CMUs and the details related to the model convergence study that is used to determine the

optimal mesh size. Section 4 describes the hot-box test of the CMUs in laboratory, and Section 5 covers the experimental validation of the CMU numerical models. In Section 6, the previously validated numerical models are used to predict the response of the CMUs for the different unit and insulation types investigated in the research campaign. Finally, Section 7 offers a discussion of the feasibility of using the new CMU configurations in the construction industry, while Section 8 contains concluding remarks and directions for future research.

5.2 Research Campaign

This study implemented a hierarchical research campaign that started from small-scale coupon testing and ended with a system-level evaluation of a CMU, as shown in Fig. 5-1. Material properties such as thermal conductivity and heat capacity were obtained through the laboratory tests on the small-scale coupons (Fig. 5-1-a) and were then used as input parameters while developing the numerical models of the units (Fig. 5-1-b). Next, tests were conducted on the units to assess the validity of the numerical models for predicting the thermo-fluid dynamic behavior of the CMUs (Fig. 5-1-c). The experimentally validated numerical models were then executed to evaluate various CMU configurations (Fig. 5-1-d) that altered (i) units' web configuration (and thus thermal bridging) for heat conduction and (ii) air movement within the units' cells for convective and radiative heat transfer.

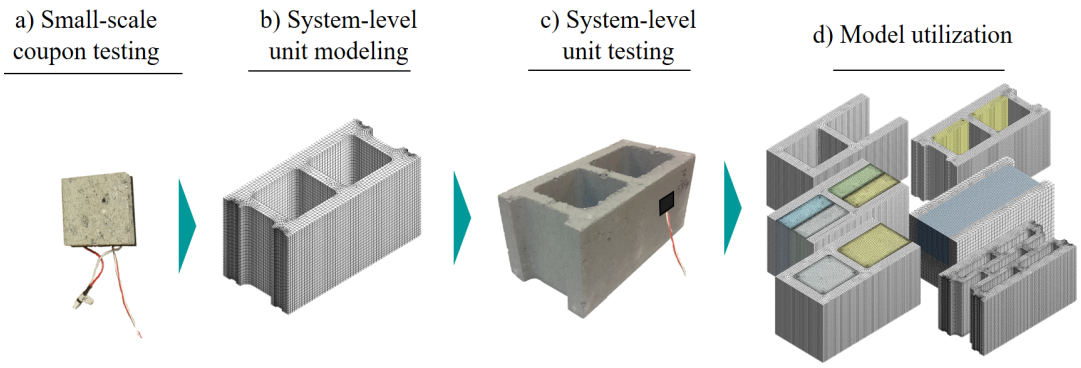

Fig. 5-1. Hierarchical process to study thermal performance of CMUs: a) small-scale coupons, b) numerical models of the units, c) experimental test of the units, and d) model utilization.

With the objective of gaining a better understanding of the effect of a variety of CMU design decisions on the thermal efficiency of CMUs, the authors evaluated 24 different CMU configurations with different unit and insulation types. "Unit type" will hereafter refer to the unit geometry of particular CMUs, while "insulation type" will refer to the type of insulation (or lack thereof) used in particular CMUs. When speaking of a particular unit type that has a particular insulation type, we will use the phrase "configuration type."

Below, Fig. 5-2 illustrates the different unit and insulation types used in this study. The four columns in the figure represent *different insulation types* in the CMU cells: Column A is the conventional hollow 8×8×16 CMU; Column B includes extruded cardboard; Column C includes rigid expanded polystyrene (EPS); and Column D includes injected foam insulation (polyurethane foam). The six rows in Fig. 5-2 represent the *different unit types*: Row 1 is a hollow unit; Row 2 is an A-shaped unit; Row 3 is a unit

with end shells and web of reduced height; Row 4 is an H-shaped unit; Row 5 is a multi-core unit with continous end shells; and Row 6 is a multi-core unit with discontinous end shells. For four of the 24 configuration types (Row 1, from A1 to D1), the numerical models were validated against laboratory experiments, and the remaining 20 configuration types were predicted using the validated numerical models.

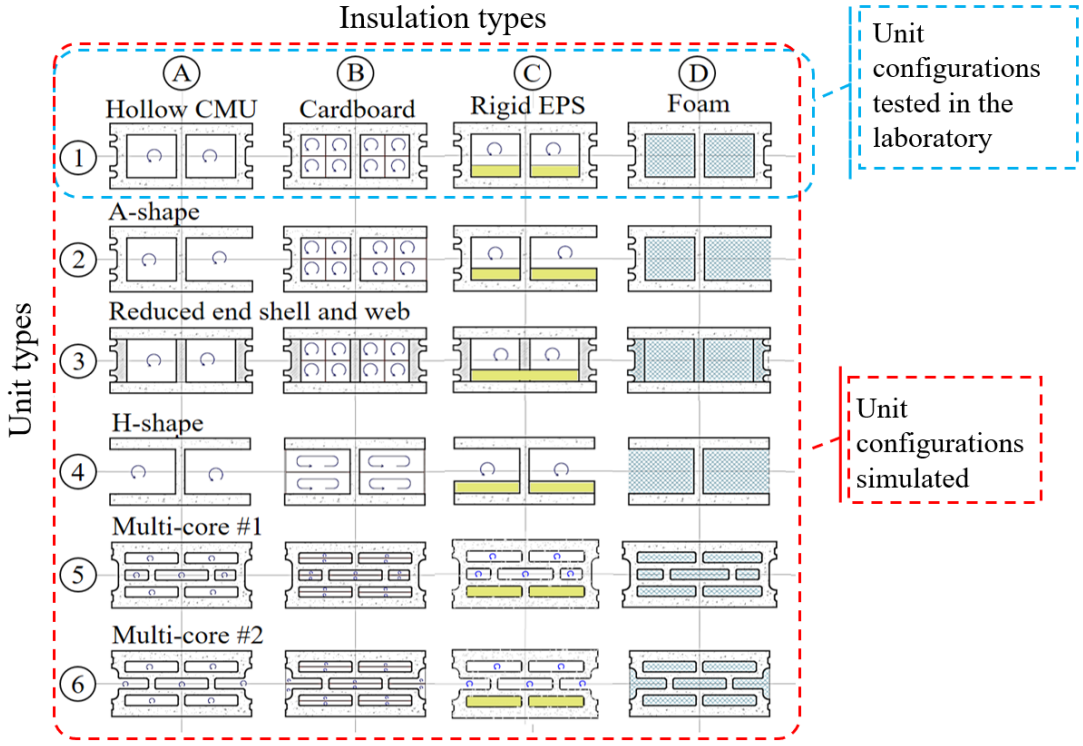

Fig. 5-2. CMU insulation types and unit types investigated in this study. The horizontal rows represent different unit types (e.g., 1-6), while the vertical columns represent different insulation types (i.e., different insulation material) (e.g., A-D). Configuration types are composed of a particular unit type and a particular insulation type (e.g., A1-D6)

The research campaign shown in Fig. 5-2 allowed for a comparison between the thermal performance of the conventional hollow CMU and the thermal performance of

units with different unit types (e.g., alternative webs and end shells) and different insulation types (i.e., different types of insulation material). In this comparison, thermal efficiency was quantified using the R-value of the units, including all three heat transfer mechanisms as well as the flow field within the cell. To evaluate the effect of unit density on R-values, two units with different densities—a normal-weight (2,074 kg/m^3) and a medium-weight (1,682 kg/m^3), according to ASTM C90 (ASTM 2016)—were investigated (see Fig. 5-3).

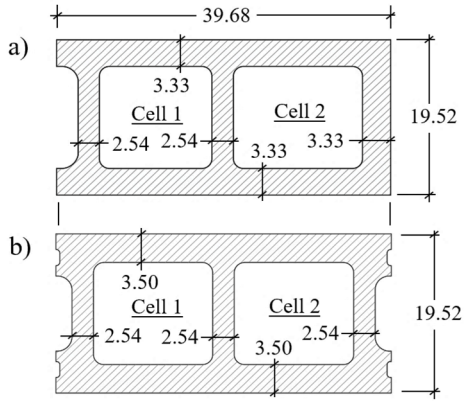

Fig. 5-3. The geometry of a) the normal-weight and b) the medium-weight CMUs (dimensions in cm).

5.3 Numerical Simulation

The presence of air flow within a unit's cells and the temperature gradient across the depth of a CMU activate all three mechanisms of heat transfer through the concrete material and the air within the unit; for this reason, it is necessary to consider the thermo-fluid dynamic (TFD) behavior of the CMUs (Li et al. 2008a; Sun and Fang 2009; Henrique dos Santos et al. 2017; Laaroussi et al. 2017). Accordingly, TFD simulations were conducted to calculate the R-value for the configuration types shown in Fig. 5-2. The Finite Volume Method was employed to solve the three kinds of governing equations of fluid

dynamics and thermal analysis: namely, (i) the Navier-Stokes equations, which represent conservation of momentum; (ii) continuity equations, which represent the conservation of mass; and (iii) the first law of thermodynamics equations, which represent the conservation of energy. These equations are nonlinear partial differential equations that were discretized into a system of algebraic equations and solved in ANSYS Fluent v18.2. To be a tractable problem, Ansys Fluent's pressured-based solver used an algebraic multi-grid approach to solve these equations in an iterative manner, where the air temperature and velocity change from iteration to iteration, reaching steady-state condition when these model outputs have negligebible residuals (Webster 1994; Pletcher et al. 2012).

5.3.1 Model Description

The authors developed three-dimensional numerical models to evaluate the R-values of the 24 configuration types shown earlier in Fig. 5-2. For each of these 24 types, two different numerical models were developed that reproduced the geometrical properties of both the normal- and medium-weight CMUs (recall Fig. 5-3).

The models were analyzed in the presence of a temperature gradient until steady-state conditions were reached. The numerical models were developed using mixed convective and radiative boundary conditions to simulate the external environment. Three user-defined input parameters were employed: (1) free stream temperatures, (2) external emissivity, and (3) heat transfer coefficients. The free stream temperatures (T_{hot}=312.15 K and T_{cold}=282.15 K) were the temperatures of the hot and cold air in contact with the face shell of the CMU (see Fig. 5-4). To represent the emissivity, radiative transfer equations were solved through the Discrete Ordinate model within ANSYS Fluent. The typical values

for external emissivity are between 0 (an ideal mirror, as all incoming radiation is reflected and no radiation is emitted) and 1 (a black body in which all incoming radiation is absorbed). However, according to existing literature, emissivity of masonry surfaces ranges between 0.85 and 0.95 (Zhao and Tao 1995; Li et al. 2008b; Sun and Fang 2009; Antar 2010; Henrique dos Santos et al. 2017). A recommended value of external emissivity ε_{ext} equal to 0.94 was used in this study [43]. The film coefficients were calculated using the ratio between the amount of heat transferred (i.e., heat flux) and the difference in temperature between the surface of the CMU and the surrounding temperature during the experiments. In this study, in configuration type A1, the film coefficients were h_{hot}=22.4 W/m^2-K and h_{cold}=28 W/m^2-K for normal-weight CMUs and h_{hot}=19 W/m^2-K and h_{cold}=32.4 W/m^2-K for medium-weight CMUs. In configuration type D1, expected to have the highest thermal resistance, the film coefficients were h_{hot}=23.2 W/m^2-K and h_{cold}=28.9 W/m^2-K for normal-weight CMUs and h_{hot}=20.7 W/m^2-K and h_{cold}=30.1 W/m^2-K for medium-weight CMUs. Finally, adiabatic boundaries were applied to both the outer surface of the end shells and the top and bottom surfaces of the CMUs to avoid heat transfer gain and/or loss.

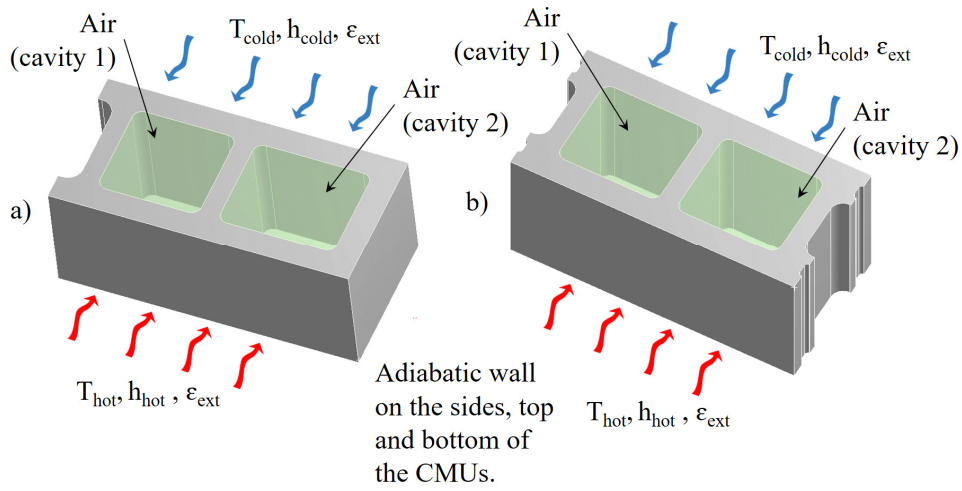

Fig. 5-4. Geometry and boundary conditions of the TFD models for a) normal-weight CMU and b) medium-weight CMU.

The governing equations in fluid dynamics and thermal analysis are not only nonlinear but also coupled to one another. In ANSYS Fluent, partial differential equations were numerically solved by adapting an available pressure-based solver; using a pressure equation within the adapted solver, the authors were able to achieve the constraint of the mass conservation (i.e., continuity equations) of the CMU's velocity field. The pressure equation was derived from the continuity and momentum equations in a such way that the velocity field, corrected by the pressure, satisfied the continuity.

5.3.2 Material Properties

The thermo-physical properties of the air in the cells of CMUs are temperature-dependent. In this study, the air density within cells was calculated using the ideal gas law for an incompressible fluid (velocities lower than 0.3 Mach), while the air heat capacity and the thermal conductivity were computed using the kinetic theory of gases. The regime

of the flow through the cells was assumed to be laminar (in Section 5, this assumption is checked).

Five material coupons—namely, normal- and medium-weight traditional concrete masonry material, extruded cardboard, injected foam, and rigid EPS—were obtained and cut into 5 cm × 5 cm sections. Three samples of each material coupon were tested for a total of 15 tests. Different thicknesses were then tested in a guarded setup, as shown in Fig. 5-5. The properties of the material coupons were measured until the heat flow and surface temperatures reached constant values (i.e., steady-state conditions). All material coupon tests were then carried out in a modified hot-box apparatus. The apparatus was similar to that in ASTM C1363-11 (ASTM 2011); meanwhile, the overall procedure was similar to that described in Smith (2016) and Huygen and Sanders (2017). The procedure involved exposing the two faces of the coupons to two different temperatures (282.15 and 312.15 K) and measuring the thermal conductivity and heat capacity of the coupons.

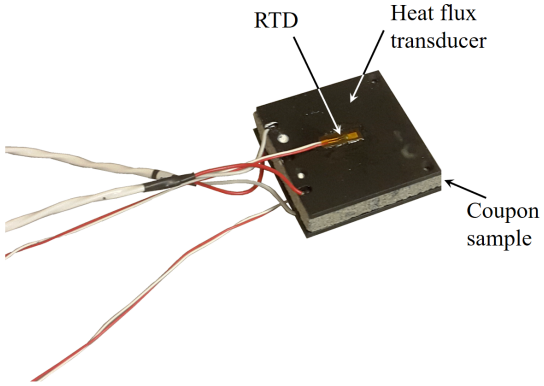

Fig. 5-5. Coupon sample in guarded testing setup.

In line with ASTM E1137 (ASTM 2014), the heat flow in the coupons was measured through heat flux transducers, and the temperature was measured by 1000-ohm

platinum resistance temperature detectors. The test setup is shown later in Fig. 5-9. The measured R-values (R_{mea}) were calculated using Eq. 5-1,

$$R_{mea} = {}^{\Delta T}/_{\bar{q}} \qquad \text{Eq. 5-1}$$

where ΔT is the measured gradient of temperature [K] between the hot and cold surfaces of the coupon and $\bar{q}$ is the measured average heat flux [W/m^2] between the hot and cold surfaces of the coupon.

Some roughness is always present on the coupon surface; as a result, contact spots were interspersed with gaps that in most instances were air-filled (Lienhard IV and Lienhard V 2003). As a result of these gaps, heat transfer could be attributed partly to conduction across the contact area and partly to convection and/or radiation across the gaps (Incropera et al. 2006). This phenomenon is known as *thermal contact resistance*. In tests where the R-value is small relative to the thermal contact resistance, as is the case with the materials discussed in this study, the effect thermal contact resistance must be considered (Tleoubaev and Brzezinski 2008).

Thermal contact resistance has been discussed in detail in which the methods for correcting the R_{mea} were developed for different materials (Ducharme et al. 1990; Zarr and Pintar 2012; Plaskolite 2017; Quadrant Plastics 2017; Huygen et al. 2017). Following these earlier studies, we corrected our coupon measurements to account for the thermal contact resistance between the surface of the sensors (i.e., the heat flux transducers and resistance temperature detectors) and the material coupon surface. We corrected the measured R-

value (R_{mea}) using Eq. 2 and obtained the corrected the R-value (R_{cor}) (Peirce and Willson 1990; Incropera et al 2006).

$$R_{cor} = 1.1909R_{mea} - 0.0263 \quad \text{(Eq. 2)}$$

Using the corrected R-value, the corrected thermal conductivity was calculated using Eq. 3,

$$k_{cor} = {}^{d}/_{R_{cor}} \quad \text{(Eq. 3)}$$

where k is expressed in [W/m-K], d represents the thickness of the coupon [m], and R_{cor} is expressed in [m^2K/W]. Finally, the heat capacity (C_p)—that is, the amount of energy released or gained by the sample as a result of temperature change—was obtained by integrating as a function of time the difference in heat flux between the amount of energy that entered the sample and the amount of energy that left it. The relevant equation (Eq. 4) is as follows:

$$C_p = \frac{2}{\rho l \Delta T_{air}} \int_0^t [\bar{q}_{hot}(t) - \bar{q}_{cold}(t)]dt \quad \text{Eq. 5-4}$$

where ρ represents the density of the unit [kg/m^3], ΔT_{air} represents the temperature difference in the air applied [K], and $\bar{q}_{hot}$ and $\bar{q}_{cold}$ represent the measured heat flux in the outer face shell of the unit [W/m^2]. The averaged values for the material properties obtained from the experiments are given in Table 5-1.

Table 5-1. Material properties obtained by coupon testing.

Material	k_{cor} [W/m-K]	C_p [J/kg-K]	ρ [kg/m^3]
Coupon #1	1.7250±0.1210	868	2,074
Coupon #2	0.8890±0.0160	748	1,682
Extruded Cardboard	0.046±0.00035	1,300	130
Injected Foam	0.038±0.00022	1,470	8.8
Rigid EPS	0.0377 @ 291.6K 0.0393 @ 302.3 K 0.0417 @ 314.7 K	1,645	14

5.3.3 Model Convergence

The solution process used in this study requires two convergence conditions to be satisfied: iteration convergence and mesh convergence. The former condition is internally enforced and satisifed in ANSYS Fluent v.18.2 during the simulation when the residuals of the computed output response consistently stay under a predefined threshold (10^{-3} in this study) in each iteration; meanwhile, the latter condition is satisfied manually when the solution exhibits negligable change during the refinement of the mesh (Durbin and Medic 2007; Almohammadi et al. 2013). In a thermo-fluid dynamics simulation, the mesh density must be appropriately determined so that the key features of the flow field and the heat transfer are incorporated without incurring additional and unnecessary computational expense. Furthermore, the numerical model must have a sufficiently refined mesh (also known as a mesh-independent solution) in order to produce a reliable prediction with negligible discretization errors (Roache et al. 2009; Atamturktur et al. 2012; Mollineaux et al. 2013). A mesh-independent solution can be found by monitoring model output (i.e., temperature, air velocity, and heat flux) for simulations with different mesh sizes. This process allows for the identification of stable values for model output (Karimi et al. 2012).

The Grid Convergence Index (GCI) provides an approach for estimating discretization errors (Roache 1994; Mollineaux et al. 2013; Martínez and Atamturktur 2017). To calculate GCI, a minimum of three obtained solutions with varying mesh sizes are required (Stern et al. 2001). In this study, models with a fine mesh (Δ_F=0.5 cm), a medium mesh (Δ_M=1.0 cm), and a coarse mesh (Δ_C=2.0 cm) were generated, and the predictions obtained with these three models were used to estimate the exact-but-unknown reference solution, y^{ref}, through Richardson's extrapolation (Richardson and Gaunt 1927). The reference solution represents the model predictions as if the calculation were to be run at Δ_{ref}=0. The Richardson's extrapolation, neglecting higher-order terms, is represented mathematically by Eq. 5.

$$y^{ref} = y(\Delta_F) + \frac{y(\Delta_F) - y(\Delta_M)}{r^p - 1} \qquad \text{Eq. 5-5}$$

In Equation 5, r is the grid refinement ratio that defines the ratio between successive average mesh sizes (in this study, r=2, which means that the average mesh size is halved in each of the dimensions represented in the solution domain), and p is the observed order of accuracy of the algorithm, which is unitless. The mesh refinement study for this research was conducted in the numerical model at three different locations of the CMU, as can be seen in Fig. 5-6. The area-weighted average temperature was obtained on the hot face of the CMU's face shell (location P1); the temperature was obtained in the center of cell 1 (location P2); and the volume-weighted average velocity of the air was obtained in cell 2 (location P3). The difference between the exact-but-unknown solution and the solutions at mesh size Δx (i.e., the solution error) can be seen in Fig. 5-7 on a log-log scale, where the

slope confirms that the observed solution closely matched with the second order of accuracy (i.e., p^{theory}=2).

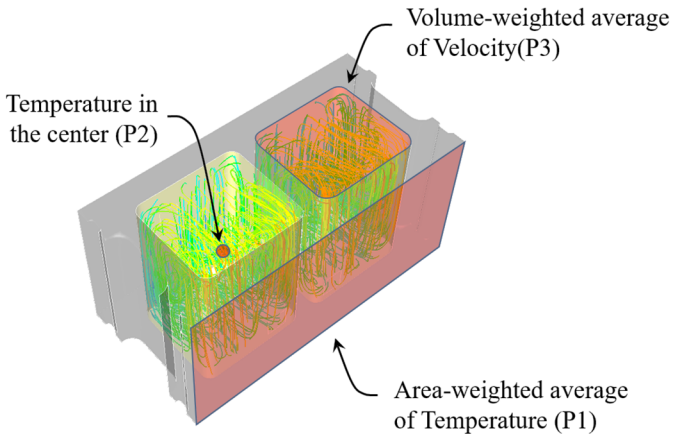

Fig. 5-6. Monitored locations to determine the GCI of different mesh sizes.

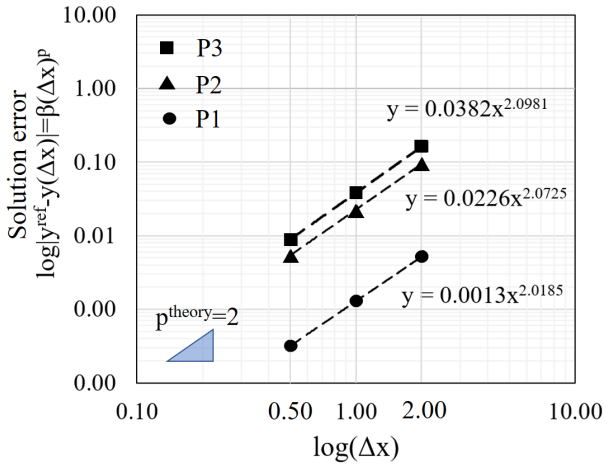

Fig. 5-7. Asymptotic convergence of variables in location P1, P2, and P3 as a function of mesh resolution.

The GCI for fine-medium and medium-coarse mesh is defined in Eq. 6,

$$GCI = \frac{1.25\varepsilon}{r^p - 1} x100\% \qquad \text{Eq. 5-6}$$

where ε is the relative difference between the predictions of models for which meshes have been subsequently redefined. Table 5-2 lists the results obtained when using fine-medium and medium-coarse meshes. The highest discretization errors were recorded at location P3, which had a $GCI_{F\text{-}M}$ of 0.33% and a $GCI_{M\text{-}C}$ of 1.45%. The ratio $GCI_{M\text{-}C}/(r^p GCI_{F\text{-}M})$ was observed to be approximately 1, which confirmed an asymptotic behavior in the solution. Therefore, a fine mesh of 0.5 cm was deemed to provide an acceptable level of discretization error.

Table 5-2. Results of the Grid Convergence Index.

Location	$GCI_{F\text{-}M}$ (%)	$GCI_{M\text{-}C}$ (%)	p	$GCI_{M\text{-}C}/r^p GCI_{F\text{-}M}$
P3	0.33	1.45	2.09	1.01
P2	2.3E-3	9.5E-3	2.07	1.00
P1	1E-4	5E-4	2.01	0.99

5.4 Hot-Box Tests on Concrete Masonry Units

The heat transfer capabilities of four configuration types, A1, B1, C1, and D1 (recall Fig. 5-2), were tested under steady-state conditions using a modified hot-box. The modified hot-box was designed to use convective heat transfer and consisted of two insulated chambers (80 cm × 80 cm) made of extruded polystyrene foam board with a thickness of 10 cm. To measure the thermal properties of the CMUs, one of the chambers was set to be hot, and the other was set to be cold, as shown in Fig. 5-8. Each test was repeated three times.

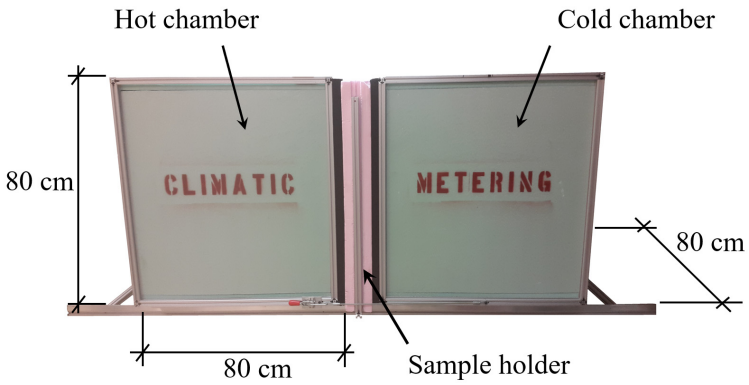

Fig. 5-8. Lateral view of the modified hot-box experimental setup.

During testing, the chambers were clamped tightly against an insulated frame that surrounded the sample holder (see Fig. 5-9). To obtain the desired temperatures of 312.15 K (39 °C) in the hot chamber and 282.15 K (9 °C) in the cold chamber, the air in each chamber was thermally controlled using a Laird 250-watt thermoelectric assembly. This assembly has fans on both sides of the chambers that transfer heat to the surrounding atmosphere. The fans were controlled by a PR-59 Regulator, which was used to alter the fan voltages between 12V (minimum power) and 24V (maximum power). To mimic natural convective patterns, baffles were set up to create a laminar air flow that directed air down the face shell of the CMU on both the cold and hot sides. The baffles fit the inside of the chamber with dimensions of 60 cm × 60 cm × 2.5 cm. To monitor the velocity and temperature in the air outlets, thermistors were installed in the mid-upper part of each baffle.

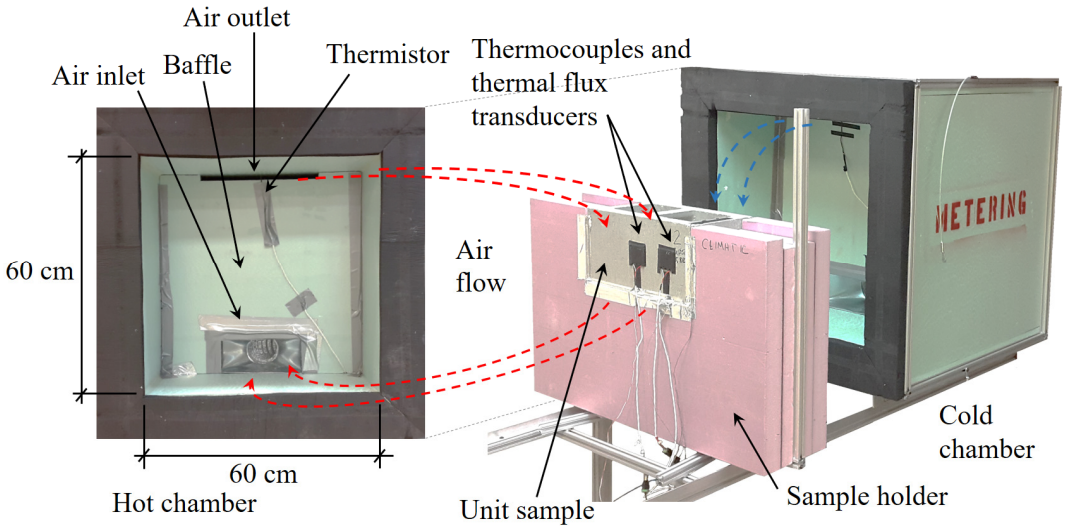

Fig. 5-9. Experimental setup of a CMU in the modified hot-box.

Within both the cold and hot chambers, instrumentation was used to monitor air and surface temperatures inside and outside of the CMU. ASTM E230 (ASTM 2012) specifies that Type T Thermocouples are suitable to measure temperatures in these types of tests. Three thermocouples (T3, T4, and T5) were thus placed in the air space in cell 2, and six thermocouples (T0, T1, T2, T6, T7, and T8) were distributed on cell 2's outer and inner face shells, as shown in Fig. 5-10.

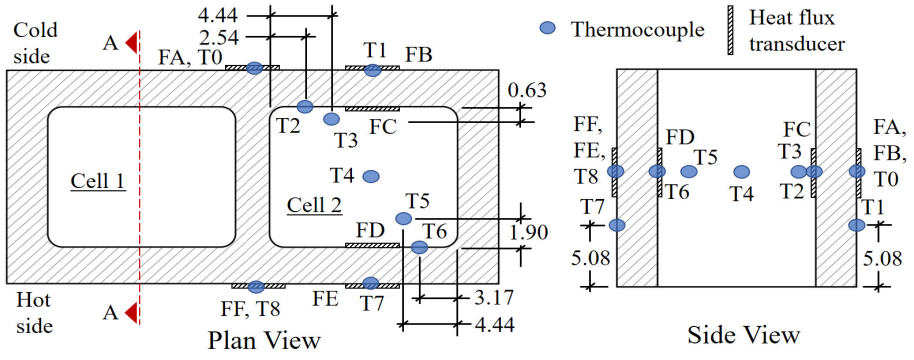

Fig. 5-10. Location of instrumentation in the CMU during testing (dimensions in cm).

Temperature measurements collected by the thermocouples were supplemented with six heat flux transducers (FA, FB, FC, FD, FE, and FF) to monitor heat flux through the CMU. The heat flux transducers, which were made of polyimide, were 5 cm × 5 cm × 0.32 cm and were distributed as shown in Fig. 5-10. The measured R-values for the CMUs were defined as the ratio of the surface average temperature gradient (T0, T1, T7, and T8) to the average heat flux between the cold and hot faces of the CMU (FA, FB, FE, and FF) (recall Eq. 5-1). As discussed in Section 3.2, the R_{mea} was corrected using Eq. 5-4 as a means of taking the contact thermal resistance into account. Table 5-3 shows the measured and corrected R-values (R_{cor}) for configuration types A1 to D1 at both normal and medium CMU weights. These results were used to validate the numerical models.

Table 5-3. Measured and corrected R-values for the normal- and medium-weight CMUs on configuration types A1 to D1.

Density	CT	R_{mea} [m^2K/W]	R_{cor} [m^2K/W]
Normal-weight	A1	0.188	0.198
	B1	0.253	0.275
	C1	0.296	0.326
	D1	0.372	0.417
Medium-weight	A1	0.260	0.284
	B1	0.369	0.413
	C1	0.415	0.468
	D1	0.617	0.708

5.5 Experimental Validation of the Thermo-Fluid Dynamics Simulation

In Section 4, two types of data were collected through the modified hot-box tests: (i) air temperature within one of the cells (cell 2) of each CMU and (ii) R_{cor} of each CMU.

These experimental measurements were subsequently used to assess the predictive abilities of the thermo-fluid dynamics simulations that were discussed in Section 3.

Air temperature in cell 2. For configuration types A1, B1, and C1, the temperatures obtained at the location of thermocouples T3, T4, and T5 (recall Fig. 5-10) are shown for the normal-weight unit in Table 5-4 and for the medium-weight unit in Table 5-5. For configuration type D1, the air temperature in the CMU cells was indeterminable, as the cells were filled with insulated material and had no flow field.

Table 5-4 and Table 5-5 distinguish cases where the temperatures predicted by the thermo-fluid dynamics simulations were inside or outside the range of experimentally measured minimum and maximum temperatures. Instances where the predictions were not in this experimental range could perhaps be explained by potential, slight variations in the location of sensors between each run.

Table 5-4. Comparison of experimental and TFD simulation air temperature measurements for normal-weight CMUs.

		Experiments		TFD				Experiments		TFD	
CT	No.	Temp. [K]		Temp. [K]	Within Range	CT	No.	Temp [K]		Temp. [K]	Within Range
		Min.	Max.					Min.	Max.		
	T5	300.78	300.98	300.12	No		T5	303.24	303.44	303.83	No
A1	T4	297.34	297.54	297.42	Yes	B1	T4	293.01	293.21	292.78	No
	T3	291.84	292.04	292.61	No		T3	289.78	289.98	289.92	Yes
	T5	293.69	293.89	293.98	No		T5	-	-	-	N/A
C1	T4	293.20	293.40	293.92	No	D1	T4	-	-	-	N/A
	T3	289.81	290.01	289.96	Yes		T3	-	-	-	N/A

CT: Configuration type, N/A: Not applicable

Table 5-5. Comparison of experimental and TFD simulation air temperature measurements for medium-weight CMUs.

		Experiments		TFD				Experiments		TFD	
CT	No.	Temp. [K]		Temp. [K]	Within Range	CT	No.	Temp. [K]		Temp. [K]	Within Range
		Min.	Max.					Min.	Max.		
	T5	297.55	297.75	297.38	No		T5	303.30	303.50	303.39	Yes
A1	T4	297.47	297.67	297.49	Yes	B1	T4	292.49	292.69	291.23	No
	T3	292.59	292.79	292.60	Yes		T3	288.90	289.10	289.02	Yes
	T5	292.94	293.14	293.01	Yes		T5	-	-	-	N/A
C1	T4	291.97	292.17	292.32	No	D1	T4	-	-	-	N/A
	T3	288.83	289.03	288.86	Yes		T3	-	-	-	N/A

CT: Configuration type, N/A: Not applicable

The air flow within the cells in configuration types A1, B1, and C1 contributed to the heat transfer and had to be accounted for. The representative temperature field (i.e., isotherms) in a mid-section cut (see A-A in Fig. 5-10) of a CMU cell is shown in Fig. 5-11. The figure shows that the air within a cell is driven by buoyancy. The inner hot face heats the air on the surface, and the air moves upward because of the decrease in air density. In

contrast, the inner cold face cools the air on the surface, and the air moves downward because of the increase in air density (Sun and Fang 2009).

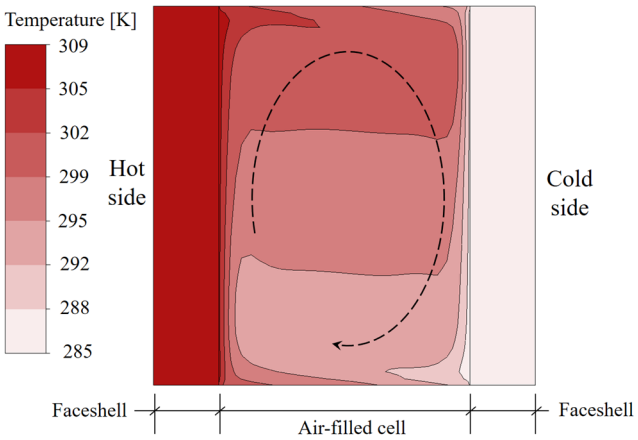

Fig. 5-11. Representative temperature field in a mid-section cut of a CMU cell.

R-value. For configuration types A1, B1, C1, and D1, the corrected R-values obtained from the procedure explained in Section 5.4 were compared against the simulated R-values. For the numerical predictions, the size and location of the thermocouples and heat flux transducers used in the laboratory experiments were represented as imprinted surface areas in the numerical model as a means of calculating the area-weighted average temperature and heat flux. The average temperatures and heat fluxes from the experimental testing and numerical models are shown in Table 5-6.

Table 5-6 presents the following data for configuration types A1, B1, C1, and D1 in normal- and medium-weight units: the average measured R-value, the variability of the corrected R-value measured through the laboratory experiments, and the predicted R-value obtained through the thermo-fluid dynamics simulations. The comparison shows that the simulated R-values were within the range of the minimum and maximum corrected R-

values. Therefore, the results indicate that the numerical models were an adequate representation of the thermal performance of the CMUs.

Table 5-6. Comparison between corrected and simulated R-values.

		Experiments					Simulations			
Den.	CT	ΔT [K]	$\bar{q}$ [W/m^2]	R_{mea} [m^{2}K/W]	R_{cor} [m^{2}K/W]		ΔT [K]	$\bar{q}$ [W/m^2]	R_{sim} [m^{2}K/W]	Within Range
N-w	A1	20.35	107.98	0.188	0.183	0.213	22.39	109.77	0.204	Yes
	B1	22.61	97.49	0.253	0.254	0.295	24.09	82.88	0.290	Yes
	C1	20.95	77.16	0.296	0.301	0.350	25.06	75.75	0.331	Yes
	D1	23.93	64.36	0.372	0.385	0.448	26.44	59.61	0.443	Yes
M-w	A1	22.32	85.75	0.260	0.262	0.305	24.32	85.67	0.285	Yes
	B1	24.29	70.35	0.369	0.382	0.444	26.05	60.08	0.434	Yes
	C1	22.42	59.69	0.414	0.432	0.503	26.45	54.29	0.487	Yes
	D1	25.67	41.64	0.617	0.654	0.761	27.81	38.16	0.729	Yes

CT: Configuration type

Recall that in Section 5.3.2 the flow regime was assumed to be laminar. This assumption was checked through the results of the simulations. Rayleigh's number (R_a) is a dimensionless number associated with buoyancy-driven flows. It is customary to classify a flow regime as laminar when R_a is lower than 10^6 (Mills 1999; Aviram et al. 2001). The calculation of R_a was determined by Eq. 5-7,

$$R_a = \frac{g\beta(\Delta T)x^3}{v\alpha} \qquad \text{Eq. 5-7}$$

where g is the gravitational acceleration, β is the expansion coefficient, ΔT is the difference of temperature in the cell, x is the characteristic length (x=12.54 cm), v is the kinematic viscosity, and α is the thermal diffusivity of the air. For the configuration types in this study, R_a was 3.4×10^5, which indicated that a laminar flow model could be used in the simulations. Fig. 5-12 illustrates the streamlines in a representative velocity field in a mid-

section cut of a CMU cell (see A-A in Fig. 5-10). The maximum velocity within this figure was located in the boundary layer along the hot and cold inner walls, and the center of the cell was almost stagnant because of a circular air flow pattern.

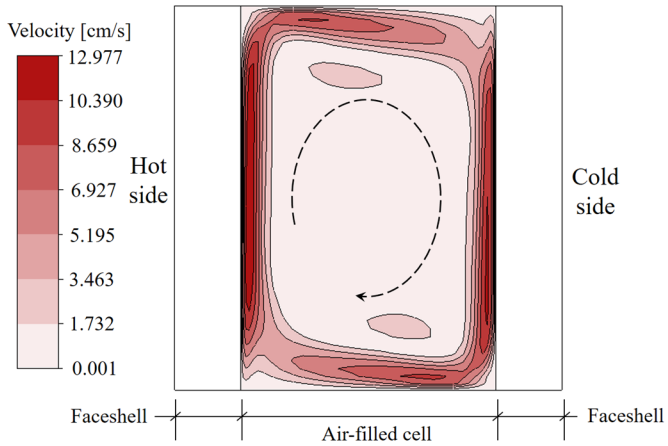

Fig. 5-12. Representative streamlines for a mid-section cut of a CMU cell.

5.6 Thermal Performance of CMU Configurations

In this section, the influence of conduction, convection, and radiation on heat transfer are evaluated for the 24 CMU configuration types shown earlier in Fig. 5-2. As shown in Fig. 5-13, the thermal performance of the conventional 8 × 8 × 16 in. hollow CMU (i.e., configuration type A1) was the lowest; that type had an R-value of 0.207 and 0.293 m^2K/W for the normal- and medium-weight CMUs, respectively. When the unit type was altered, however, higher R-values were obtained. In configuration A6, for example, the normal- and medium-weight CMUs had an R-value of 0.363 and 0.484 m^2K/W, respectively. When insulation materials with a relatively lower thermal conductivity than the CMU were inserted into the cells of the various unit types, the highest R-value predicted was in configuration type D4, which had R-values of 1.050 and 1.581 m^2K/W for the

normal- and medium-weight CMUs, respectively. These improvements in the R-values of configuration type D4 were due to the larger volume of insulated material inserted across the unit's thickness, which reduced the heat flow through the CMU.

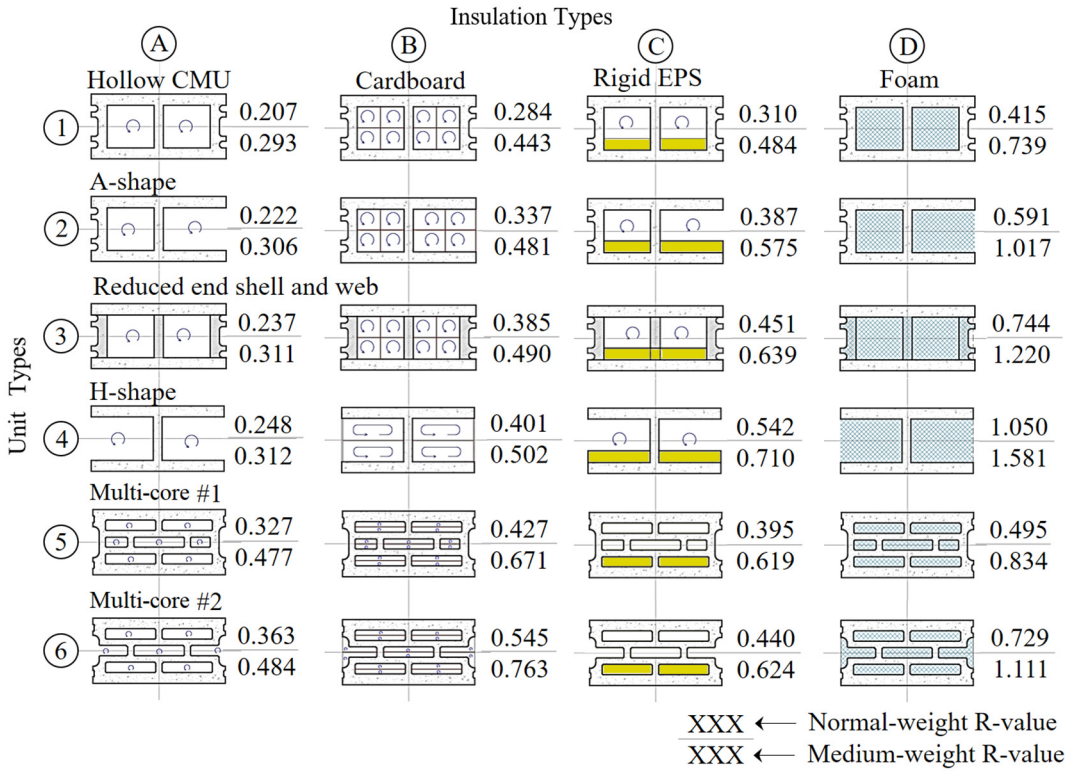

Fig. 5-13. R-values in m^2K/W obtained from numerical simulations for different configuration types. Columns A through D represent different insulation types; rows 1 through 6 represent different unit types.

5.6.1 Effects of Unit Type on Thermal Performance

The effects of unit type on heat flow can be seen in Table 5-7. When configuration type A1 is compared against configuration types A2 through A6, increases in R-values for the latter types become evident for both normal- and medium-weight CMUs. A similar effect is observed when configuration type B1 is compared to configuration types B2

through B6. These consistent (i.e., monotonic) increases in thermal performance from unit type 1 to unit type 6 can be explained by the reduction of the cross-sectional area of continuous thermal bridges. Moving from unit type 1 to unit type 6, the cross-sectional area of thermal bridges was repeatedly reduced. Unit type 1 had three continuous webs, while unit type 2 had only two continuous webs. Meanwhile, unit type 3 had three half-height webs (equivalent to the cross-sectional area of 1.5 webs), and unit type 4 had only one continuous web. For unit types 5 and 6 further attempts were made to break thermal bridges. This reduction in the cross-sectional area of continuous thermal bridges ultimately reduced the rate of heat energy passing through the units.

Table 5-7. Comparison of R-values according to unit type for normal and medium-weight CMUs (CT means Configuration Type). For each insulation type (A-D), the percentage differences are calculated with respect to unit type 1 (e.g., A1, B1, C1 and D1).

Normal-weight unit

CT	R	Diff.	CT	R	Diff.	CT	R	Diff.	CT	R	Diff.
A1	0.207		B1	0.289		C1	0.310		D1	0.415	
A2	0.222	7%	B2	0.337	16%	C2	0.387	25%	D2	0.591	42%
A3	0.237	15%	B3	0.385	33%	C3	0.451	45%	D3	0.744	79%
A4	0.248	20%	B4	0.401	39%	C4	0.542	75%	D4	1.050	153%
A5	0.327	58%	B5	0.427	48%	C5	0.395	27%	D5	0.495	19%
A6	0.363	76%	B6	0.545	88%	C6	0.440	42%	D6	0.729	76%

Medium-weight unit

CT	R	Diff.	CT	R	Diff.	CT	R	Diff.	CT	R	Diff.
A1	0.293		B1	0.443		C1	0.484		D1	0.739	
A2	0.306	5%	B2	0.481	9%	C2	0.575	19%	D2	1.017	38%
A3	0.311	6%	B3	0.490	11%	C3	0.639	32%	D3	1.220	65%
A4	0.312	7%	B4	0.502	13%	C4	0.710	47%	D4	1.581	114%
A5	0.477	63%	B5	0.671	51%	C5	0.619	28%	D5	0.834	13%
A6	0.484	65%	B6	0.763	72%	C6	0.624	29%	D6	1.111	50%

When configuration type C1 is compared to configuration types C2 through C6, the R-values for both normal- and medium-weight CMUs are also shown to increase, albeit not in a monotonic manner. Between C1 and C2, C1 and C3, and C1 and C4, the R-values increase by percentages of 25%, 45%, and 75%, respectively. Yet when C1 is compared to C5 and when C1 is compared to C6, the R-values increase only by percentages of 27% and 42%, respectively. This pattern can be explained if we consider the unit types themselves. Configuration types C5 and C6 featured unit types that were multi-cored with continuous and/or discontinuous thermal bridging in the end shells. As a result, for configuration types that included unit types 5 and 6, the introduction of the rigid EPS and

foam insulations no longer led to a significant degree of percentage increase in R-values. This observation also held true for insulation type D.

The TFD simulations enabled the heat transferred across the unit to be separated into the three mechanisms of conduction, convection, and radiation. Moving from configuration type A1 to configuration types A2 through A6 for normal- and medium-weight CMUs, conduction was reduced in the latter types as a result of the reduction of the cross-sectional area of continuous thermal bridges. Reducing the thermal bridges in the units slightly increased the temperature gradient across the air cavity. Convection and radiation increased in configuration types A2 through A4 because of the increase in air volume and air velocity within the CMU cells.

The nonconventional web and shell features of unit types 5 and 6 resulted in a decrease in convection because those features reduced the amount of heat that was conducted through the CMUs and diminished the air volume within CMU cells. The number of barriers (interfaces) within the cells of unit types 5 and 6 also reduced those configuration types' rates of radiation transport. The combination of these effects (i.e., decreased conduction, convection, and radiation transport) resulted in both a slight increase in the gradient temperature across and a reduction in the air velocity within the cells of configuration types A5 and A6.

5.6.2 Effects of Insulation Type

As shown in Table 5-8, the configurations with insulation type B (i.e. extruded cardboard) generally had higher R-values than those with insulation type A (i.e., hollow

cells with no insulation). For insulation type B, the addition of extruded cardboard interrupted the air flow within the CMU cells and effectively divided the volume in the cells into smaller sub-cells. Similarly, the configurations with insulation type C had higher R-values than those with insulation type A because they contained an insulating layer of rigid EPS, a material that is around 40% less conductive than the CMU material itself. Finally, the configurations with insulation type D had higher R-values than those with insulation type A because the injected foam within them removed the air from the cells. As a result, the rates of heat energy and heat flow that passed through the configurations with insulation type D were reduced.

Table 5-8. Comparison of R-values according to insulation type for normal- and medium-weight CMUs (CT means Configuration Type). For each unit type (1-6), the percentage differences are calculated with respect to insulation type A (e.g., A1, A2, A3, A4, A5 and A6).

Normal-weight unit						Medium-weight unit					
CT	R	Diff.	CT	R	Diff.	CT	R	Diff.	CT	R	Diff.
A1	0.207		A2	0.222		A1	0.293		A2	0.306	
B1	0.289	40%	B2	0.337	52%	B1	0.443	51%	B2	0.481	57%
C1	0.310	50%	C2	0.387	75%	C1	0.484	65%	C2	0.575	88%
D1	0.415	101%	D2	0.591	167%	D1	0.739	152%	D2	1.017	232%
CT	R	Diff.	CT	R	Diff.	CT	R	Diff.	CT	R	Diff.
A3	0.237		A4	0.248		A3	0.311		A4	0.312	
B3	0.385	62%	B4	0.401	62%	B3	0.490	58%	B4	0.502	61%
C3	0.451	90%	C4	0.542	118%	C3	0.639	106%	C4	0.710	128%
D3	0.744	214%	D4	1.050	323%	D3	1.220	292%	D4	1.581	407%
CT	R	Diff.	CT	R	Diff.	CT	R	Diff.	CT	R	Diff.
A5	0.327		A6	0.363		A5	0.477		A6	0.484	
B5	0.427	31%	B6	0.545	50%	B5	0.671	41%	B6	0.763	58%
C5	0.395	21%	C6	0.440	21%	C5	0.619	30%	C6	0.624	29%
D5	0.495	52%	D6	0.729	101%	D5	0.834	75%	D6	1.111	130%

As regards nonconventional unit types 5 and 6, the addition of an insulating material increased the R value for both normal- and medium-weight CMUs. As can be seen in Table 5-8, the extruded cardboard (insulation type B) was more effective in reducing the heat flow than the rigid EPS (insulation type C). This observation can be explained by the fact that the extruded cardboard in the B configuration types allowed for smaller sub-cells and impeded airflow; however, the rigid EPS did not block the airflow within the cells. Among all insulation types, injected foam (insulation type D) led to the highest increase in R values. The increased R-values associated with insulation type D were attributable to the less conductive properties of the injected foam, which prohibited air flow within the cells.

The three heat transfer mechanisms of conduction, convection, and radiation were distributed differently in different insulation types. When unit type 1 was combined with insulation types B (i.e., extruded cardboard) and C (i.e., rigid EPS), the resulting configuration types (i.e., B1 and C1) showed a similar amount of heat conduction as configuration type A1 (i.e., hollow cells with no insulation). In other words, extruded cardboard and rigid EPS had a negligible contribution to heat conduction. In the case of insulation type B, convection was reduced because the cells were broken down into multiple smaller cells; meanwhile, for insulation type C, a similar reduction in convection occurred because the rigid EPS took up a portion of the air volume in the cells. The smaller air cavities in the cell for insulation types B and C ultimately reduced the temperature gradient and air velocity across the cells; radiation transport was also reduced in cells with these types of insulation as a result of an extra pair of interfaces within the cells. Finally, a comparison between insulation type A and insulation type D showed an increase in heat conduction in the latter insulation type; fundamentally, for both normal- and medium-weight units conduction was the primary heat transfer mechanism in configuration types that featured insulation type D.

5.7 Discussion of Feasibility of Implementation in the Construction Industry

To determine the feasibility of implementing this study's 24 configuration types in masonry construction, the cost of each CMU must also be taken into account. To estimate the costs, we accounted for the amount of each material that goes into the individual CMUs and the labor costs associated with those materials. Acquired from the manufacturer, configuration type A1 in normal and medium weights costs $1.49 and $1.56, respectively.

Labor costs for commercial installation of configuration type A1 were estimated using a base cost of $4.25 per unit. Because of increased weight, labor costs were slightly higher for configuration types that included unit type 3 (10%) and substantially higher (50%) for configuration types that included unit types 5 and 6. The volume of unit types 1 through 6 can be determined from the units' dimensions. Since the relationship between cost and volume is known for unit type 1, the cost for unit types 2 through 6 can be estimated solely based on the volume of material in each of those unit types. Additional costs must be added to unit types 2 and 4 to account for higher probability of breakage during shipping and handling. Accordingly, the cost for unit type 2 was adjusted by 10%, and the cost of unit type 4 (which is more susceptible to breakage than unit type 2) was adjusted by 20%.

The cost for the insulation types B, C, and D was calculated as the cost of the insulating materials added. The cost of extruded cardboard is priced at $0.002 per ft^2, the rigid EPS at $0.004 per ft^3, and polyurethane (injected foam) at $0.004 per ft^3. Volumes of the added materials were obtained from measurements of different configuration types. The labor costs associated with the installation of the insulating material were assumed to be identical for all insulation types. The cost of transportation has been included, adding $0.15 per unit for configuration type A1 normal-weight. The transportation cost for the rest of configurations has been added/reduced proportional to the weight of each configuration type.

Next, the cost-effectiveness of the CMUs was analyzed by calculating the ratio of the R-value to the cost for each configuration type. The ratio represents the amount of R-value that was obtained for every US dollar invested. As seen in Table 5-9, four of the five

configuration types with the highest ratios share insulation type D. According to these results, the most cost-effective configuration type was identified as D4 with a ratio of 0.131 and 0.197 R-value per USD invested for normal- and medium-weight. Despite the increase in thermal performance when unit and insulation types are changed, the hollow unit (A1) remains the most widely used unit around the world due to its high structural capacity and ability to allow for the placement of grout and steel reinforcing bars within the cells. Moreover, since this configuration type has been extensively studied, current design guidelines are oriented towards the design of this configuration type.

Table 5-9. Five highest R-values per US dollar for normal- and medium-weight units.

Normal-weight		Medium-weight	
CT	[R-value/USD]	CT	[R-value/USD]
D4	0.131	D4	0.197
D3	0.091	D3	0.150
C4	0.087	D2	0.130
D2	0.076	C4	0.113
D6	0.074	D6	0.114

5.8 Conclusions

Energy consumption caused by cooling and heating in commercial and residential buildings is likely to increase in the coming years and decades. This problem can be addressed if the insulation properties of building materials are maximized through a better understanding of those materials' thermal resistance, or R-value. In this paper, the R-values of CMUs were studied through an experimental and numerical campaign of thermo-fluid dynamic analyses. Using different scenarios, the current study investigated the thermal

effects of (i) the material properties of CMUs, (ii) varied geometric configurations of CMUs, and (iii) the addition of insulation material within CMU cells.

The capabilities of the numerical model were demonstrated by comparing the model's results with those of the hot-box experiments for configuration types A1 (conventional hollow unit), B1 (addition of extruded cardboard to conventional unit), C1 (addition of rigid EPS to conventional unit), and D1 (addition of injected foam to conventional unit). The comparison showed an acceptable agreement between the numerical model and the experiments and supported the view that the model accurately captures the thermo-fluid dynamics. Because the models were validated, the following conclusions can be reached for the studied configurations:

- The air flow within the cells of the studied configuration types contributes to the heat transfer within the CMU cells and should not be ignored in thermal analysis.
- Buoyancy drives the air flow within the CMU cells so that it moves in a circular pattern. Moreover, the laminar flow regime governs the air behavior.
- The density of the concrete material used in CMUs has an important effect on the thermal behavior of the CMUs; the magnitude of the effect varies based on unit and insulation type. The thermal performance of a conventional CMU without insulation (i.e., configuration type A1) shows a noticeable sensitivity to concrete density, as the medium-weight unit has an R-value that is 42% higher than that of a normal-weight unit. The thermal performance of an H-shaped unit with extruded cardboard (i.e., configuration type B4) shows the lowest sensitivity to the density of the concrete, as the thermal performance of the medium-weight unit is only 25% higher than that of the

normal-weight unit. Finally, the thermal performance of a conventional unit with injected foam (i.e., configuration type D1) exhibits the highest difference in thermal performance between the normal- and medium-weight units. For D1, the thermal performance of the medium-weight unit is 78% higher than that of the normal-weight unit.

- In terms of unit type, configuration type D4 (i.e., H-shaped unit with injected foam) provides the highest improvement in R-values over its baseline configuration type (i.e., D1, hollow unit with injected foam in the cells). For configuration types with insulation type D (i.e., addition of injected foam), the R-value increases 153% between D1 and D4 for normal-weight units and 114% between D1 and D4 for medium-weight units.
- In terms of insulation type, configuration type D4 (i.e, H-shaped unit with injected foam) also shows the highest improvement over its baseline configuration type (i.e., A4, an H-shaped unit with no insulation). For the normal-weight unit, the R-value increases 323%, and for the medium-weight unit, the R-value increases 407%.
- The numerical models also demonstrate the importance of considering the three heat transfer mechanisms (i.e., conduction, convection, and radiation) in the thermal analysis of CMUs. In general, conduction can be altered by modifying the unit type (i.e., the unit geometry) and by changing the number and cross-sectional area of thermal bridges within the unit. Convection can be altered by modifying the air volume within the units' cells and by breaking up those cells into smaller sub-cells. Moreover, radiation can be altered by modifying the air volume within CMU cells and adding interfaces or barriers within those cells.

- The highest cost-effectiveness ratio is obtained for configuration type D4 (i.e., H-shaped unit with injected foam). For the normal-weight unit, the ratio is 0.131 R-value/USD, and for the medium-weight unit, the ratio is 0.197 R-value/USD. The lowest cost-effectiveness ratio is obtained for configuration type A1 (hollow unit). For the normal-weight unit, the ratio is 0.035 R-value/USD, and for the medium-weight unit, the ratio is 0.049 R-value/USD.

Air velocities are expected to be relatively higher for a wall than within a single-unit analysis. As a result, it is necessary to extend the assessment of CMUs' thermal performance to masonry walls and to take air flow dynamics across the height of the walls into account. Future studies considering dynamic cycles of loading are also encouraged.

References

Al-Homoud, M. S. (2005). "Performance Characteristics and Practical Applications of Common Building Thermal Insulation Materials." *Building and environment*, 40(3), 353-366.

Alhazmy, M. M. (2006). "Analysis of Coupled Natural Convection–Conduction Effects on the Heat Transport through Hollow Building Blocks." *Energy and Buildings*, 38(5), 515-521.

Alhazmy, M. M. (2010). "Numerical Investigation on Using Inclined Partitions to Reduce Natural Convection Inside the Cavities of Hollow Bricks." *International Journal of Thermal Sciences*, 49(11), 2201-2210.

Almohammadi, K. M., Ingham, D. B., Ma, L., and Pourkashan, M. (2013). "Computational Fluid Dynamics (CFD) Mesh Independency Techniques for a Straight Blade Vertical Axis Wind Turbine." *Energy*, 58, 483-493.

Antar, M. A., and Baig, H. (2009). "Conjugate Conduction-Natural Convection Heat Transfer in a Hollow Building Block." *Applied Thermal Engineering*, 29(17), 3716-3720.

Antar, M. A. (2010). "Thermal Radiation Role in Conjugate Heat Transfer across a Multiple-Cavity Building Block." *Energy*, 35(8), 3508-3516.

Arendt, K., Krzaczek, M., and Florczuk, J. (2011). "Numerical Analysis by FEM and Analytical Study of the Dynamic Thermal Behavior of Hollow Bricks with Different Cavity Concentration." *International Journal of Thermal Sciences*, 50(8), 1543-1553.

ASTM. (2011). "Standard Test Method for Thermal Performance of Building Materials and Envelope Assemblies by Means of a Hox Box Apparatus." *ASTM C1363-11*, West Conshohocken, PA.

ASTM. (2012). "Standard Specificaion for Temperature-Electromotive Force (emf) Tables for Standardized Thermocoouples." *ASTM E230-12*, West Conshohocken, PA.

ASTM. (2014). "Standard Specificaion for Industrial Platinum Resistance Thermometers." *ASTM E1137-14*, West Conshohocken, PA.

ASTM. (2016). "Standard Specification for Loadbearing Concrete Masonry Units." *ASTM C90-16a*, West Conshohocken, PA.

Atamturktur, S., Hemez, F., and Laman, J. (2012), "Uncertainty Quantification in Model Verification and Validation as Applied to Large Scale Historic Masonry Monuments." *Engineering Structures (Elsevier),* 43(1), 221-234.

Aviram, D. P., Fried, A. N., and Roberts, J. J. (2001). "Thermal Properties of a Variable Cavity Wall." *Building and Environment*, 36(9), 1057-1072.

BIA. Brick Industry Association. (2016). "Introduction to Energy Performance of Brick Masonry." *Technical Notes on Brick Construction*, 1-10.

Bilgen, E. (2002). "Natural Convection in Enclosures with Partial Partitions." *Renewable Energy*, 26(2), 257-270.

del Coz Díaz, J.J., García Nieto, P.J., Martín Rodríguez, A., Martínez-Luengas, A.L., and Betegón Biempica, C. (2006). "Nonlinear Thermal Analysis of Light Concrete Hollow Brick Wall by the Finite Element Method and Experimental Validation." *Applied Thermal Engineering*, 26(1), 777-786.

del Coz Díaz, J.J., García Nieto, P.J., Betegón Biempica, C., and Prendes Gero, M.B. (2007). "Analysis and Optimization of the Heat-Insulating Light Concrete Hollow Brick Walls Design by the Finite Element Method." *Applied Thermal Engineering*, 27(1), 1445-1456.

del Coz Díaz, J.J., García Nieto, P.J., Suárez Sierra, J.L., and Betegón Biempica, C. (2008). "Nonlinear Thermal Optimization of External Light Concrete Multi-Holed Brick Wall by the Finite Element Method." *Int. J. Heat and Mass Transfer*, 51(1), 1530-1541.

Ducharme, M.B., Frim, J., and Tikuisis, P. (1990). “Errors in Heat Flux Measurements due the Thermal Resistance of Heat Flux Disks.” *Journal of Applied Physiology*, 69(2), 776-784.

Durbin, P. A., & Medic, G. (2007). *Fluid Dynamics with a Computational Perspective*. Cambridge University Press.

El-Hassan, H., Shao, Y., and Ghouleh, Z. (2013). “Effect of Initial Curing on Carbonation of Lightweight Concrete Masonry Units.” *ACI Materials Journal*, 110(4), 442-450.

Freedonia Group. (2010). “Brick and Block Demand to Reach 12.4 Billion Units, $8 Billion by 2014.” *Journal of Concrete Products*, Freedonia Group Study, 2652(1), 245-248.

Gu, H., and Hunt, J. F. (2007). “Two-dimensional Finite Element Heat Transfer Model of Softwood. Part III: Effect of Moisture Content on Thermal Conductivity.” *Wood and Fiber Science*, 39(1), 159-166.

Henrique dos Santos, G., Fogiatto, M. A., and Mendes, N. (2017). “Numerical Analysis of Thermal Transmittance of Hollow Concrete Blocks.” *Journal of Building Physics*, 1(1), 1-18.

Huygen, N., Sanders, J., and Smith, S. (2017). “Development and Calibration of Method for Thermal Property Measurement of Non-homogeneous Masonry Materials.” (In preparation).

Huygen, N., and Sanders, J. (2017). “Dynamic Thermal Performance Measurements.” (In preparation).

Incropera, F.P., DeWitt, D.P., Bergman, T.L., and Lavine, A.S. (2006). *Fundamentals of Heat and Mass Transfer,* John Wiley and Sons, NJ.

Karimi, M., Akdogan, G., Dellimore, K. H., and Bradshaw, S. M. (2012). "Quantification of Numerical and Model Uncertainties in the CFD Simulation of the Gas Holdup and Flow Dynamics in a Laboratory Scale Rushton-Turbine Flotation Tank." *In the 9th International Conference on CFD in the Minerals and Process Industries*, CSIRO, Melbourne, Australia.

Kosny, J., and Christian, J. E. (1995). "Thermal Evaluation of Several Configurations of Insulation and Structural Materials for Some Metal Stud Walls." *Energy and Buildings*, 22(2), 157-163.

Laaroussi, N., Lauriat, G., Raefat, S., Garoum, M., and Ahachad, M. (2017). "An Example of Comparison between ISO Norm Calculations and Full CFD Simulations of Thermal Performances of Hollow Bricks." *Journal of Building Engineering*, 11(1), 69-81.

Li, L.P., Wu, Z.G., He, Y.L., Lauriat, G., and Tao, W.Q. (2008a). "Optimization of the Configuration of 290x40x90 Hollow Clay Bricks with 3D Numerical Simulation by the Finite Volume Method." *Energy and Buildings*, 40(1), 1790-1799.

Li, L.P., Wu, Z.G., Li, Z.Y., He, Y.L., and Tao, W.Q. (2008b). "Numerical Thermal Optimization of the Configuration of Multi-Holed Clay Bricks Used for Constructing Building Walls by the Finite Volume Method." *Int. J. Heat and Mass Transfer*, 51(1), 3669-3682.

Lienhard IV, J.H., and Lienhard V, J.H. (2003). *A Heat Transfer Textbook,* Phlogiston Press, MA.

Losada, I.J., Losada, M.A., and Martin, F.L. (1995). "Experimental Study of Wave-induced Flow in a Porous Structure." *Coastal Engineering*, 26(1), 77-98.

Mahoutian, M., Chaallal, O., and Shao, Y. (2018). "Pilot Production of Steel Slag Masonry Blocks." *Canadian Journal of Civil Engineering*, (in print).

Martínez, M., Atamturktur, S., Ross, B., & Thompson, J. (2017). "Assessing the Compressive Behavior of Dry-stacked Masonry with Experimentally Informed Numerical Models." *ASCE Journal of Structural Engineering*. https://doi.org/10.1061/(ASCE)ST.1943-541X.0002056

Martínez M. and Atamturktur S., (2017), "Experimental and Numerical Evaluation of Reinforced Dry-Stacked Concrete Masonry Walls." *Journal of Building Engineering (Elsevier),* (submitted, in review).

Mills, A.F. (1999). *Heat Transfer*, Prentice-Hall, New Jersey.

Mobedi, M. (2008). "Conjugate Natural Convection in a Square Cavity with Finite Thickness Horizontal Walls." *International Communications in Heat and Mass Transfer*, 35(4), 503-513.

Mollineaux, M., Van Buren, K., Hemez, F., and Atamturktur, S. (2013), "Simulating the Dynamics of Wind Turbine Blades: Part I, Model Development and Verification." *Wind Energy (Wiley),* 16(5), 694-710.

Nayak, R., Tarkes, D. P., and Satapathy, A. (2010). "A Computational and Experimental Investigation on Thermal Conductivity of Particle Reinforced Epoxy Composites." *Computational Materials Science*, 48(3), 576-581.

NCMA TEK 6-2C. (2013). "R-Values and U-Factors of Single Wythe Concrete Masonry Walls." *National Concrete Masonry Association*.

Ozel, M. (2011). "Thermal Performance and Optimum Insulation Thickness of Building Walls with Different Structure Materials." *Applied Thermal Engineering*, 31(17-18), 3854-3863.

Peirce, B. O., and Willson, R. W. (1990). "On the Thermal Diffusivities of Different kinds of Marble." *In Proceedings of the American Academy of Arts and Sciences*, 36(2), 13-16.

Plaskolite. (2017). "Physical, Chemical, Mechanical, and Thermal Properties of OPTIX Acrylic." Accessed on July 27, 2017 < http://www.plaskolite.com/Fabrication/Acrylic/Optix>.

Prabhu, S., Atamturktur, S., Brosnan, D., Dorrance, R., and Messier, P. (2014), "Foundation Settlement Analysis of Fort Sumter National Monument: Model Development and Predictive Assessment." *Engineering Structures (Elsevier),* 65(1), 1-12.

Ratanathavorn, W., Charoenjai, S., Janbuala, S., Chalermsinsuwan, B., and Poochinda, K. (2015). "Effects of Design Parameters for Clay Brick Kiln Using Computational Fluid Dynamics and Experimental Design." *Advanced Materials Research*, 1101(1), 51-56.

Richardson, L. F., and Gaunt, B. A. (1927). “The Deferred Approach to the Limit.” *Phil. Trans. R. Soc. Lond. A*, 226(636-646), 299-361.

Roache, P.J. (1994). “Perspective: A Method for Uniform Reporting of Grid Refinement Studies.” *Journal of Fluids Engineering*, 116(3), 405-441.

Roache, P. J., Schmalz, R. A., Jia, Y., and Smith, P. E. (2009). Verification and Validation of 3D Free-surface Flow Models. *American Society of Civil Engineers*.

Sambou, V., Lartigue, B., Monchoux, F., and Adj, M. (2016). “Modeling of the Thermal Performance of Air-filled Partitioned Enclosures: Effects of the Geometry and Thermal Properties.” *Journal of Building Physics*, 39(4), 321-341.

Sanders, J., and Brosnan, D. (2010). “Improving the Thermal Resistance of Brick Masonry Systems.” *In Masonry. ASTM International*, 7(4), 134-146.

Smith, S.K. (2016). “Development of the Modified Hot Box: A Convective Heat Transfer Device for Measuring the Steady State and Transient Thermal Properties of Non-Homogenous Building Materials.” *M.S. thesis*. Clemson University, SC.

Stern, F., Wilson, R.V., Coleman, H.W., and Paterson, E.G. (2001). “Comprehensive approach to Verification and Validation of CFD Simulations Part 1: Methodology and Procedures.” *Journal of Fluids Engineering*, 123(4), 793-802.

Stevens, G., Atamturktur, S., Lebensohn, R., and Kaschner, G. (2016), "Experiment-based Validation and Uncertainty Quantification of Coupled Multi-Scale Plasticity Models." *Multidiscipline Modeling in Materials and Structures*, 12(1), 151-176.

Sun, J., and Fang, L. (2009). "Numerical Simulation of Concrete Hollow Bricks by the Finite Volume Method." *International Journal of Heat and Mass Transfer*, 52(23), 5598-5607.

Tleoubaev, A., and Brzezinski, A. (2008). "Error of the Heat Flow Meter Method Caused by Thermal Contact Resistance." *Proc. 29th International Thermal Conductivity Conference, ITCC29 and Proc. 17th International Thermal Expansion Symposium, ITES17*.

Quadrant Plastics. (2017). "Thermal Conductivity of HDPE Plastic." Accessed on July 27, 2017 <http://qepp.matweb.com/search/DataSheet.aspx?Bassnum=P1SMP33&ckck=1>.

Valore, R. C. (1980). "Calculations of U-values of Hollow Concrete Masonry." *Concrete International*, 2(02), 40-63.

Van Geem, M. G. (1986). "Thermal Transmittance of Concrete Block Walls with Core Insulation." *Journal of Thermal Insulation*, 9(3), 187-210.

Wakili, K. G., and Tanner, C. (2003). "U-value of a Dried Wall Made of Perforated Porous Clay Bricks: Hot Box Measurement Versus Numerical Analysis." *Energy and Buildings*, 35(7), 675-680.

Wati, E., Meukam, P., and Damfeu, J. C. (2017). "Modeling Thermal Performance of Exterior Walls Retrofitted from Insulation and Modified Laterite Based Bricks Materials." *Heat and Mass Transfer*, 53(12), 3487-3499.

Zarr, R. R., and Pintar, A. L. (2012). "NIST Special Publication 260-175. Standard Reference Materials: SRM 1453, Expanded Polystyrene Board, for Thermal Conductivity from 281K to 313K." *National Institute of Standards and Technology*.

Zhao, C.Y. and Tao, W.Q. (1995). "Natural Convections in Conjugated Single and Double Enclosures." *Int. J. Heat Mass Transfer*, 30(1), 175-182.

Zmeureanu, R., and Fazio, P. (1988). "Thermal Performance of a Hollow Core Concrete Floor System for Passive Cooling." *Building and environment*, 23(3), 243-252.

Zukowski, M., and Haese, G. (2010). "Experimental and Numerical Investigation of a Hollow Brick Filled with Perlite Insulation." *Energy and Buildings*, 42(9), 1402-1408.

CHAPTER SIX

CONCLUSIONS

6.1 Summary of Research

Masonry construction has many advantages over other construction practices. Mortarless masonry systems are especially desirable as they require less construction time and less skilled labor. However, design standards do not currently exist for mortarless construction, largely because knowledge is limited concerning the structural behavior of dry-stack systems under different loading conditions. To increase this knowledge, both experimental tests and numerical models are needed. The combined use of tests and models will enable a better understanding of the physics involved with dry-stack systems and allow for accurate predictions that do not depend on excessive experimental programs and exorbitant computational time.

This dissertation has responded to the need for combined experimental and numerical research on mortarless masonry systems. Chapter Two provided a review of past investigations of different mortarless masonry systems, discussing relevant information related to dry-stack masonry materials, previous scholars' experimental and numerical approaches to mortarless systems, and future directions on dry-stack masonry systems.

Chapter Three presented original research on dry-stacked prisms with experimentally validated and predictive numerical models that explicitly took into account the roughness of unit bedding surfaces. Two variations of surface roughness (i.e., ground and unground) were considered to explore the behavior of associated mortarless prisms under axial compressive loads. Subsequently, a parametric analysis was executed to derive

relationships between unit design variables; these variables included unit compressive and tensile strength, surface roughness, grout strength, and unit size.

In Chapter Four, a numerical model of a reinforced mortarless masonry wall was developed and subjected to out-of-plane loads. The numerical model included the material discontinuity introduced by the existence of joints at actual locations on a physical wall; moreover, the geometry and material properties used in the model were based on experimental measurements. Performing experimental tests on mortarless masonry walls enabled the validation of numerical results concerning the wall's structural behavior. As a result, the experimental tests and numerical models contributed to an understanding of the effects of different design variables (i.e., unit and grout compressive strength, yield strength of reinforcing bars, and percentage of reinforcement and grouting) on the performance of the mortarless masonry walls.

Finally, Chapter Five evaluated the thermal performance of concrete masonry systems; this included either standard units or special thermally efficient unit configurations. Sophisticated numerical models were developed to predict the thermal performance of the masonry units; these models were validated by comparing their results to those of laboratory experiments. Once the numerical models were validated, they were used to evaluate the effects of material properties, geometry, and insulation materials on the heat flow path, distribution of temperatures, and air velocities within the units. The results of this chapter showed the importance of considering the three heat transfer mechanisms and the influence of the flow field when evaluating the thermal performance of masonry units.

6.2 Major Findings of the Research

This subsection details the major findings of the dissertation by chapter.

Chapter Two: Past Accomplishments and Future Directions of Dry-Stack Masonry

- Conventional masonry has advantages over other systems built with concrete, wood, or steel. These advantages, which include reductions in construction time and cost, are magnified when mortarless masonry is used.
- The lack of mortar in dry-stack masonry systems can be compensated for by using non-interlocking units, interlocking units, surface-bonding agents, or pre-stressed reinforcement elements. A combination of these methods may also be used.
- Mortarless masonry systems show a softening in axial stiffness in early stages of loading. In later stages of loading, the axial stiffness increases. This phenomenon is caused by unevenness in the interface between the prisms' and walls' constitutive units.
- Filling hollow unit cells with grout enhances the stability and the axial, shear, and flexural capacity of masonry systems.
- A thin layer of mortar between units does not affect the performance of mortarless masonry systems.
- Further research determining the behavior and shear capacity of dry-stack masonry walls is needed.

Chapter Three: Compressive Behavior of Dry-Stack Prisms under Axial Compressive Loads

- The unit strength and prism strength for both ground and unground units show a linear relationship. However, prisms with ground units exhibit approximately 15% higher compressive capacity than prisms with unground units.
- The tensile strength of masonry units is typically 10% of the units' compressive strength. Increasing the tensile strength by increments of 2% (i.e., to 12, 14,...20%) results in an increase of 7-11% in the compressive strength of prisms with ground units and an increase of 8-12% in the compressive strength of prisms with unground units.
- For prisms with ground units, cracking patterns point to a uniform concentration of compressive stresses at the interface between the units. For prisms with unground units, local failures occur at the interface between the units when low levels of load are applied. Prisms with ground units thus have a higher compressive capacity than prisms with unground units.
- Grout enhances the structural performance of prisms under compressive loads; this improvement in performance is independent of individual units' compressive strength. However, the amount of performance improvement is dependent on whether the units are ground or unground.

Chapter Four: Evaluation of Reinforced Dry-Stack Concrete Masonry Walls

- When the compressive strength of the masonry unit increases from 2,000 to 4,000 psi, the ultimate lateral load-carrying capacity of the masonry wall and its displacement ductility increase by 35% and 185%, respectively. When the grout compressive strength increases from 4,000 to 7,000 psi, the ultimate lateral load-carrying capacity

of the masonry wall and its displacement ductility increase by 22% and 107%, respectively.

- When the yield strength of the steel reinforcing bars increases from 40,000 to 80,000 psi, the ultimate load-carrying capacity of the masonry wall increases by 10%, while its displacement ductility decreases by 69%.
- The ultimate flexural capacity of the wall's cross-section increases by 10% when the reinforcement ratio increases from 0.34 to 0.62%. However, the displacement ductility of the wall decreases by 57% given the same increase in the reinforcement ratio.
- A change from partially grouted to fully grouted walls leads to a 53% improvement in the walls' ultimate load-carrying capacity and increases their displacement ductility by 110%.

Chapter Five: Thermo-Fluid Dynamics Analysis of Concrete Masonry Units

- To study the thermal performance of masonry, the three heat transfer mechanisms (i.e., conduction, convection, and radiation) and the air flow within masonry unit cells must be considered.
- Laminar flow governs the regime of the flow within units.
- In masonry structures, thermal resistance (R-value) is affected by material density. When material densities are high, thermal resistance is lower. In contrast, when material densities are low, higher thermal resistance is obtained. The geometry of masonry units also affects their R-value. For instance, an H-shaped unit has a higher R-value than conventional hollow units. Finally, the R-value of a unit is improved when

a material with low thermal conductivity is added within the unit's cells to interrupt the air or heat flux flow.

- The most cost-effective unit is an H-shaped unit with injected foam in its cells. For normal-weight units, this configuration has an R-value to U.S. dollar ratio of 0.133; for medium-weight units of the same configuration, the ratio is 0.200.

6.3 Limitations and Assumptions

This section summarizes the limitations, assumptions, and constraints of the dissertation's experimental programs and numerical models.

First, the analysis of mortarless masonry models is limited by the computational resources available. Such analysis involves a highly nonlinear problem that is attributable to complex geometric effects, material nonlinearities, and contact nonlinearities. Although mortarless masonry models do have limitations and involve assumptions, their results remain within the range of accuracy.

Second, the applicability of this dissertation's results is constrained by the number of experimental cases examined. In other words, this research is valid only in the domain where the analysis of a structure's mechanistic behavior remains unchanged, despite variations in selected design parameters. In the study of masonry structures, geometric, mechanical, and thermal properties are subjected to variations that arise from the selection of masonry material aggregates and the unit tolerances established during the fabrication process. In this regard, several researchers have recognized that current methods for characterizing unit-height irregularities problematically affect the alignment and the plumb of masonry walls. These limitations are overcome in numerical models, however, as their

effect is imperceptible in comparisons of numerically modeled and experimentally tested behavior.

Third, the numerical models used in this dissertation were guided by the following assumptions: i) the tensile strength of the masonry units was assumed to be 10% of the units' compressive strength; ii) steel reinforcements were assumed to have a bilinear behavior; and iii) a perfect bond was assumed both between the steel reinforcement and the grout, and between the grout and the units. Moreover, because it is challenging to characterize the unevenness of the contact surface of the units, this dissertation modeled the contact surface as a uniform and periodic triangle-shaped sawtooth; such modeling led to acceptable results. Finally, thermal performance was found to be susceptible to thermal contact resistance; in this dissertation, the amount of thermal contact resistance between the units and the instrumentation was assumed to be the same as what other authors have found for similar materials.

6.4 Suggestions for Future Work

This dissertation has provided insights into the structural and thermal behavior of mortarless masonry structures. Future studies can build upon this work and continue to improve understandings of such systems. The following list features suggestions for future research:

- Future studies might take further account of the effect of eccentric loads on mortarless masonry prisms composed of conventional units or proprietary units.

- Future research might systematically study the effect of the number of units within a mortarless masonry system when a compressive test is being run. To date, researchers have found a significant difference in the axial compressive strength of a two-unit dry-stack prism and the axial compressive strength of a seven-unit-high wall. This difference in capacity is attributable to irregularities in the unit interfaces. Future dry-stack design guidelines must consider the relationship among compressive capacity, unit number, and unit irregularity.
- Researchers have found no difference in compressive strength when a mortarless prism with interlocking units is tested in a running bond or stack pattern. Future studies might consider whether this effect is applicable to mortarless prisms with non-interlocking units.
- Future research might further evaluate the behavior of masonry prisms with non-interlocking units when those prisms are subjected to axial eccentric loads.
- Researchers have found that when surface bonding or pre-stressed reinforcement elements are used in mortarless walls, the shear capacity of the walls is inconsistent, preventing scholars from developing a codified mathematical expression, such as in mortared systems. Future shear studies might, therefore, be conducted to shed light on the structural behavior of mortarless masonry systems with surface bonding and pre-stressed reinforcements.
- Future research might consider the evolution of the coefficient of friction as a function of time when increased vertical and horizontal loads are applied simultaneously.

- Future efforts might be directed toward improving a uniform distribution of load in the joints of mortarless masonry systems. Proposed techniques must be able to provide enough friction to avoid sliding failures.
- Researchers have found limitations when predicting the in-plane cyclic behavior of mortarless walls. Future research might, therefore, entail improving numerical models to account for different joint states (e.g., open joints, closed joints, or partially open/closed joints) at a given time.
- Additional combined experimental and numerical studies are needed to investigate further the behavior of post-tensioned mortarless masonry walls containing non-interlocking and conventional units.
- Additional combined experimental tests and numerical simulations might be conducted to study the effect of the absence of mortar on the thermal performance of masonry walls.

The suggestions outlined in this section are intended to promote continued endeavors to expand knowledge about mortarless masonry systems. The suggestions are not exhaustive but should provide a platform for additional research into dry-stack masonry.